Doctoral Dissertation

# Controlled Nanophase Separation of Alloy Towards Nanomaterials Catalyst Tailoring

(合金前駆体のナノ相分離制御による高機能触媒材料の創成)

ABDILLAH SANI BIN MOHD NAJIB

September 2020

Department of Materials Science (Supervisor: Prof Hideki Abe)

Graduate School of Science and Engineering,

Saitama University

Doctoral Dissertation

# Controlled Nanophase Separation of Alloy Towards Nanomaterials Catalyst Tailoring

(合金前駆動体のナノ相分離制御による高機能触媒材料の創成)

ABDILLAH SANI BIN MOHD NAJIB

September 2020

Department of Materials Science (Supervisor: Prof Hideki Abe)

Graduate School of Science and Engineering,

Saitama University

# Table of Contents

# CHAPTER 1

# INTRODUCTION

## 1.1 Background of Study

Catalysis is a phenomenon in which the rate of chemical reaction is increased with the presence of a substance that remained unchanged after the reaction known as catalyst. It has been one of the core components in chemistry, contributing in almost all fields, including agriculture, energy, production and others.

Catalyst of the same phase as the reactant (gas/liquid) is termed as homogeneous catalyst, while heterogeneous catalyst is referred to the one having different phase (solid) from the reactant. Heterogeneous catalyst is preferred in terms of easy separation process from reactant and low recycling cost, despite having limited surface area that lowered the interaction with reactant molecules compared to homogeneous catalyst.

With the emergence of nanoscience, nanomaterials such as nanoparticles and nanostructured materials have been utilized as catalysts, paving an exciting subfield of nanocatalysis. Heterogeneous catalyst from nanomaterials provides high surface area for interaction with reactant molecules, thus increases the catalytic activities. Nanoparticles come in variants of metallic nanoparticles and supported catalysts while nanostructured catalyst includes nanoporous metal, core-shell structured, hollow structured and others. With the uprising number of research on nanomaterials catalyst, numerous synthesis routes were proposed.

Recent research trend shifted from focusing solely on increasing the surface area, to incorporating facet tailoring in the synthesis process. This is motivated by the fact that chemical reactions are greatly dependent to the catalyst facets. Bottom-up approach such as precipitation, sol-gel, and reduction are conventional methods to produce nanoparticles. However, these processes often involve laborious procedures. There are also number of successful attempts to tailor the nanoporous materials through bottom-up approach using templates such as block copolymers, liquid crystals and/or mesoporous silica, but these templates are far too costly for industrialization.[1–7] Top-down approach is the more practical option for mass production of catalyst. However, it remains a challenge to tailor such nanomaterials having high surface area

and active facets through this approach. Process such as ball-milling and selective leaching often results in uncontrolled phase/facet formation. On the other hand, lithographic technique is too artificial and not suitable for large scale production of catalyst. A spontaneous, yet controllable synthesis method is an ideal choice for mass production of nanomaterials catalyst.

In this research, we developed a synthesis mechanism by taking advantage of the phase separation occurs during the oxidation of intermetallic compound. (Since the phenomenon takes place at nanoscale order, we will call it nanophase separation from here onwards). The intermetallic compound precursor was made up of 2 elements, easily oxidized metal and metal with high oxidation resistant. When subjected to controlled amount of oxidant at elevated temperature, metal having high affinity towards oxygen got oxidized into oxide, while the remaining stable element became pure metal. This eventually created a network of metal and oxide nanocomposite. The relative diffusion coefficient between the 2 participating elements results in different phase distribution (pattern) of the metal-oxide nanocomposite. This pattern formation could be associated to the exothermic reaction-diffusion. A simpler form of reaction-diffusion model, the Gray-Scott model, will be used to simulate the pattern formation during phase separation in chapter 4. Real-time observation of the nanophase separation involving platinum-cerium ($Pt_5Ce$) intermetallic compound will also be presented in the same chapter. The practical application of the tailoring via nanophase phase separation and its merit in controlling the facets will be demonstrated in chapter 5 where metallic nanoporous ruthenium (Ru) and rhodium (Rh) catalyst were synthesized from respective nanocomposite and tested for hydrogen generation reactions.

## 1.2 Objective of Study

The purposes of this research are as follows

1) To understand the trend of pattern formation in reaction-diffusion process by adopting Gray-Scott model as reference model for simulation.
2) To demonstrate the concept of surface tailoring with the emerging pattern of experimentally synthesized metal-oxide nanocomposite.
3) To materialize nanoporous metal catalyst from nanophase separation method and demonstrate the practical application with hydrogen generation reactions

## 1.3 Problem Statement

Nanocatalysis field demands the incorporation of high surface area and facet controlled catalyst tailoring. Large scale production of nanomaterials catalyst through bottom-up approach often involves laborious procedures and costly templates, while top-down approach synthesis results in uncontrolled phase/facet formation. A spontaneous yet controllable synthesis route of nanomaterials catalyst is needed.

The concept of nanophase separation proposed in this study requires a clear demonstration of mechanism on pattern formation, facet tailoring, and practical application.

## 1.4 Scope of Study

This study covers simulation of nanophase separation based on Gray-Scott model and nanomaterials synthesis of PGMs (Pt, Ru, Rh) and easily oxidized Y and Ce counterpart. Practical applications consist of hydrogen generation reaction using metal catalyst for hydrogen generation reactions.

# CHAPTER 2

# LITERATURE REVIEW

## 2.1 Catalysis

The history of catalysis predates to earliest time of mankind with traditional processes like fermentation to produce alcohol before it was systematically organized and classified as catalysis for modern science by a Swedish scientist, Jöns Jacob Berzelius in 1835.[8] Since then, catalysis has developed into one of the most important field in chemistry. Whether in destructive manner of explosives and fighter fuels used in world war, or in constructive manner of polymer productions and fertilizer synthesis, catalysis plays a crucial role over mankind for the past centuries affecting geopolitics, economy, and environments. Recent study reveals that almost half of the world population is being benefited by one of the great breakthroughs in catalysis, i.e., Harber-Bosch reaction that utilized metal catalyst at high pressure and temperature. In addition, with the catalyst development such as Ziegler–Natta catalyst, synthetic polymer production had become possible, driving the industrial and manufacturing revolution in all possible direction.

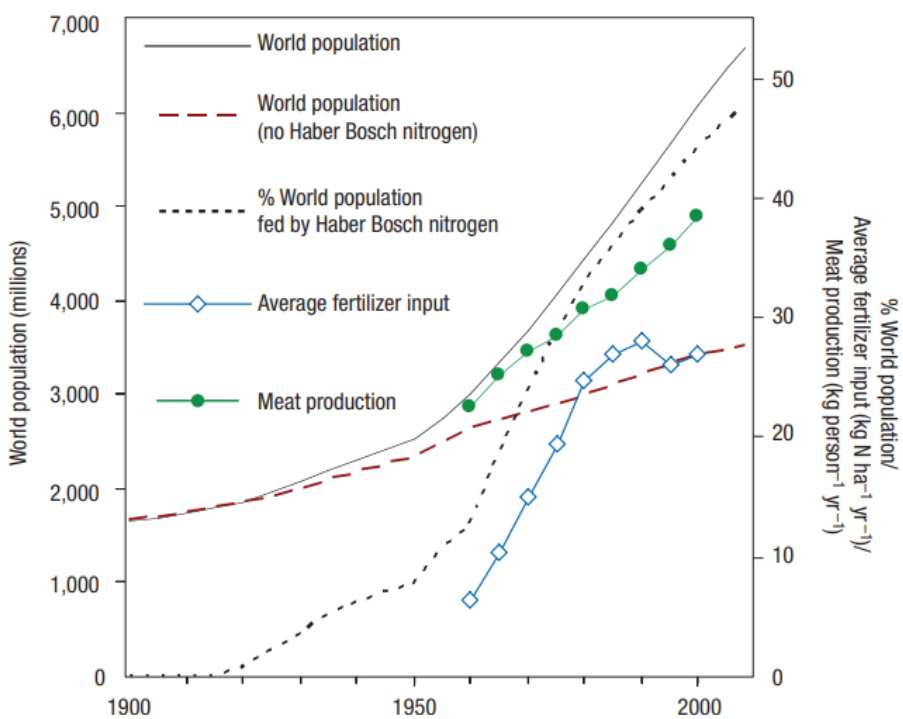


Figure 2.1: Trends in human population and nitrogen use throughout the twentieth century.[9]

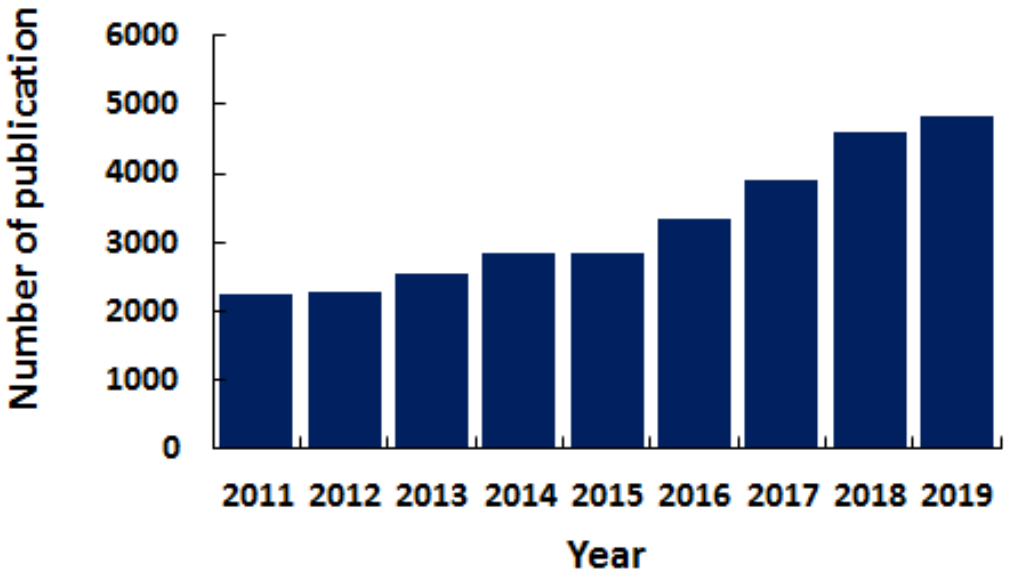


Figure 2.2: Recent number of publication by ACS catalysis

Thousands of researches have been published yearly on catalysis, showing how important and the growing interests on the subject. Most researches focus on improving the conversion rate, selectivity, lowering reaction temperature, and prolong catalyst lifespan. Modification includes reactor designs,[10,11] catalyst improvement,[12–14] and feed gas conditions,[15]. In addition, fundamentals studies on mechanism has led to more sophisticated findings such as light illumination effect and electricity, further expands the field of catalysis into photocatalysis and electrocatalysis. With the advancement of characterization technique, catalysis field is expected to continue to expand in future.

## 2.2 Nanocatalyst

With the emergence of nanoscience, the concept of nanomaterials had been introduced attributing to its unique chemical, electronic, mechanical and optical properties compared to bulk materials. Nanomaterials is a class of materials with single unit size between 1 and 100 nm or more precisely, according to ISO/TS 80004, it is defined as "material with any external dimension in the nanoscale (1 nm - 100 nm) or having internal structure or surface structure in the nanoscale (1 nm - 100 nm)".[16] Thus it covers nano-objects (ex: nanoparticle, nanorod, nanotube, nanoribbon) and nano-structure materials (ex: nanocomposites, nanoporous materials,

nanocrystalline materials). The vast application of nanomaterials includes nanoelectronics, nanoadsorbents, nanomedicine, and nanocatalyst.[17–19]

In principle, catalyst is classified into 2 main types, homogeneous catalyst and heterogeneous catalyst. The former exist in the same phase as the reactant (gas/liquid), while the latter comes in different form (solid). Heterogeneous catalyst is more favorable in terms of recyclability and easy separation from reactant, but its molecular interaction with reactant is more limited compared to homogeneous catalyst. With the utilization of nanomaterials, heterogeneous nanocatalyst effectively promotes interactions with reactant due to its high surface area. Nanoparticles and nanoporous materials are among the most common form of nanocatalysts used.

Nanocatalyst could be synthesized by either bottom-top or top-down approach with theirs own merits and demerits. Among the most common bottom-up approach to synthesize nanoparticles are precipitation, sol-gel, impregnation, and reduction. On the other hand, nanoporous catalyst is usually produced through chemical deposition to hard templates such as mesoporous silica and/or precipitation over soft templates such as block copolymers.[20–22] Through this approach, catalyst size, and in some cases facets could be carefully tailored by adjusting the synthesis condition. However, laborious procedures and the use of costly templates and precursors are the main drawbacks for industrializations. Nanocatalyst synthesis by top-down approach includes ball-milling and etching methods which are scalable, low-cost, and practical. Yet, catalyst size distribution and facets could hardly be manipulated via these techniques.

### 2.3 Phase separation and metal oxidation

Phase separation is a well-known phenomenon in which a single solid (liquid) phase separates into two or more new phases.[23] The separation often associated with thermodynamic instability of the homogeneous multicomponent system to the lower free energy system.[24] As per described by Gibbs, the instability decomposition could be divided into two regimes: (a) Nonlinear instability which is large in degree but small in extent (nucleation and growth), (b) Linear instability which is small in degree but large in extent (spinodal decomposition).[25,26] Favvas and Mitropoulos illustrated the mechanism of nucleation and growth and spinodal

decomposition as in Figure 2.3, whereby the former occurs in metastable region (m) while the later takes place in unstable region (u). It is also described in the same work that the work required for nucleation, W is given by the equation (1), while spinodal decomposition is governed as Cahn-Hilliard model (equation (2)).[27]

$$W = 4\pi r^2\gamma - \frac{4}{3}\pi r^3 \Delta P \quad (1)$$

r: radius of nucleus, γ: surface tension, ΔP: hydrostatic pressure

$$\frac{\partial C_B}{\partial t} = \left\{M\left(\frac{\partial f^2}{\partial {C_B}^2}\right)\right\}_{-D} \nabla^2 C_B - 2M\kappa\nabla^4 C_B \quad (2)$$

$f$: $free\ energy\ of\ homogeneous\ material\ of\ composition\ C_B, M$: $positive\ constant,$

$\kappa$: $positive\ parameter$

Spinodal decomposition can be found in phase diagram of metals alloys, metallic glass, and mixtures of polymers. Applications of it includes alloy hardening for structural materials, production of metallic glass matrix composite, and fabrication of porous polymer membranes in tissue engineering.[28–30] On the other hand, the use of nucleation is found in many places including functional glass ceramics production, synthesis of drugs crystals and age hardening of alloys.[29,31,32]

Oxidation is an exothermic reaction as oxides are more stable (lower free energy) compared to their pure forms. Classical oxidation theory by Wagner which describes parabolic oxide growth overlooks the initial stage of oxidation mechanism.[33] Several recent researches had demonstrated the formation of oxide islands (nucleation) at the surface of metals/alloys.[34,35] Zhou described the thermodynamics of oxide during metal oxidation highlighting the lower oxygen contact angle reduces the nucleation free energy barrier.[36] Luo et. al. showed selective oxidation of Cu in Cu-5 at.%Pt system where areas adjacent to $Cu_2O$ oxide islands was lower in Cu content showing Cu was consumed (diffused to the $Cu_2O$ oxide island).[34]

Instead of metal alloys, in previous study, Abe et. al. used intermetallic compound (IMC) from 2 metals with different oxygen affinity as precursor for the controlled oxidation. Phase separation from homogeneous system of monophasic intermetallic compound to biphase metal-

oxide nanocomposites was observed. However, comprehensive demonstration of the phenomenon, crystal orientations, pattern formation mechanism and analysis, was never mentioned.[37]

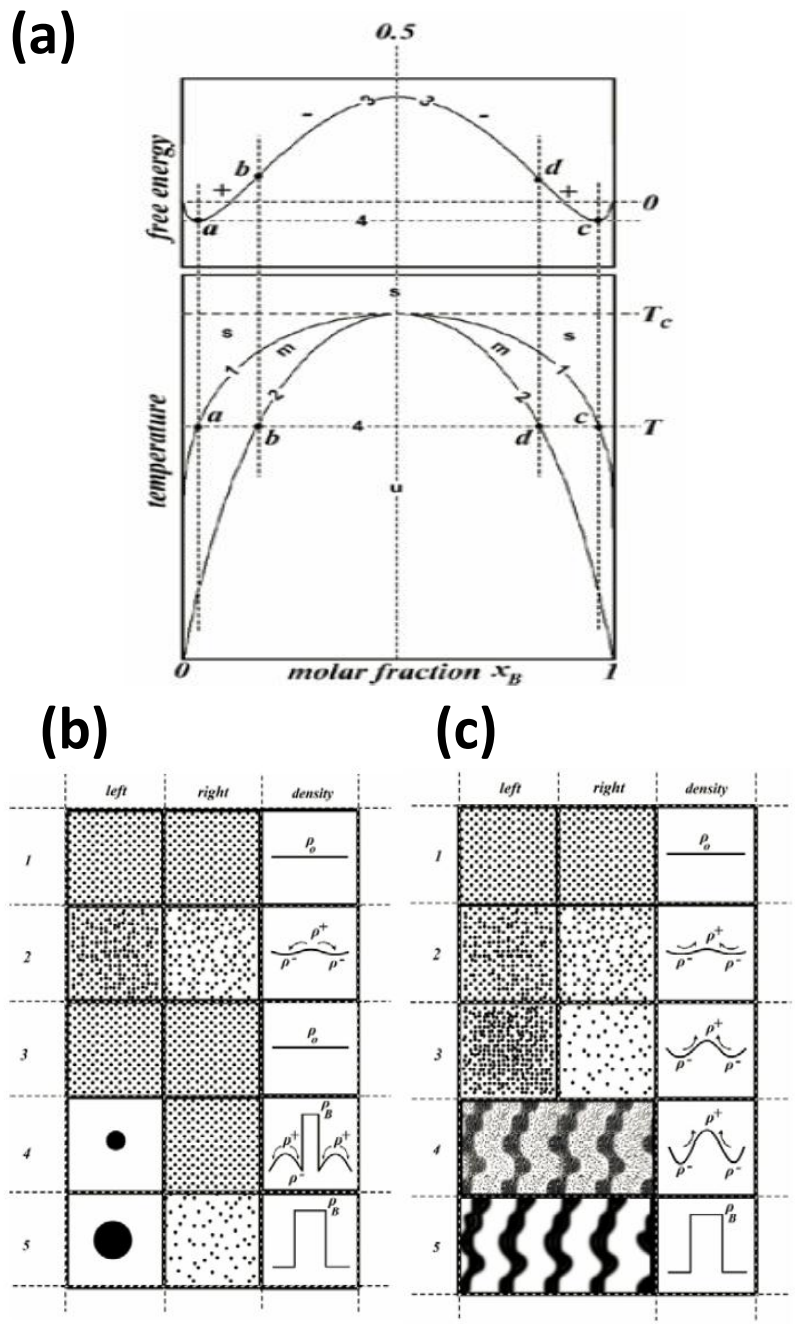


Figure 2.3: (a) Phase diagram with miscibility gap (lower) and free energy change, Mechanism of (b) nucleation and growth, and (c) spinodal decomposition. Reproduced from Favvas et. al.[27]

2.4 Pattern formation

Initiated by Alan Turing in 1952, the concept of pattern modelling was introduced to describe morphogenesis – reaction (perturbation/disturbance) and diffusion of initially homogeneous chemical substances called morphogens which eventually result in inhomogeneous system, forming patterns. These morphogens interaction is that of opposite to each other, e.g., activator-inhibitor relationship or growth and decay relationship. The model consists of reaction–diffusion equations (3) of the two morphogens with respective diffusion coefficients.

$$\begin{cases} \frac{\partial u}{\partial t} = d_1 \nabla^2 u + f(u,v) \\ \frac{\partial v}{\partial t} = d_2 \nabla^2 v + g(u,v) \end{cases} \quad \text{.....(3)}$$

$u, v$: $morphogen\ concentration$ $\qquad$ $f, g$: $reaction\ kinetics$

$d_1, d_2$: $diffusion\ coefficients$

While Turing model is the general form of the reaction-diffusion, a few models have been introduced by specifically assigning the reaction kinetics terms of $f$ and $g$. This includes Gierer-Meinhardt model,[38] Schnakenberg model,[39,40] and Gray-Scott model.[41] While majority of the works deals with biological reactions, Mimura et. al. proposed pattern dynamics in exothermic reaction-diffusion system as follows.[42]

$$\begin{cases} \frac{\partial \mathrm{T}}{\partial t} = d_T \Delta T + \frac{1}{\varepsilon}\left(-\kappa T + a e^{\frac{T}{1+\frac{T}{c}}}\right) \\ \frac{\partial \mathrm{a}}{\partial t} = d_a \Delta a + h(a_0 - a) - a e^{\frac{T}{1+\frac{T}{c}}} \end{cases} \quad \text{.....(4)}$$

T: Temperature, a: concentration of reactant, $\mathrm{d}_T$: heat conductivity, $\mathrm{d}_a$: diffusion rate of reactant

ε: time constant of two kinetics, κ: heat radiation rate, c: constant of Arrhenius rate

h: supply rate of reaction, $\mathrm{a}_0$: given concentration outside the system

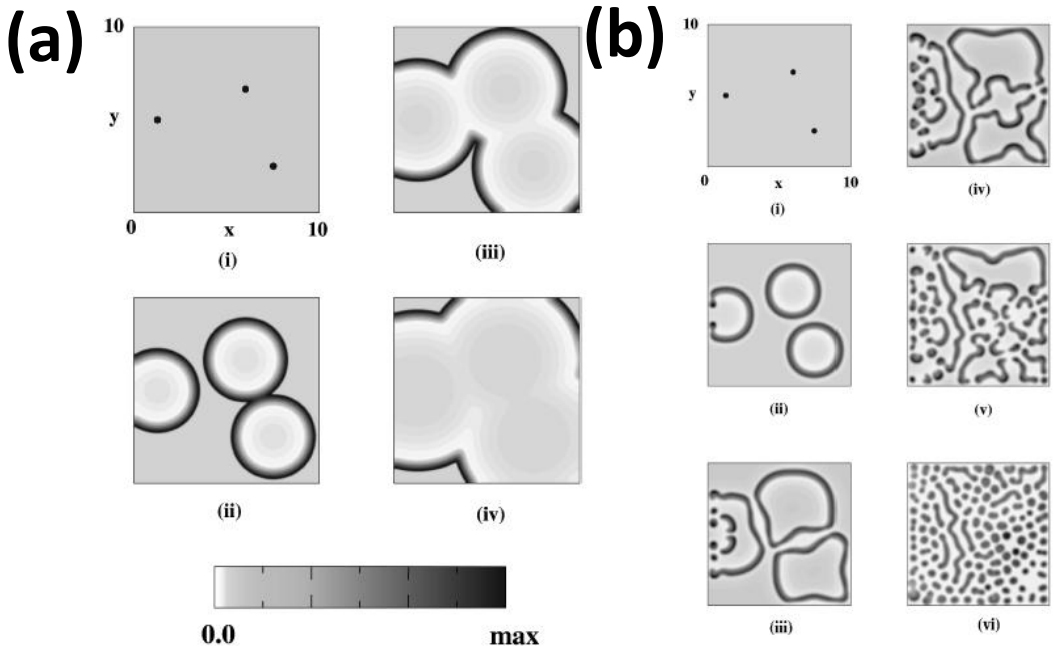


Figure 2.4: (a) Annihilation of three expanding rings with diffusion parameter as (b) Non-annihilation of three rings – diffusion parameter exhibited using exothermic reaction-diffusion model. Reproduced from Mimura et. al.[42]

Unlike other spatio-temporal patterns such as Belousov-Zhabotinsky (BZ) model and FitzHugh-Nagumo model which exhibit annihilation of travelling pulses or expanding rings when they collide, exothermic reaction-diffusion model demonstrate non-annihilation when the relative diffusion exceeds certain value, same as in the Gray-Scott model. In fact, both models are differ only at reaction term as $\mathrm{f(u)} = e^{\frac{T}{1+\frac{T}{c}}}$ in exothermic reaction-diffusion model corresponds to $\mathrm{f(u)} = u^2$in Gray-Scott model (equation 5).

$$\begin{cases} \frac{\partial \mathrm{u}}{\partial t} = d_u \Delta u - uv^2 + F(-u+1) \\ \frac{\partial \mathrm{v}}{\partial t} = d_v \Delta v + uv^2 - v(F+K) \end{cases} \quad \ldots\ldots(5)$$

$u$: activator, $v$: inhibitor, $\mathrm{d}_u$: diffusion rate of u, $\mathrm{d}_v$: diffusion rate of v,

F: flowrate constant, K: rate constant for decay

## 2.5 Metal-oxide interface and facets tailoring

Wide application of metal-oxide interface in electronics, structural, catalysis and corrosion control has made it one of the vital research subjects. Metal-oxide interface could be produced with internal oxidation of alloys, internal reduction of oxides, epitaxial growth of thin film, and solid state bonding. Crystallographic orientations of metal and oxide phase are known to be dependent to the interfacial energy and nucleation kinetics.[43] Orientation with low lattice misfit is favored causing the formation of epitaxial and heteroepitaxial relation at the interface.[44] This is widely applied especially in thin film growth of semiconductors.[45] Same occurrence is also found in oxidation of metals and alloys where the precipitates (oxide islands) grow epitaxial to the substrate metals/alloys.[34,46] Recent study revealed that phase separation of perovskite by exposure to laser had also possessed epitaxial relation with the substrate.[47]

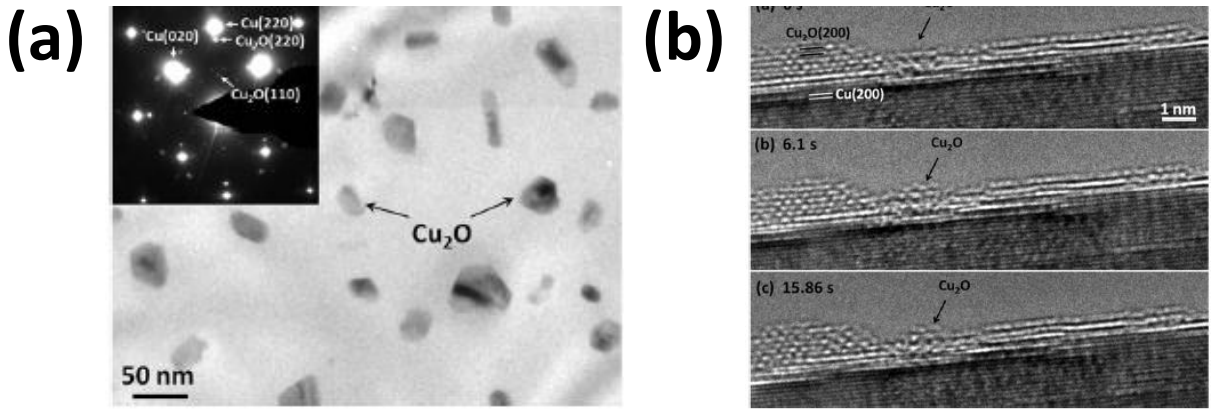


Figure 2.5: Metal-oxide epitaxial of Cu-$CuO_2$ (b) Evolution of oxides islands observed by in-situ TEM. Reproduced from Zhou et. al.[34]

## 2.6 Hydrogen generation reactions

Hydrogen, $H_2$ plays a pivotal role in energy industry as an efficient energy carrier (highest energy content per unit weight = 120.7 kJ $g^{-1}$) as well as a zero-emission fuel.[48] It is also the most important resource for agricultural systems based on ammonia production. Most of the current $H_2$ production relies on catalytic reforming of fossil hydrocarbons (95%) such as methane (*e.g.* $CH_4+H_2O = 3H_2+CO_2$), with only 5% from renewable energy.[49]

One of the promising alternatives for reforming of methane is dry reforming of methane (DRM), as it consumes $CO_2$ as reactant instead of releasing it as in conventional steam reforming of methane (SRM).[50] On the other hand, electrolytic $H_2$ evolution from aqueous solution (Hydrogen Evolution Reaction: HER) can, when driven by renewable electricity from photovoltaic cells (PV) and/or wind power, provide $CO_2$-free $H_2$.[51–53]

# CHAPTER 3

# RESEARCH METHODOLOGY

This chapter is dedicated to elucidate the research plan/approach and describe in detail all experimental procedures conducted within the research.

3.1 Research methodology flowchart

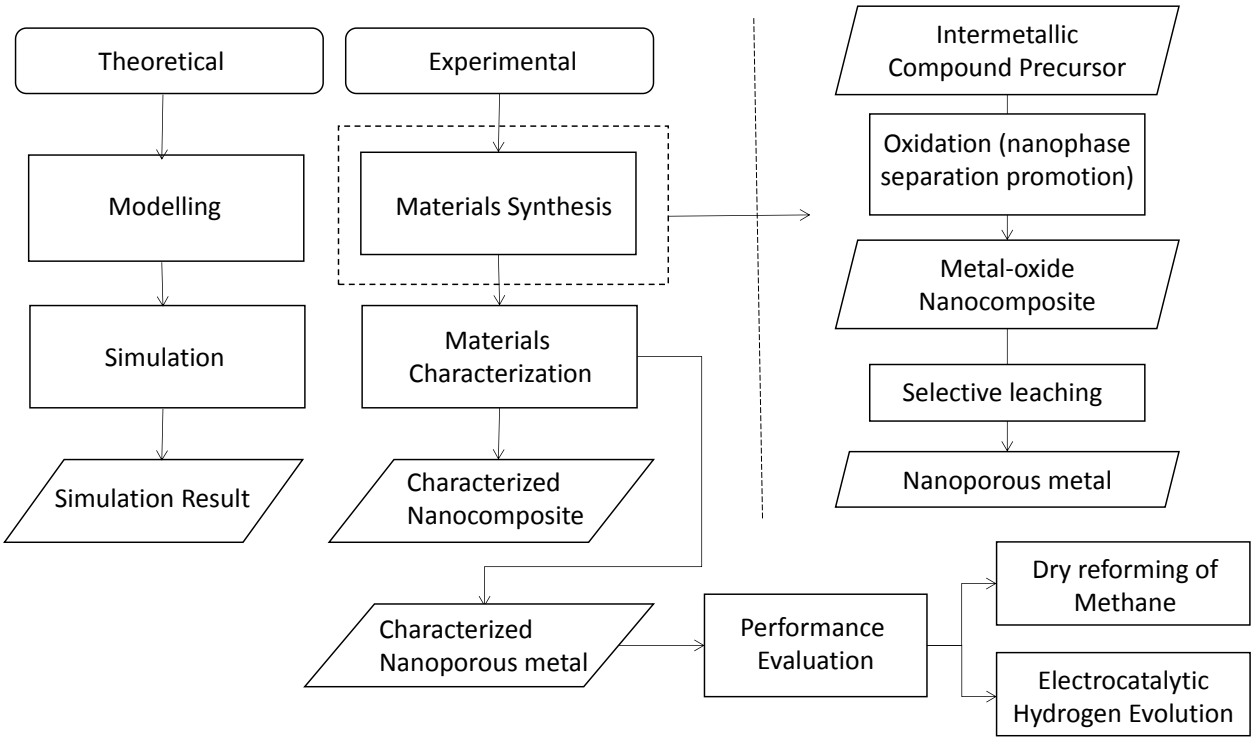


The concept of utilizing nanophase separation in tailoring nanomaterials catalyst was pursued theoretically and experimentally. A primitive reaction-diffusion model, Gray-Scott model, was used to demonstrate phase separation which will be described in 3.2. As for the experimental demonstration of nanophase separation, intermetallic compound comprising of 2 metals i.e., highly stable and oxyphilic metals were used as precursor. Nanophase separation was promoted in oxidative environment at high temperature (3.4.2). The structure of the resulting metal-oxide nanocomposite was then compared with the simulation result. To show the practical utilization of nanophase separation in catalyst tailoring, active faceted nanoporous metallic catalysts was prepared. Through selective leaching, the oxide phase was removed from nanocomposite to produce the nanoporous metallic catalyst (Scheme 3.1).

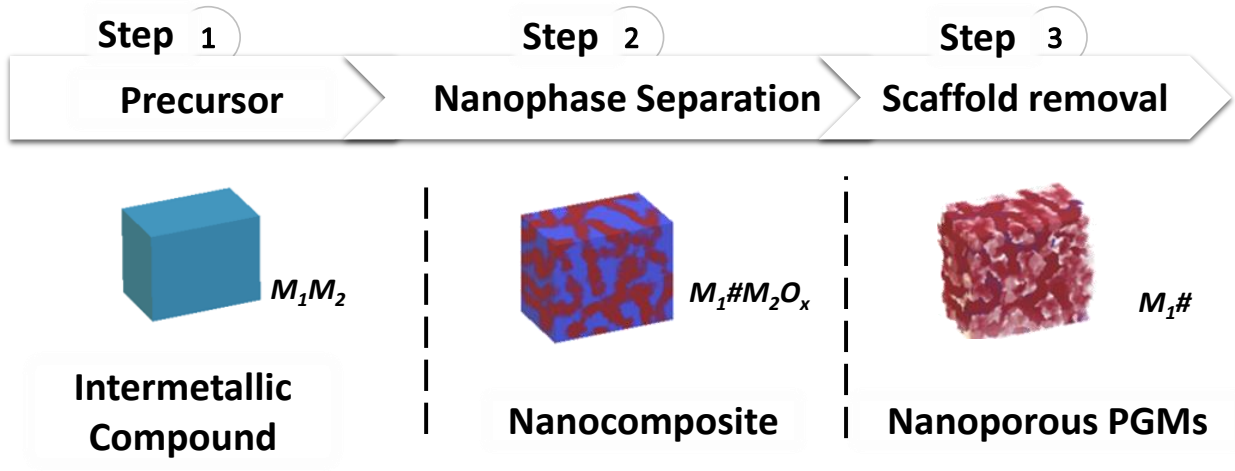


Scheme 3.1: Synthesis route for metallic nanoporous catalyst via nanophase separation

3.2 Modelling and simulation

Gray-Scott model was adopted as a primitive model for nanophase separation phenomenon on the basis of aforementioned similarity with exothermic reaction-diffusion in 2.4. The participating metal and oxide phase were representatively assigned to equation (5). The focus of this approach is to observe the effect of diffusion term (1st term) on the pattern formation (2nd and 3rd terms relate to reaction term which needed thorough studies to specifically establish the oxidation of intermetallic compound. Hence, constants were fixed for all conditions such that the simulation converges into stable solutions).

$$\begin{cases} \frac{\partial u}{\partial t} = d_u \Delta u - uv^2 + F(-u+1) \\ \frac{\partial v}{\partial t} = d_v \Delta v + uv^2 - v(F+K) \end{cases} \quad \text{.....(5')}$$

u, v are the measures for concentration of metal and oxide respectively

$d_u$, $d_v$ are the measures for diffusion rate of metal and oxide respectively

F: constant , K: constant

Simulation of nanophase separation was done based on equation (5') using Mathematica software version 8.0 (see appendix 1 for detailed programming code). Measures of diffusion rate

of metal, $d_u$ and oxide $d_v$ were varied to predict the corresponding pattern formation. In addition, iteration time which corresponds to the reaction time was also manipulated.

## 3.3 Materials

### Material selection

Platinum group metals (PGMs) Pt (plates - Furuya Kinzoku Co.), Ru (chips - 99.9%, Myojokinzoku Inc.), and Rh (powder - 99.99%, Tanaka Kikinzoku Kougyou K.K.) were chosen as starting materials for the nanomaterials catalyst synthesis. Y (chunk - 99.9%, Furuuchi Chemical Corporation) and Ce (chips - 99.9%, Sigma Aldrich Corporation) were used as oxyphilic metal counterpart.

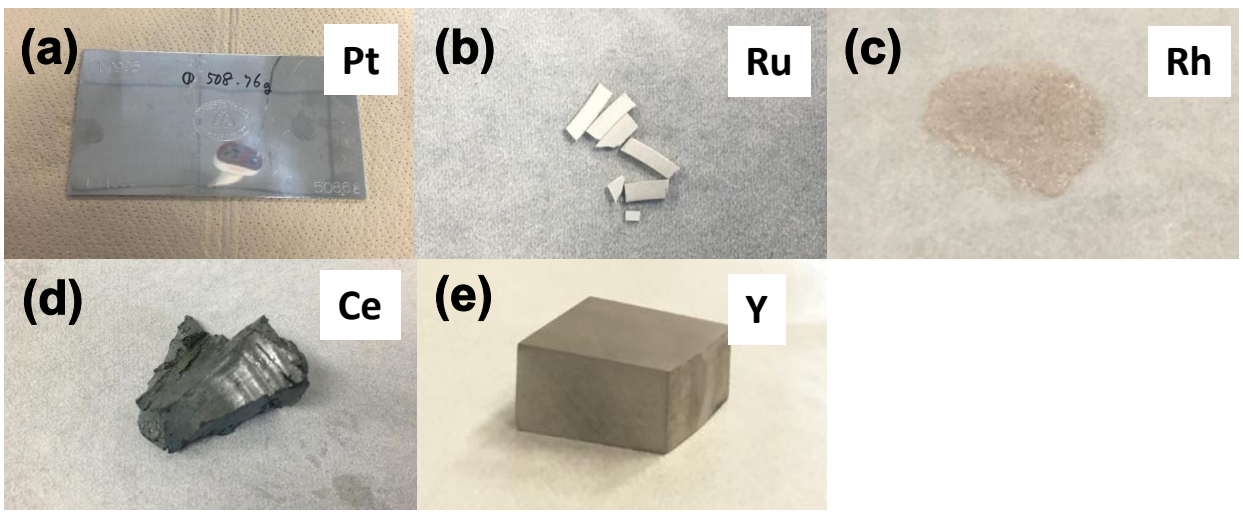


Figure 3.1: (a) Platinum plate (b) Ruthenium chunk (c) Rhodiun powder (d) Cerium chunk (e) Yttrium chunk

## 3.4 Sample Preparation

### 3.4.1 Arc Melting

Depending on the targeted nanomaterials catalyst, starting materials (Pt, Ru, or Rh) were melted with counterpart metals (Ce or Y) in arc furnace (Selec Ltd - SE-11400) to prepare intermetallic compound precursors. The compounds were then crushed with mortar and sieved to get powder of 50 µm - 60 µm in size.

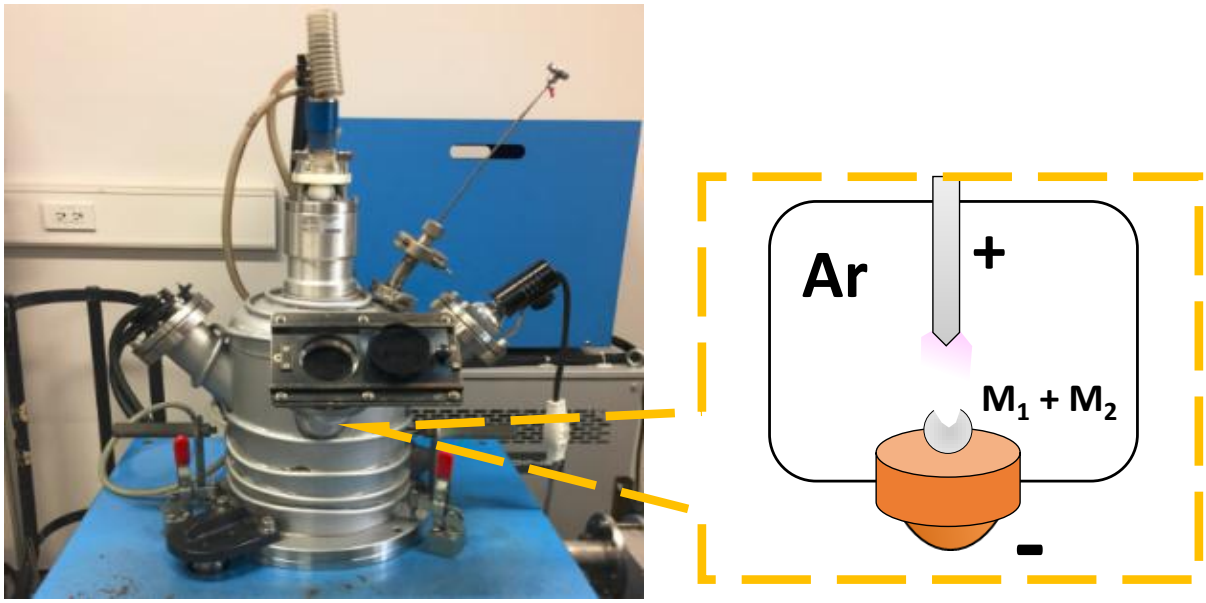


Figure 3.2: Arc furnace for melting

### 3.4.2 Heat treatment

To promote nanophase separation, around 0.4 g of sieved powder (50 µm - 60 µm) was put into ceramic boat and heated at 600°C for 12 hours in the mixture of carbon monoxide (CO), oxygen (O) and argon (Ar) gas (CO:O2:Ar=1:1:98 in volumetric ratio; flow rate = 60 $cm^3s^{-1}$). The treatment was done in tube furnace equipped with temperature controller (Chino-SU). The flowrate of gas mixture (Japan Fine Products Co., Ltd) was controlled with mass flowmeter (Ohkura Electric Co., Ltd - MF1100B).

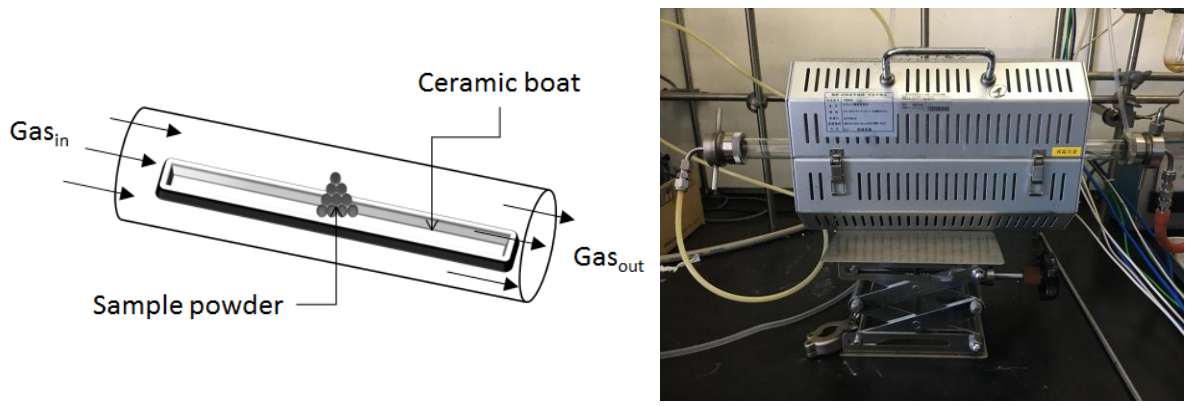


Figure 3.3: Tube furnace setup for controlled oxidation

Table 3.1: Controlled oxidation treatment condition

| **Treatment Condition** | |
|---|---|
| **Temperature** | 600ºC |
| **Time** | 12 hours |
| **Gas ratio** | CO - 2.07%<br>$O_2$ - 1.00%<br>Ar - Balance |
| **Flowrate** | 60 $cm^3s^{-1}$ |

### 3.4.3 Selective leaching

The resulting metal-oxide nanocomposite was then treated in acid solution to selectively leach oxide phase. $Y_2O_3$ was leached by immersing the powder in 69% $HNO_3$ (Wako Pure Chemical Industries, Ltd.) at room temperature while the leaching $CeO_2$ was done with a more extreme condition of 95% $H_2SO_4$ (Wako Pure Chemical Industries, Ltd.) at 150ºC. The leaching was done in beaker stirred with magnetic stirrer and after 6 hours, the solution was transferred into centrifuge tube with addition of 20 ml ultrapure water. The tube was centrifuged in table top centrifugal machine (Kubota Co., Ltd – AT-508C) at 1600 rpm for 10 minutes. Solution was discarded while the sludge was again diluted with ultrapure water and centrifuged. This step was repeated for 3 times and the final sludge was dried in electric drying oven (ADVANTEC-DRA630DA) at 80ºC overnight.

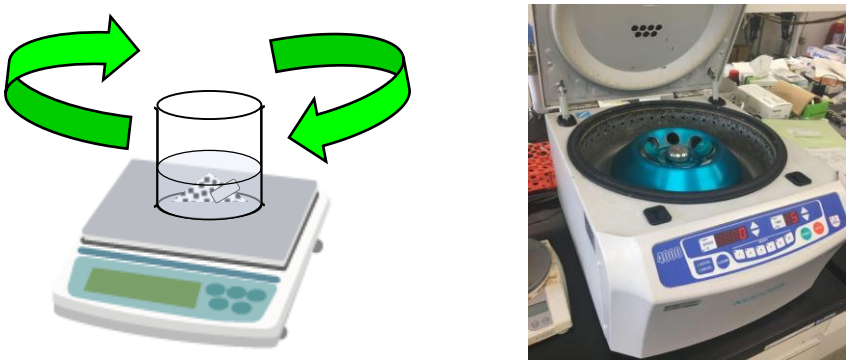

Figure 3.4: Selective leaching process

Table 3.2: Selective leaching condition

| **Treatment Condition** | $Y_2O_3$ Leaching | $CeO_2$ Leaching |
|---|---|---|
| **Leaching Agent** | $HNO_3$ (69%) | $H_2SO_4$ (95%) |
| **Concentration** | 69% | 95% |
| **Temperature** | Ambient | 150ºC |
| **Time** | 6 hours | 6 hours |

## 3.5 Materials Characterization

### 3.5.1 *p*XRD and HAXPES

Powder XRD was collected with PANalytical X'Pert PRO (Cu Kα, 45 kV, 30 mA). Samples were scanned in the 2θ range from 10º to 100º in steps of 0.0857º $s^{-1}$. The resulting x-ray diffraction spectra were analyzed using software (Highscore – PANalytical B.V.). Surface characters of the samples were investigated by using Hard XPS (HAXPES) conducted at Spring8 (BL15XU). Excitation energies for the scan range from 5630 eV to 5650 eV with step of 0.05 eV.

### 3.5.2 Electron Microscopy

Sample morphology and elemental analysis was conducted by using EDS detector attached FE-SEM (Hitachi SU-8230). TEM (JEM-2100F1) was also used for higher magnification image and EDS elemental mapping was done in STEM mode. Fast Fourier Transform (FFT) analysis was applied (Gatan software) to identify the crystal orientation. All samples were trimmed to the thickness of 70 nm with FIB (JEM-9320FIB) prior to TEM observation. In situ observation was conducted using reaction science high-voltage scanning transmission electron microscope (JEM-1000K RS) at High Voltage Electron Microscope Laboratory in Nagoya University.

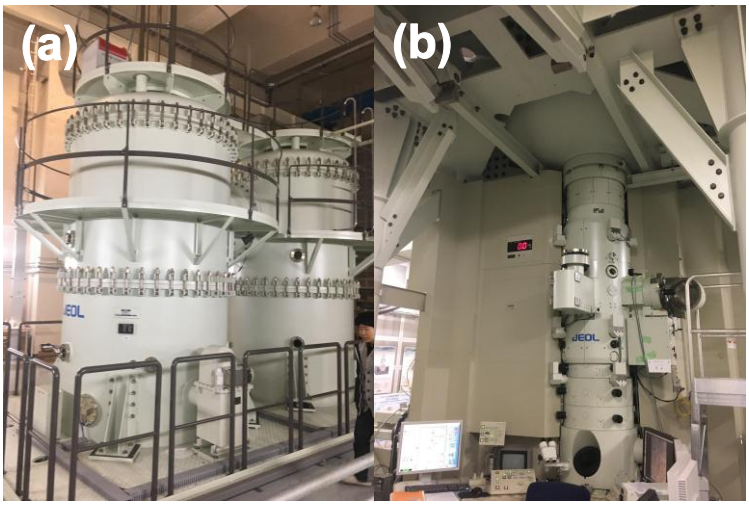


Figure 3.5: reaction science high-voltage scanning transmission electron microscope (JEM-1000K RS) at High Voltage Electron Microscope Laboratory in Nagoya University (a) Upper deck – Electron gun (b) Lower deck – Operation room

### 3.5.3 $N_2$ Physisorption

$N_2$ physisorption was conducted with Micromeritics ASAP 2010 analyzer at 77 K to get the adsorption/desorption isotherm, Brunauer-Emmett-Teller (BET) surface area and Barrett, Joyner, and Halenda (BJH) pore distribution. Degassing at 423 K for 3 hours was carried out to eliminate surface impurities prior to the analysis.

## 3.6 Catalytic Performance Evaluation

### 3.6.1 Dry reforming of Methane

Dry reforming of methane was conducted in a fixed bed reactor (Micromeritics-MAE). An aliquot of 0.1 g of sample was loaded in a quartz reactor (inner diameter = 10 mm). Then gas mixture of $CH_4/CO_2/Ar$ (1/1/98 in vol %) with a flow rate of 100 mL $min^{-1}$ was introduced into the reactor. The reaction temperature was raised to 683 K to evaluate the DRM performance. Online GC system (Shimadzu GC-8A), equipped with a TCD and a packed column (active carbon, 60-80 mesh (GL Sciences); 3 mm x 3m), was used to analyze the output stream, which was collected with a 1 mL sampling loop. The $CH_4$- and $CO_2$ conversion rates were calculated as follows:

$$\boldsymbol{CH_4 Conversion}\ [\%] = \frac{\boldsymbol{mol\ of CH_4 input - mol\ of CH_4 output}}{\boldsymbol{mol\ of CH_4 input}} \times \mathbf{100}$$

$$\boldsymbol{CO_2 Conversion}\ [\%] = \frac{\boldsymbol{mol\ of CO_2 input - mol\ of CO_2 output}}{\boldsymbol{mol\ of CO_2 input}} \times \mathbf{100}$$

### 3.6.2 Electrocatalytic Hydrogen Evolution Reaction

Electrochemical investigation was carried out using three-electrode cell equipped with CH Instrument (CHI 842B) potentiostat. A mixture of distilled water (398 ml), propanol (100 ml), Nafion (2 ml), and catalyst (2.5 mg) was prepared and sonicated for 10 minutes to obtain an ink. The ink (5 ml) was then dropped to coat the working electrode (glassy carbon electrode) and left to dry in a furnace at room temperature. The prepared working electrode was then placed in an electrochemical cell together with a counter electrode (Pt wire, diameter = 1 mm) and a reference electrode (Ag/AgCl). All potentials were converted to RHE by adding a value of 0.195+0.059pH (reference value at 25°C). The electrochemical studies for HER were conducted in 0.5 M $H_2SO_4$ solution under argon, at 25°C. Counter electrode of graphite was used as control. In addition, HER with perchloric acid ($HClO_4$) 0.1M as electrolyte was also done as control.

The electrochemical surface area (ESCA) was quantified by measuring the double-layer capacitance by cyclic voltammetry (CV). The CV curves in a non-faradaic region (-0.2 to 0.34 V) were plotted as a function of various scan rates. The double layer capacitance ($C_{dl}$) was evaluated from the slope of the linear regression between the current differences in the middle of the potential window of CV curves versus the scan rates (20, 40, 60, 80, 100 mV/s; see Figure S19) as $i = v.C_{dl}$. Based on the literature reported $C_s$ values is generally materials, 0.035 mF $cm^{-2}$ was considered for EASA calculation.[54–56] The ECSA value was obtained by dividing $C_{dl}/C_s$ with the loading weight of the catalyst.[57]

Electrochemical impedance spectra (EIS; Nyquist plot) at a potential of -0.4 V over the frequency range of 0.01 Hz–100 kHz was also carried out with 0.5 m $H_2SO_4$ solution as electrolyte and graphite as counter electrode. For stability evaluation, chronogalvanometry and chronoamperometric was done in 0.5 M $H_2SO_4$ solution. The former was done at +10 mA for 6 hours, while the latter was done for 1 hours and the current retention was recorded and plotted.

Cu underdeposition was adopted to calculate turnover frequency (TOF). [58,59] TOF=I/(2Fn), where I is the current (A) during HER linear sweep measurement, F is the Faraday constant (C $mol^{-1}$), n is the number of active sites (mol). Since $n=Q_{Cu}/2F$, TOF calculation is simplified as $TOF = I/Q_{Cu}$. $Q_{cu}$ was obtained from integration of curve related to Cu monolayer stripping only.

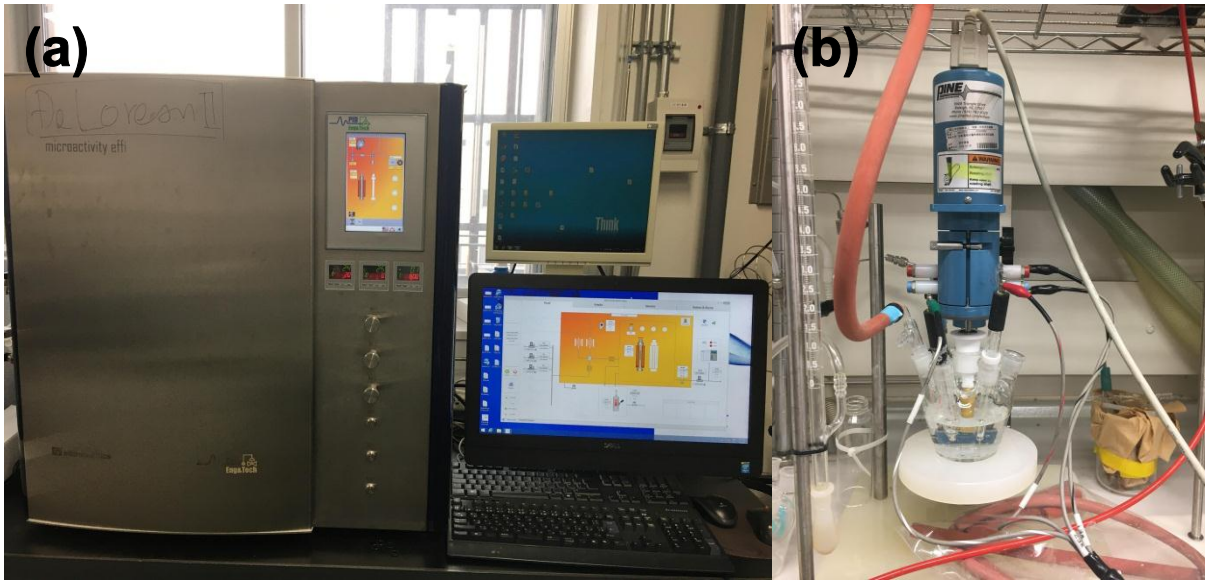


Figure 3.6: (a) Thermocatalysis reactor for DRM (b) Electrocatalysis setup for HER

# CHAPTER 4

# NANOPHASE SEPARATION CONCEPT

This chapter aims to shed light on the concept of nanophase separation phenomenon as a tool for surface tailoring. Gray-Scott model was adopted to simulate the pattern formation in reaction-diffusion process. Measures of diffusion coefficients were varied to understand the pattern formation trend. The simulated trend from Gray-Scott model was taken into comparison with the emerged pattern of nanocomposites promoted by nanophase separation considering that it is also a form of reaction-diffusion process. This is followed by real-time observation of nanophase separation phenomenon in representative precursor ($Pt_5Ce$) by conducting in situ TEM in oxidative atmosphere at elevated temperature. Finally, the proposed mechanism of nanophase separation is discussed.

## 4.1 Reaction-Diffusion Simulation

As mentioned in 3.2, the morphogens of u and v was assigned to metal and oxide phase. By changing the measure of diffusion rate of metal (du) and oxide (dv), the obtained pattern from the simulation was identified (Figure 4.1) (Hue color was used – Red → Blue → Green → Red, thus, u and v boundary = blue and green boundary). At the same diffusion rate, phase separation barely showed any defined pattern (Figure 4.1a). By decreasing dv, a more defined pattern of phase separation was obtained. Connected oxide phase v in green started to emerge at du = 0.1 and dv = 0.025, followed by lamellar pattern (dv = 0.020) and maze pattern (dv = 0.017). Further decreased value of dv resulted in discontinuity of the phases, and finally yielded spot pattern nucleation. This trend was as pointed out by Turing et. al. in describing the phase separation as a diffusion driven instability process, i.e. higher difference in diffusion rate between morphogens accelerate the phase separation. [25,26]

Simulation was also done to investigate the resulting pattern by changing the du value. As shown in Figure 4.2, the phase area was larger compared to lower value of du while maintaining the same du/dv ratio (Figure 4.1f and 4.2c). Clearer visual of spot nucleation was identified at greater difference of du and dv.

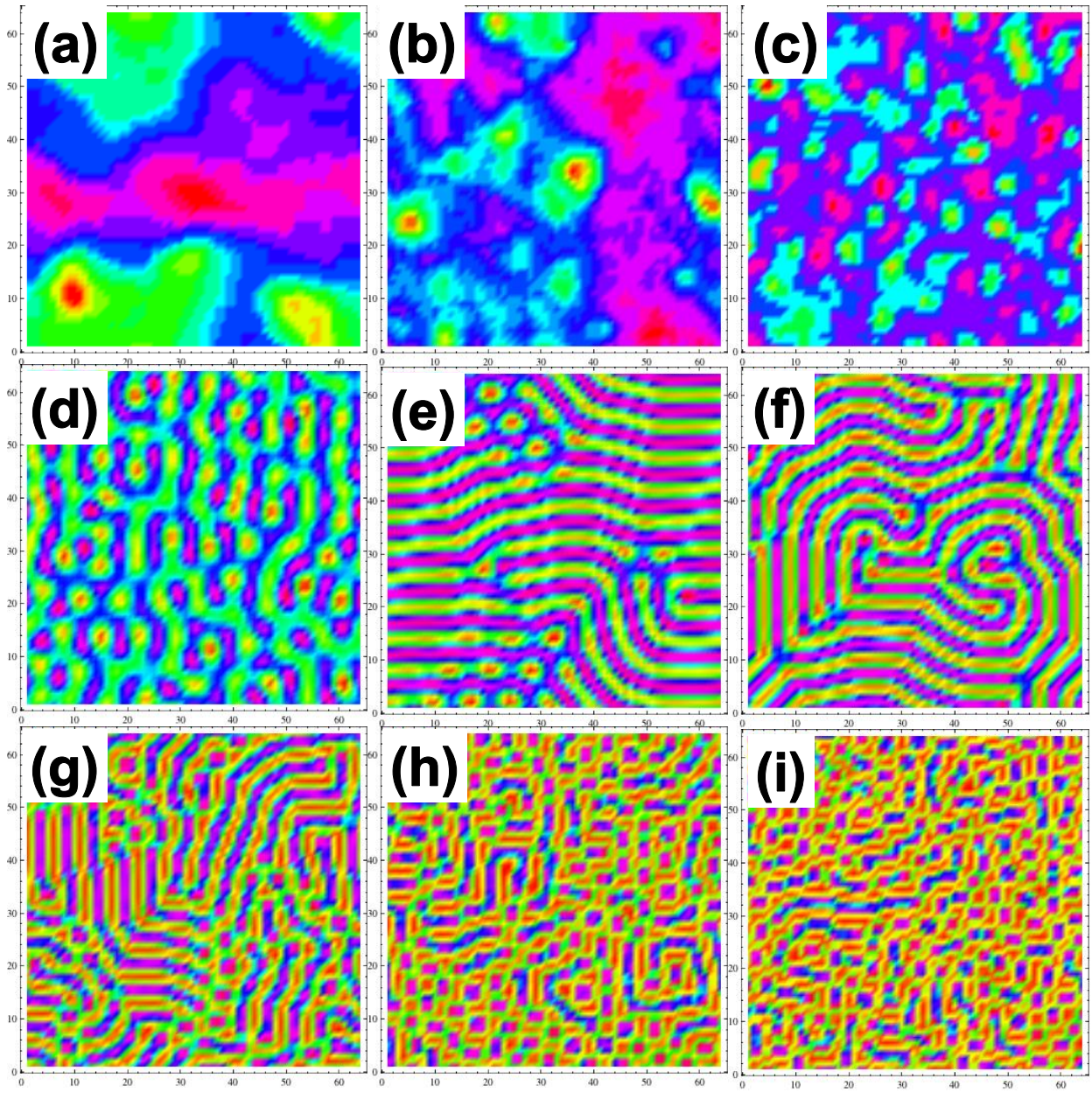


Figure 4.1: Simulation result of nanophase separation with condition K= 0.04, F= 0.017, du = 0.100, (a) dv = 0.100, (b) dv = 0.050, (c) dv = 0.033, (d) dv = 0.025 (e) dv = 0.020, (f) dv = 0.017, (g) dv = 0.014, (h) dv = 0.013, (i) dv = 0.011. Color is based on hue (Red → Blue → Green → Red)

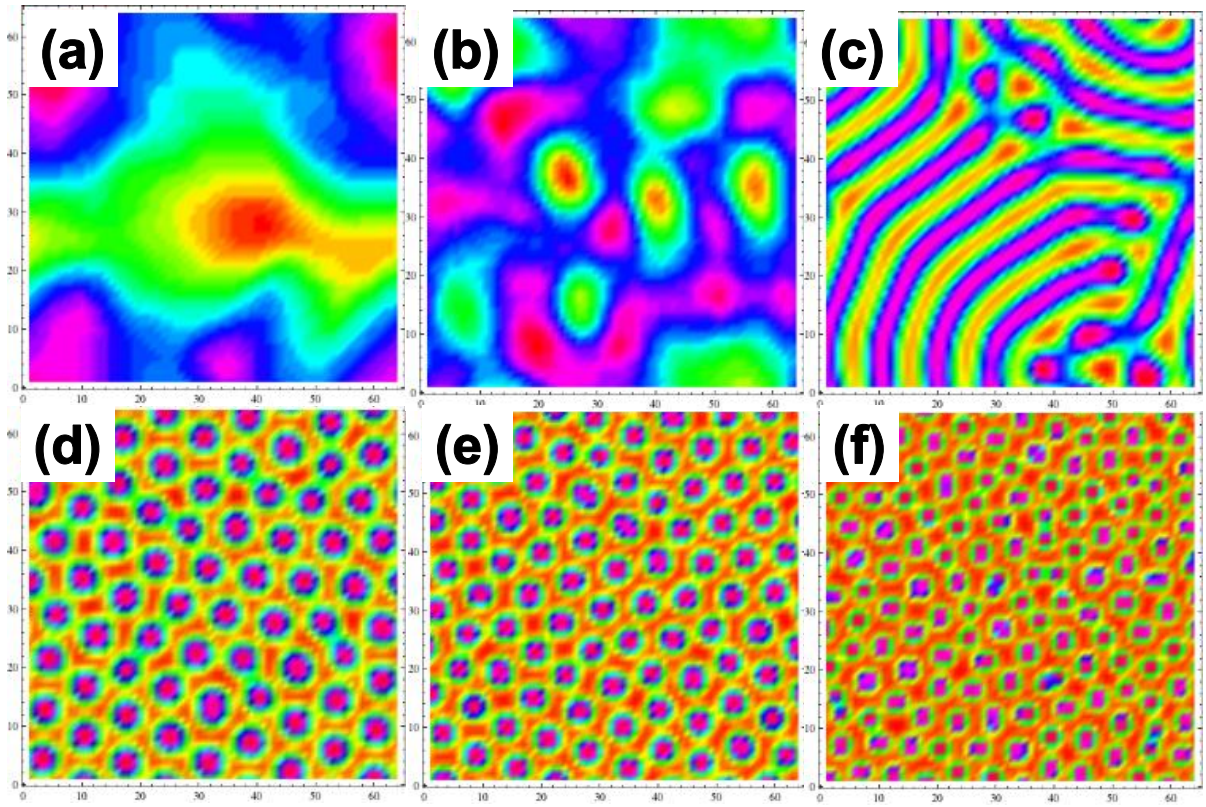


Figure 4.2: Simulation result of nanophase separation with condition K= 0.04, F=0.017 ,du = 0.300, (a) dv = 0.300, (b) dv = 0.100, (c) dv = 0.050, (d) dv = 0.033 (e) dv = 0.025. Color is based on hue (Red → Blue → Green → Red)

The simulation of pattern evolution as time was increased is presented in Figure 4.3. This was done by manipulating the iteration times (single iteration, dt = 0.01). At 1000 times iteration, a localized separation was seen, and as the iteration times are increased, the phase segregated to form a more defined patterns (in this case, lamella pattern as du and dv was selected based on previous dv/du ration investigation). After 1,000,000 iterations (Figure 4.3h), the pattern showed insignificant change compared to 3,000,000 iterations (Figure 4.3i) indicating system has achieved stability.

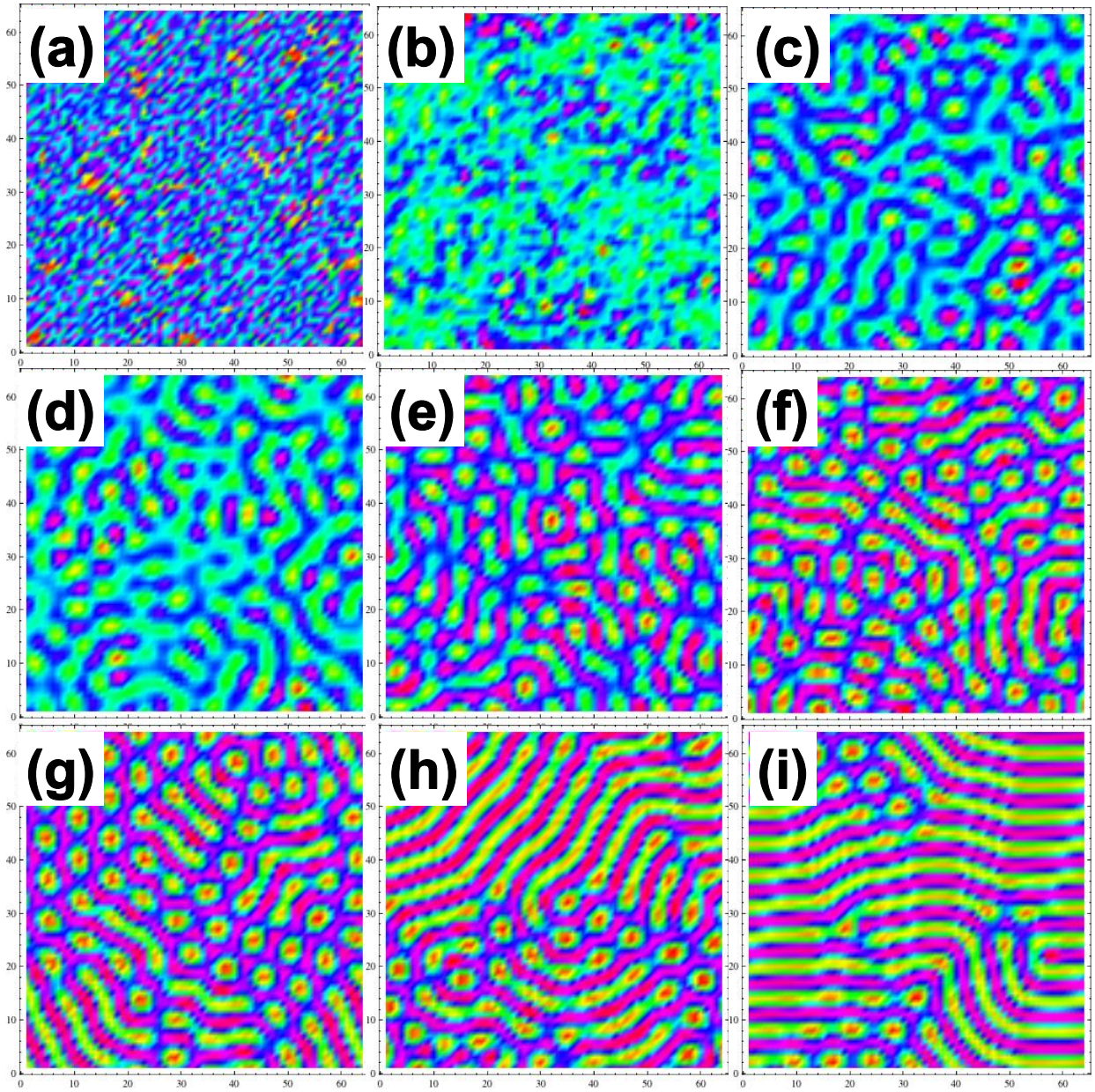


Figure 4.3: Simulation result of nanophase separation with condition K= 0.04, F=0.017, du = 0.300, dv = 0.060, dt = 0.01, iteration times = (a) 1000, (b) 5000, (c) 25,000, (d) 50,000 (e) 100,000, (f) 250,000, (g) 500,000, (h) 1,000,000, (i) 3,000,000. Color is based on hue (Red → Blue → Green → Red)

4.2 Nanophase separation of $Pt_5Ce$ precursor into Pt-$CeO_2$ nanocomposite

In situ TEM was carried out to demonstrate the actual occurrence of nanophase separation phenomenon. Sample used was the 80-90 nm FIB trimmed $Pt_5Ce$ intermetallic compound. At 500ºC, 0.1 Pa of oxygen gas was channeled onto the precursor while being observed with TEM. Area with minimum deformation was selected to be observed in order to see the phenomenon clearly. Figure 4.4a and 4.4b show the surface texture before and after nanophase separation respectively at low magnification. Initially homogeneous surface of $Pt_5Ce$ completely transformed into lamellar textured surface after oxygen was supplied and this covers all area.

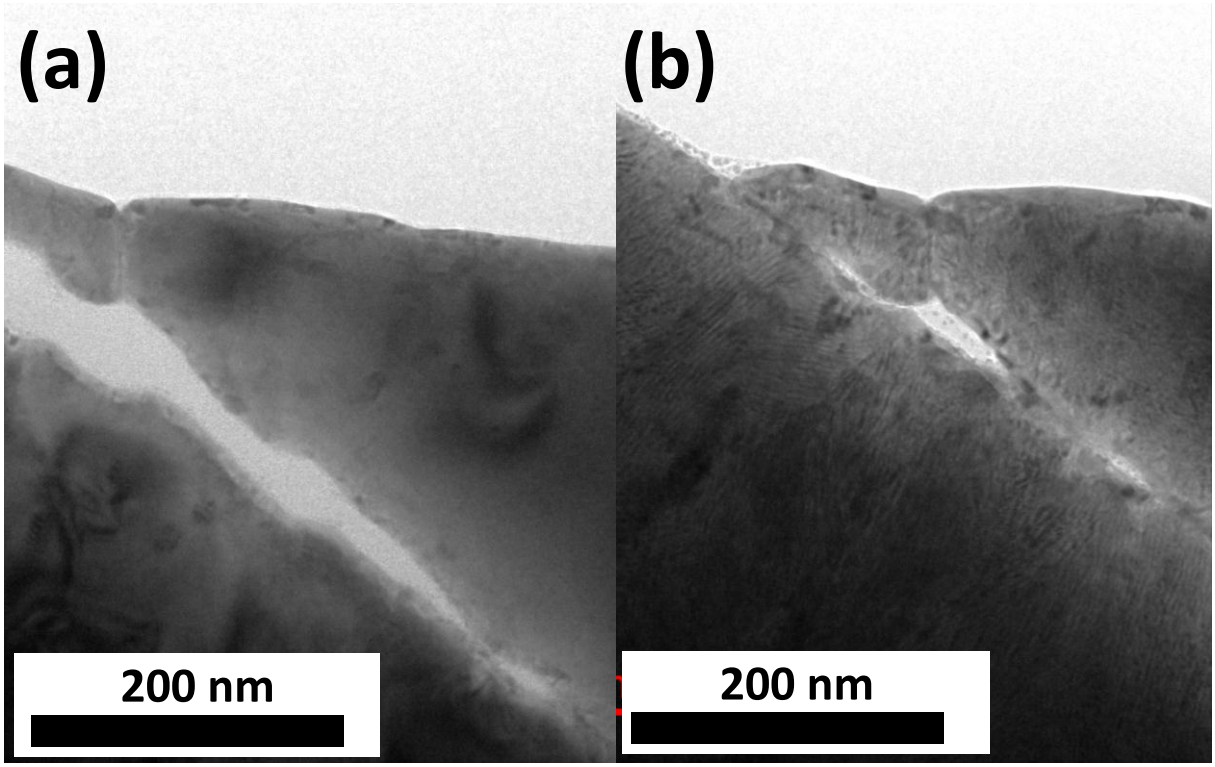


Figure 4.4: TEM image of $Pt_5Ce$ precursor (a) before, and (b) after being exposed to oxygen (0.1 Pa) at 500ºC

Figure 4.5 is the higher magnification of TEM images and their corresponding diffraction patterns, before and after nanophase separation. It is clear from the diffraction patterns (Figure 4.5c, d) that in the beginning, $Pt_5Ce$ possessed a diffraction pattern corresponded to $Pt_5Ce$ crystal which at this high magnification covered a single crystal (one grain). After nanophase separation, a diffraction ring consisting Pt and $CeO_2$ was seen, indicating the complete transformation into biphasic polycrystalline Pt-$CeO_2$ nanocomposite.

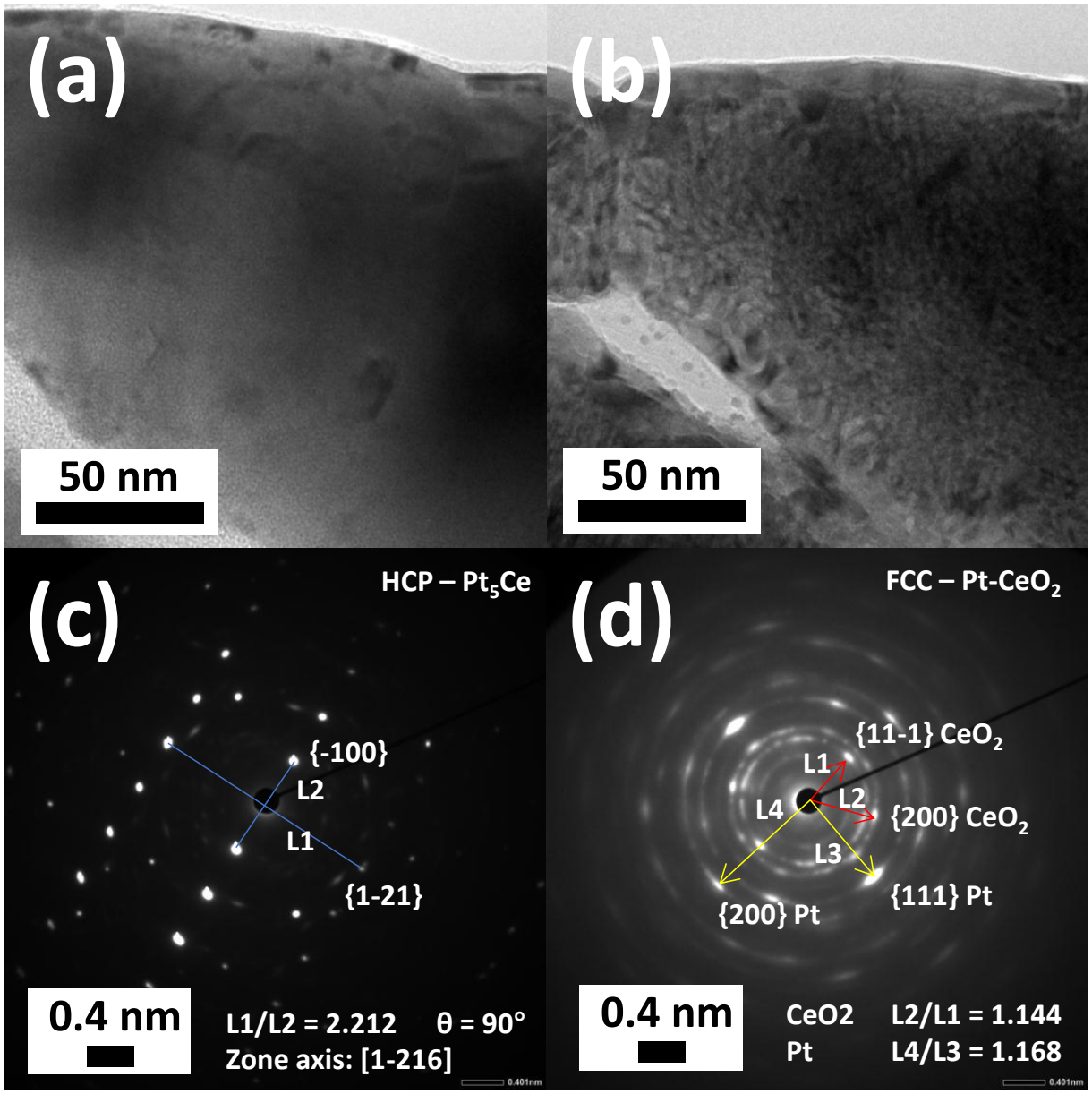


Figure 4.5: TEM image of $Pt_5Ce$ precursor (a) before, and (b) after (higher magnification), and diffraction pattern (c) before, and (d) after being exposed to oxygen (0.1 Pa) at 500ºC

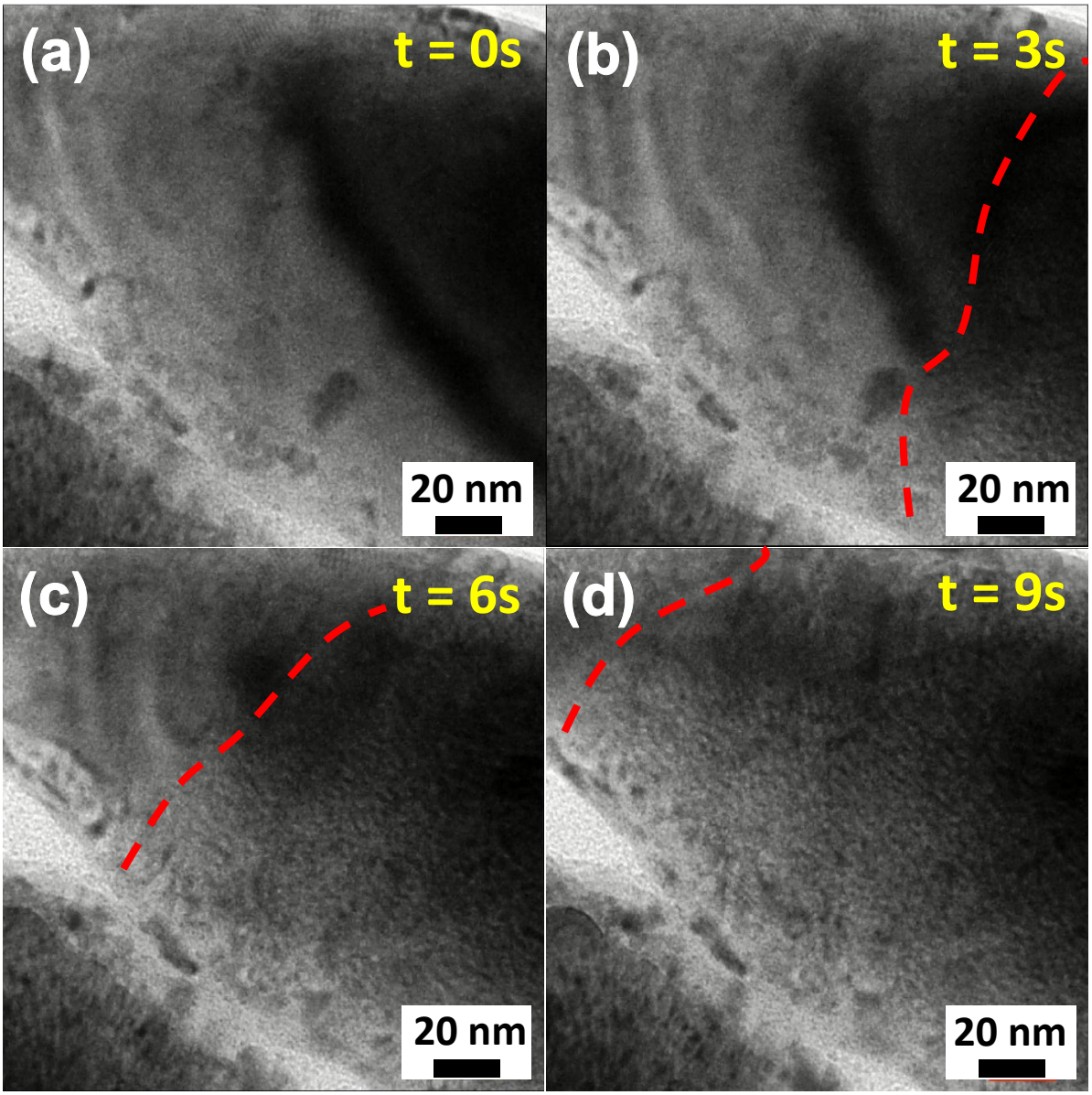


Figure 4.6: In situ TEM image capture of $Pt_5Ce$ precursor evolution to Pt-$CeO_2$ nanocomposite after being exposed to oxygen (0.1 Pa) at 500ºC

The propagation of nanophase separation was observed using the in situ TEM and the captured images are presented in Figure 4.6. The propagation front was marked with broken lines in red, whereby nanophase separation was recorded to propagate at around 20 nm $s^{-1}$ throughout the surface. No significant change of texture was observed after the nanophase separation. It also noted that Pt-$CeO_2$ nanocomposite developed parallel to the propagation direction forming elongated/lamella phase. Since the transformation was irreversible, it is logical to predict that if 2 waves/propagation fronts meet, the effect would be that of non-annihilation mode.

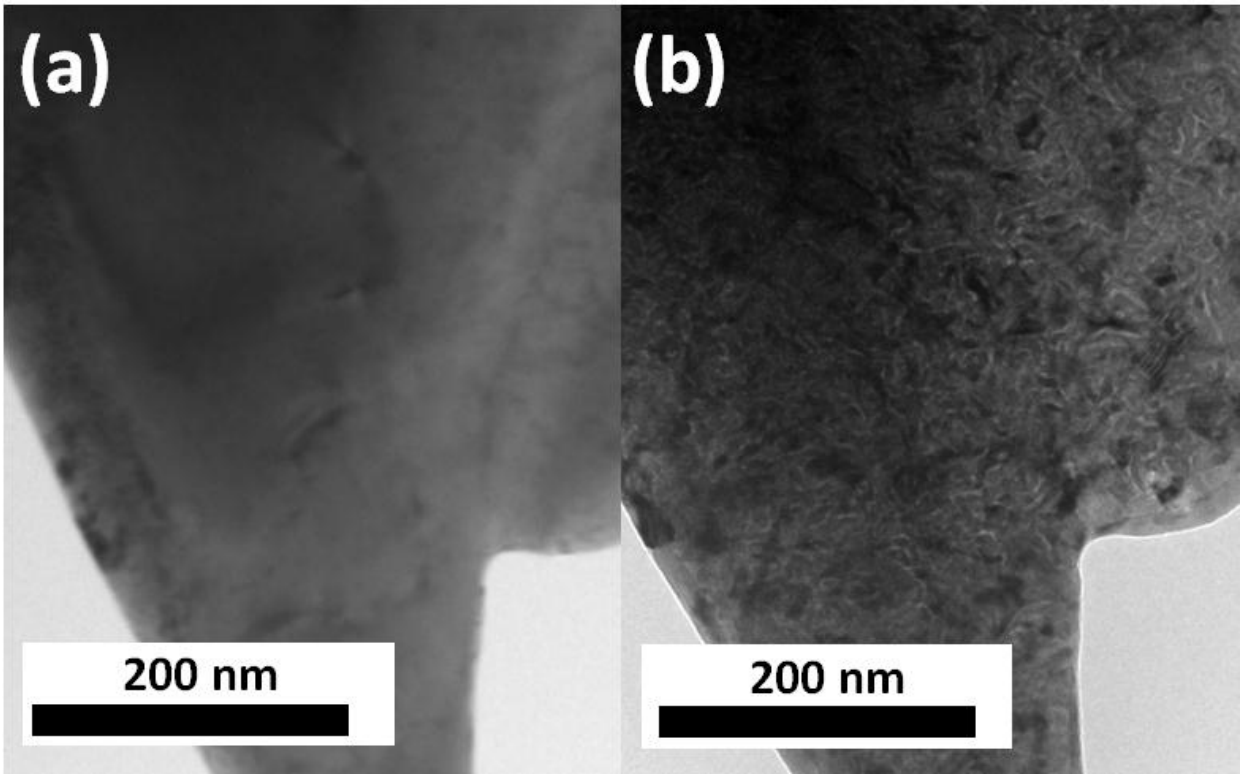


Figure 4.7: TEM image capture of $Pt_5Ce$ precursor evolution to Pt-$CeO_2$ nanocomposite after being exposed to mixture gas (2%CO: 1%O: 97%Ar -50 Pa) at 500ºC

Nanophase promotion was also conducted by using mixture gas (2%CO: 1%O: 97%Ar -50 Pa) at 500ºC. CO gas acted as reducing component in the gas mixture to control the spontaneous propagation of nanophase separation. The resulting texture after the exposure to mixture gas was shown in Figure 4.7b. Unlike the treatment in pure $O_2$, the lamellar direction was rather randomly oriented. Higher magnification observation with diffraction pattern confirmed the transformation from $Pt_5Ce$ precursor to nanocomposite Pt-$CeO_2$ (Figure 4.8). In addition, in situ

TEM observation revealed a relatively slower and non-directional development of nanocomposite (Figure 4.9). This could be associated with the presence of CO gas which could suppress the oxidation to occur at slower rate.

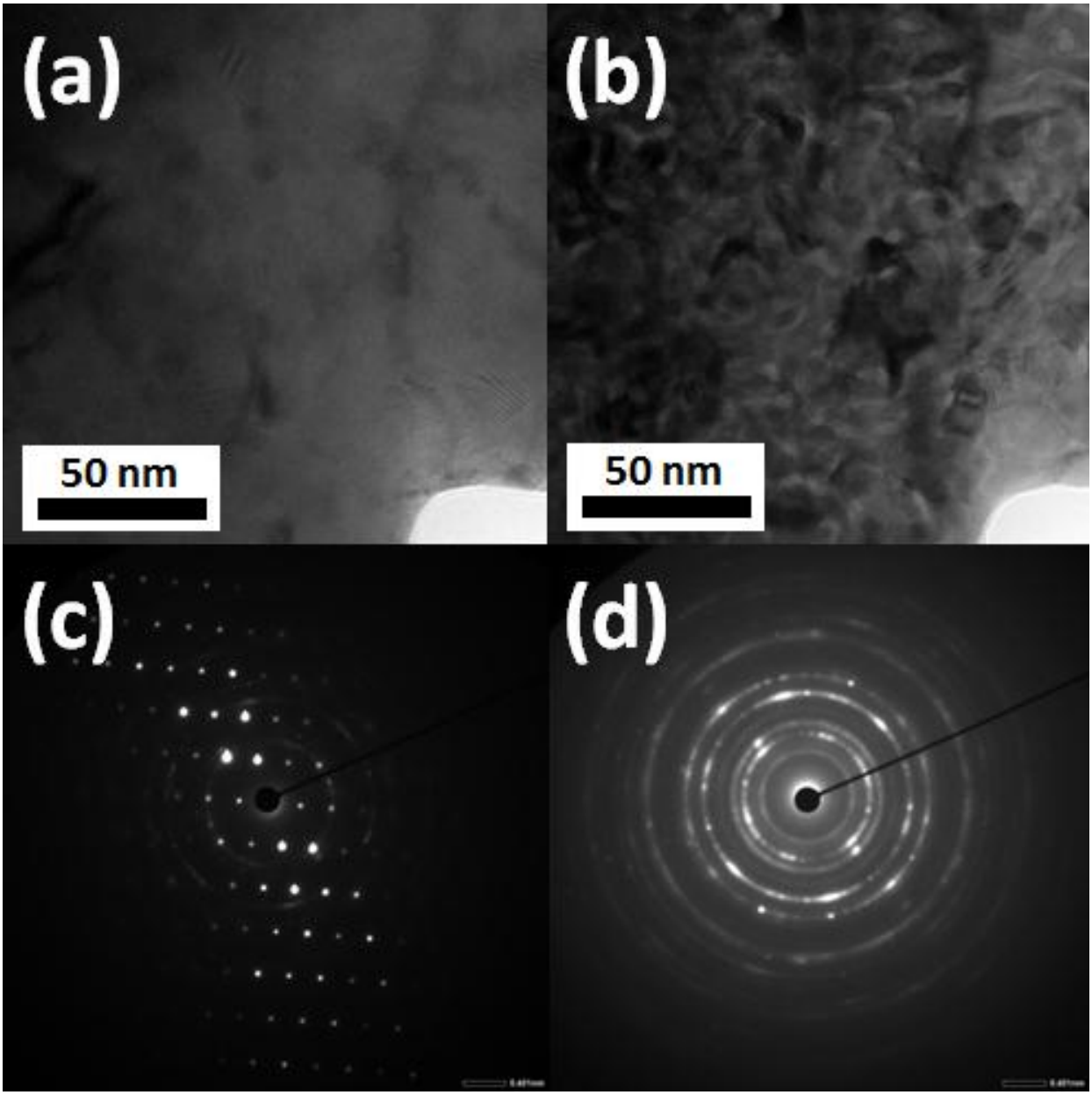


Figure 4.8: TEM image of $Pt_5Ce$ precursor (a) before, and (b) after (higher magnification), and diffraction pattern (c) before, and (d) after being exposed to mixture gas (2%CO: 1%O: 97%Ar - 50 Pa) at 500ºC

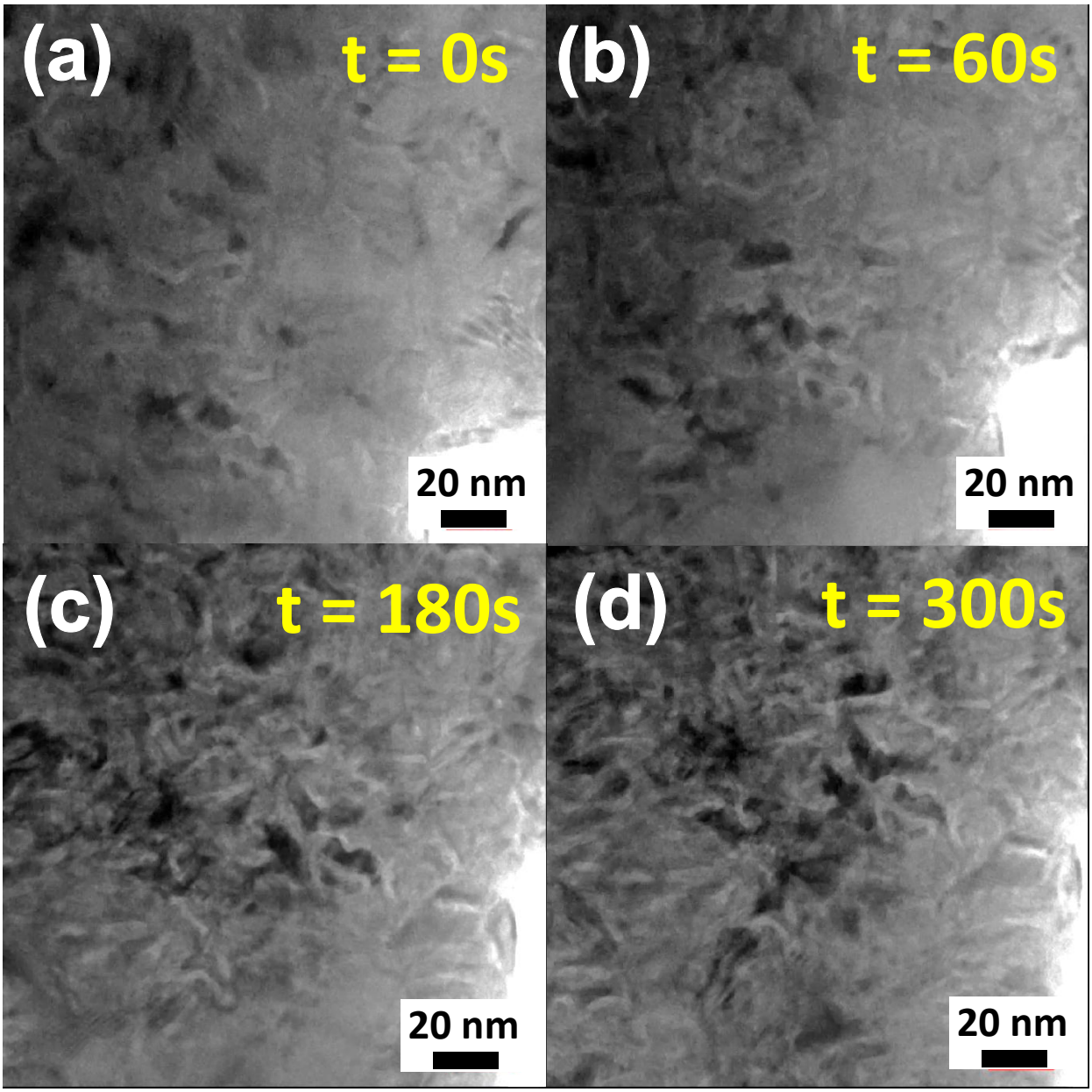


Figure 4.9: In situ TEM image capture of $Pt_5Ce$ precursor evolution to Pt-$CeO_2$ nanocomposite after being exposed to mixture gas (2%CO: 1%O: 97%Ar -50 Pa) at 500ºC

4.3 Proposed mechanism of nanophase separation

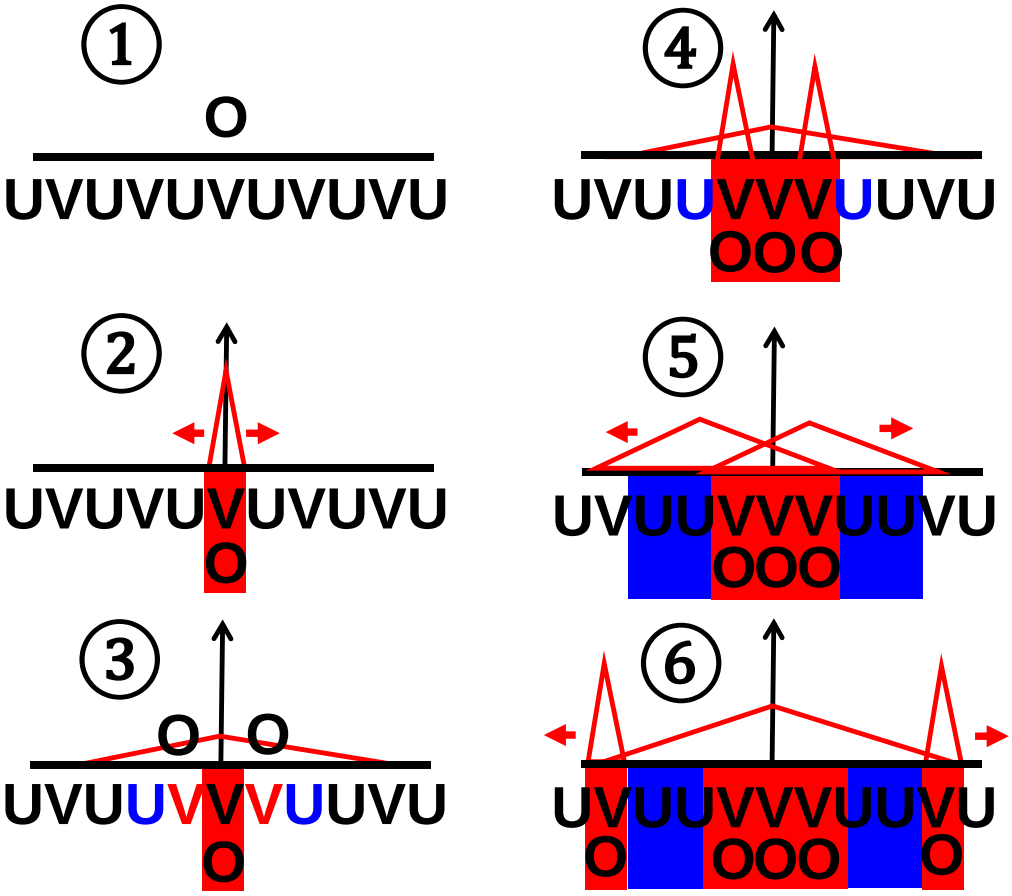


Figure 4.10: Proposed mechanism of nanophase separation

The proposed mechanism of nanophase separation induced by oxidation in intermetallic compound is illustrated in Figure 4.11. At high temperature, when $O_2$ was adsorbed on the surface ① and diffuse into the IMC, it reacts with element having high affinity towards oxygen (V) forming oxide. Since oxidation is an exothermic reaction, the oxidation caused heat to be released creating hot spots ②, attracting more V atoms for further oxidation ③, creating more hot spots. When the adjacent region depletes of V atoms, the unoxidized U atoms accumulated forms alternating phase ⑤. As heat continues to spread beyond U phase, new oxidation spots are triggered upon the availability of V atoms ⑥.

# CHAPTER 5

# NANOPOROUS METALLIC CATALYST TAILORING FOR HYDROGEN GENERATION

This chapter is dedicated to demonstrate the practical application of nanophase separation as a tailoring technique in synthesizing efficient nanoporous catalysts for hydrogen production. The synthesis strategy is as per described in chapter 3. At first, the characterization of nanocomposites that was produced from the promotion of nanophase separation, including the metal oxide interface condition will be presented. This is followed by the characterization of the obtained nanoporous metal after selective leaching, and finally catalytic performance demonstration with dry reforming of methane (DRM) and electrocatalytic hydrogen evolution reaction (HER). Nanoporous Rh was synthesized to be tested for DRM, while nanoporous Ru was tested for electrocatalytic HER performance.

## 5.1 Characterization of nanocomposite

Selective oxidation was conducted at 600ºC in $CO:O_2:Ar$ (2%:1%:97%) gas for 12 hours. TEM observation showed that oxidized (nanophase separation promoted) $Pt_5Ce$ precursors (cross-section) exhibited phase separation throughout all areas at nanoscale order (Figure 5.1). Scanning transmission electron microscopy (STEM) mode was also used along with elemental mapping using EDS to clearly identify the phase. Bright- and dark contrasted areas in Figure 5.2a correspond to the Pt and $CeO_2$ phase, respectively, as supported by compositional mapping (Figure 5.2b, c, d). This is also confirmed by the *p*XRD spectra which revealed that all precursors were completely transformed into corresponding metals and $CeO_2$ after they were oxidized as all peaks corresponding to $Pt_5Ce$ precursor were completely replaced by individual peaks of Pt and $CeO_2$ (Figure 5.3).

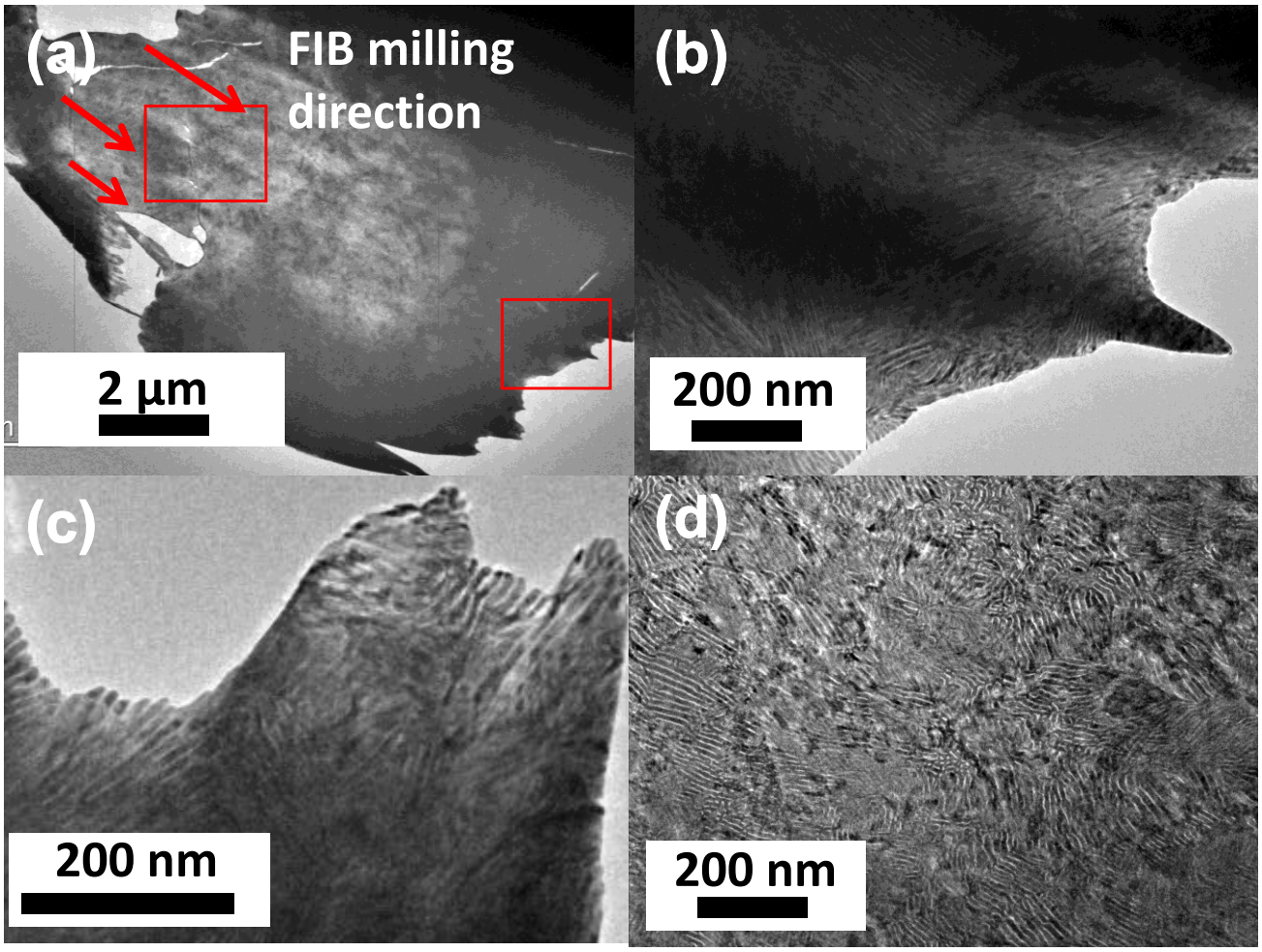


Figure 5.1 TEM image of cross-sectioned Pt-$CeO_2$ nanocomposite.

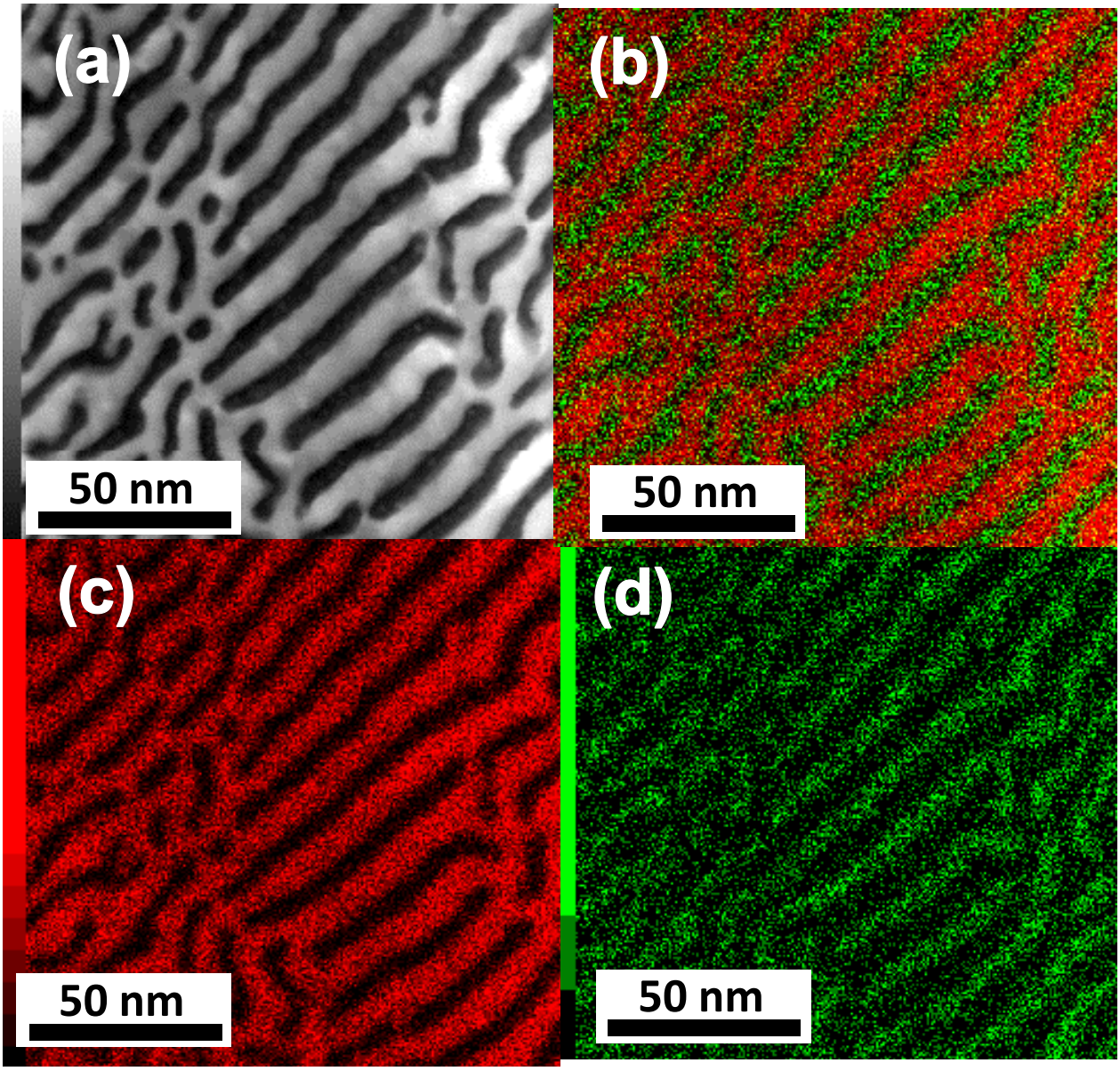


Figure 5.2 (a) STEM image, (b), (c), (d) elemental mapping of cross-sectioned Pt-$CeO_2$ nanocomposite. Pt = red, Ce = green)

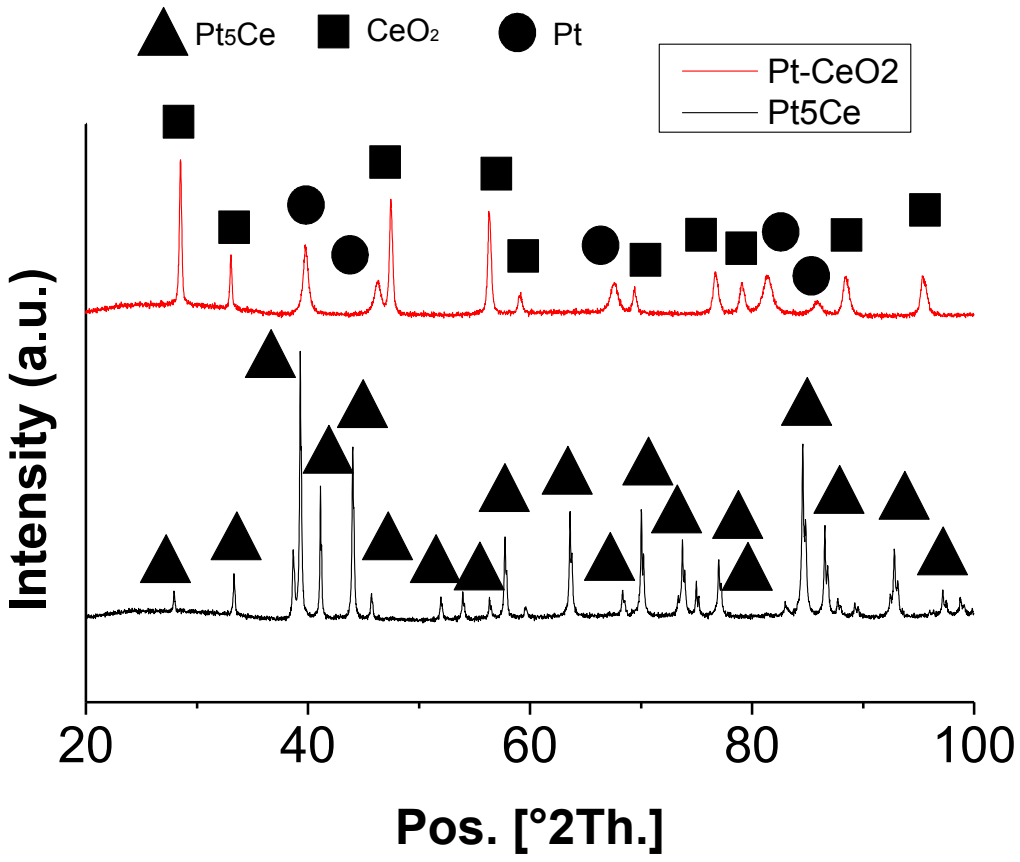


Figure 5.3: *p*XRD result of $Pt_5Ce$ and Pt-$CeO_2$ nanocomposite

$Ru_2Ce$ precursor showed similar emergence of lamella structure after being oxidized with the exactly the same condition with $Pt_5Ce$. Lamellar was elongated normal to the surface which could be related to the diffusion direction of oxygen. Figure 5.5 shows STEM observation and EDS analysis. It is noticed that the size of the lamellar in Ru-$CeO_2$ nanocomposite was finer/thinner compared to the one that of Pt-$CeO_2$ nanocomposite. This could be associated with the amount of metal in the precursor. $Pt_5Ce$ had 5 times molar ratio to cerium compared to 2 times in $Ru_2Ce$. As per discussed in in previous chapter, oxidation of Ce caused the adjacent area to be depleted of Ce atoms, thus creating Ru phase area. Low amount of Ru atoms caused the alternating lamellar became finer as Ce atoms became available for further oxidation at shorter gap compared to $Pt_5Ce$. Same as Pt-$CeO_2$, *p*XRD result of Ru-$CeO_2$ showed individual Ru and $CeO_2$ peaks without any leftover of $Ru_2Ce$ precursor peaks.

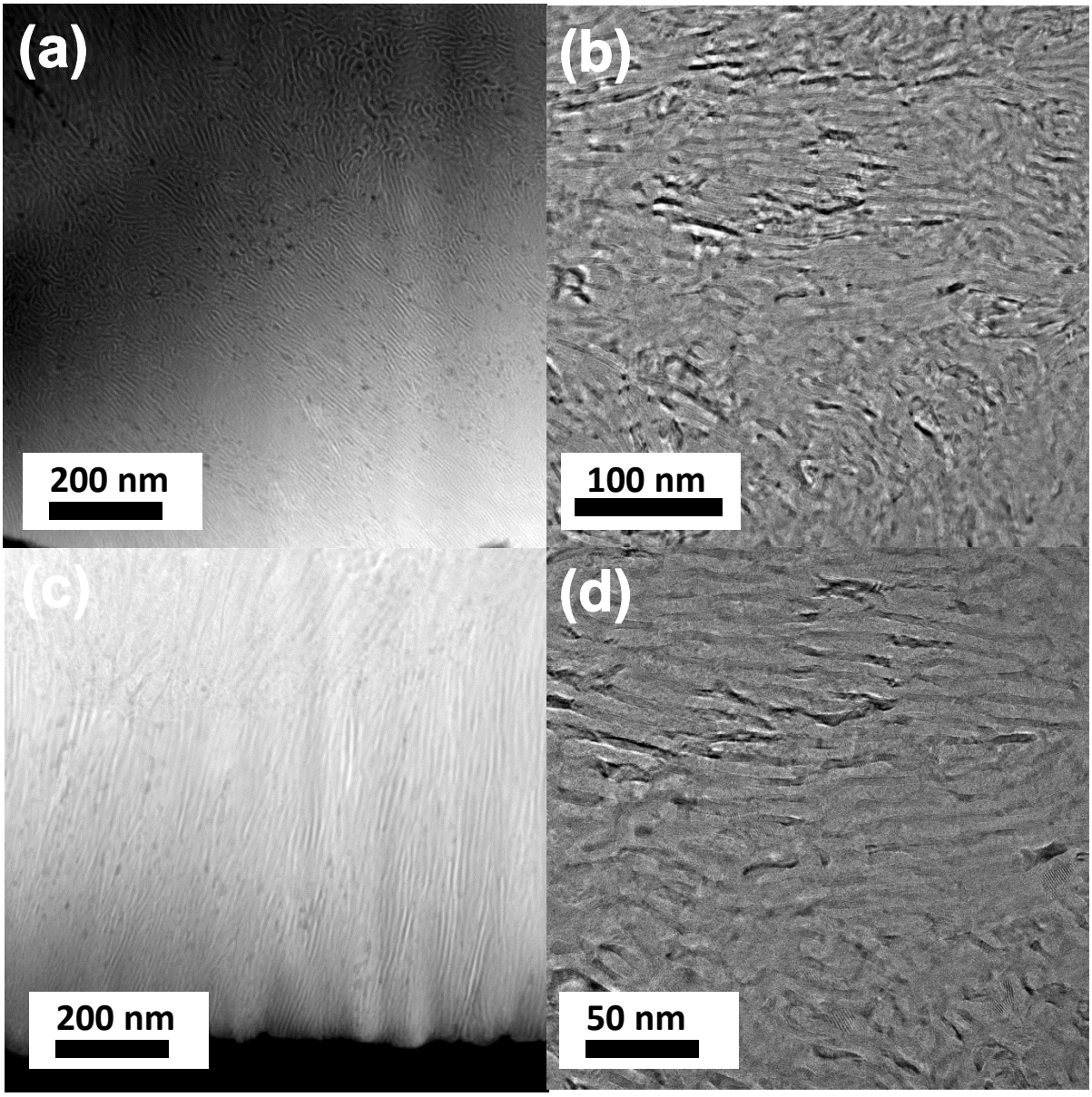


Figure 5.4: TEM image of cross-sectioned Ru-$CeO_2$ nanocomposite.

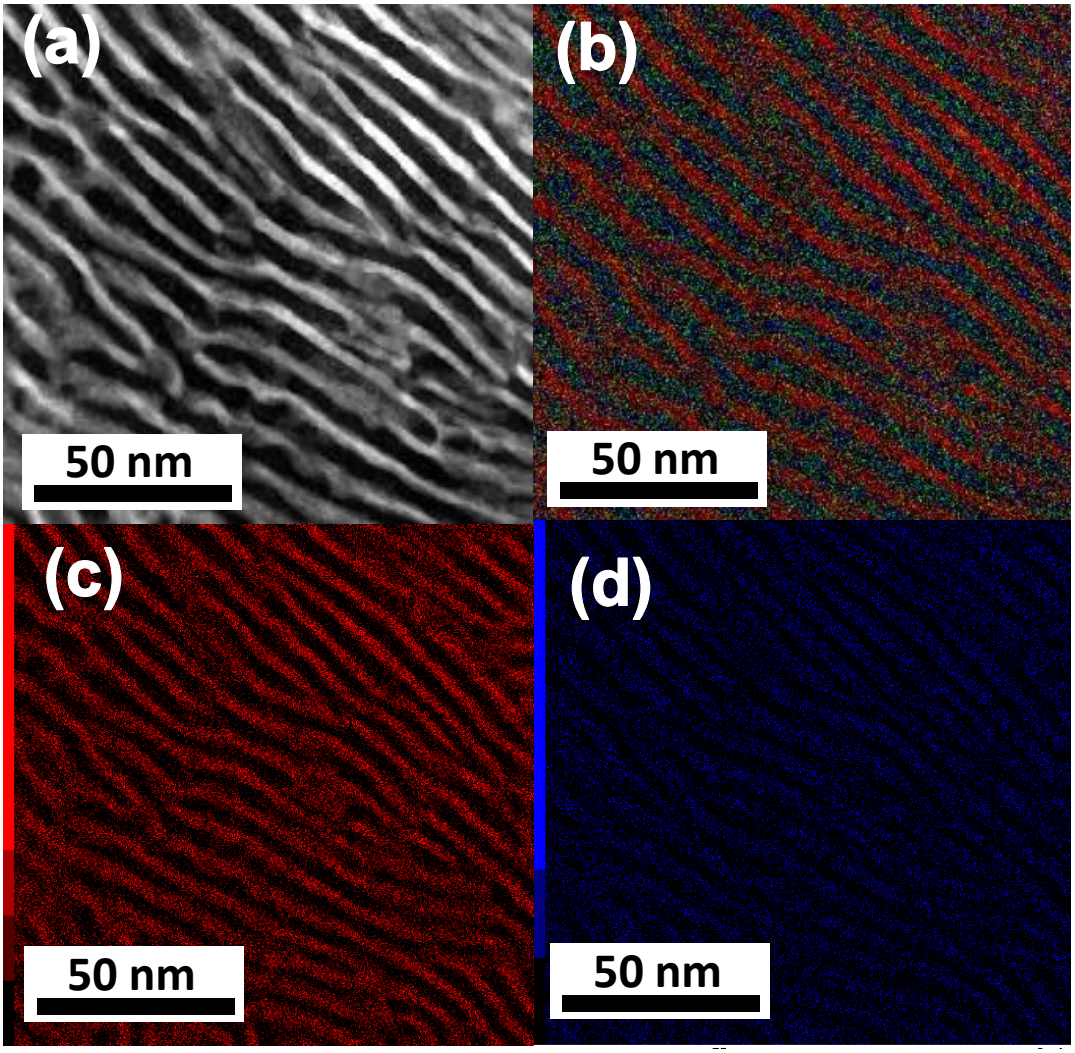


Figure 5.5 (a) STEM image, (b), (c), (d) elemental mapping of cross-sectioned Ru-$CeO_2$ nanocomposite. Pt = red, Ce = green)

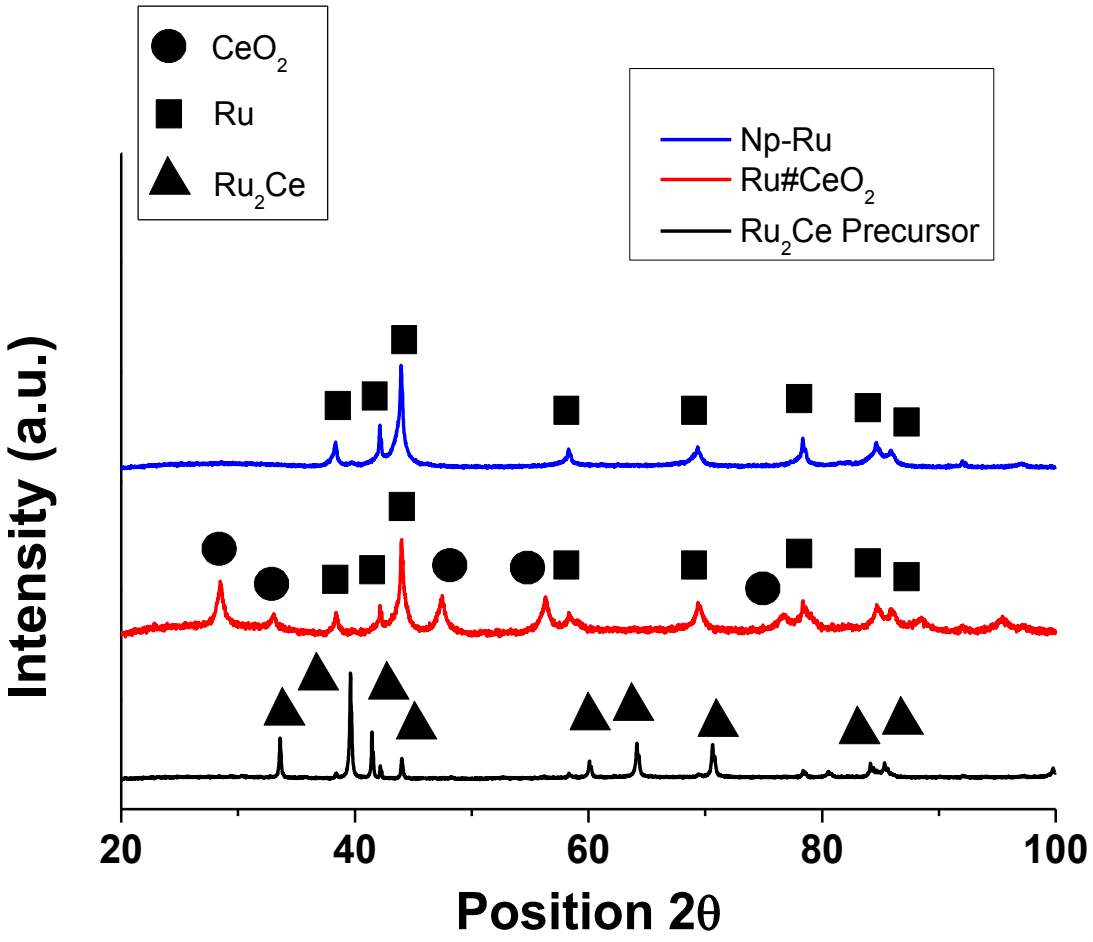


Figure 5.6: *p*XRD result of $Ru_2Ce$ and Ru-$CeO_2$ nanocomposite

Instead of using Ce as counterpart, Y was also used to understand the effect of emerging oxide phase. Precursor intermetallic compound of RuY was prepared and oxidized as per standard procedure (600ºC in $CO:O_2:Ar$ (2%:1%:97%) gas for 12 hours). STEM observation with EDS elemental mapping is presented in Figure 5.7. It reveals that though the oxide developed normal to the surface, similar to Ce based precursor, it consisted of wavy lines instead of straight lamella as in $Pt_5Ce$ and $Ru_2Ce$. One of the possible causes is the different in metal and oxide diffusions rate. As discussed in chapter 4, the ratio of diffusion rate between metal and oxide significantly affect the emerging pattern. Similar occurrence was also noticed for Rh when coupled with Y when used as precursor (RhY intermetallic compound) (Figure 5.8). Another possible reason is the structure of the oxide itself. $CeO_2$ has symmetrical distribution of Ce and O atoms regardless the facet orientation, whereas, $Y_2O_3$ has asymmetrical distribution of Y and O atoms at certain facets.

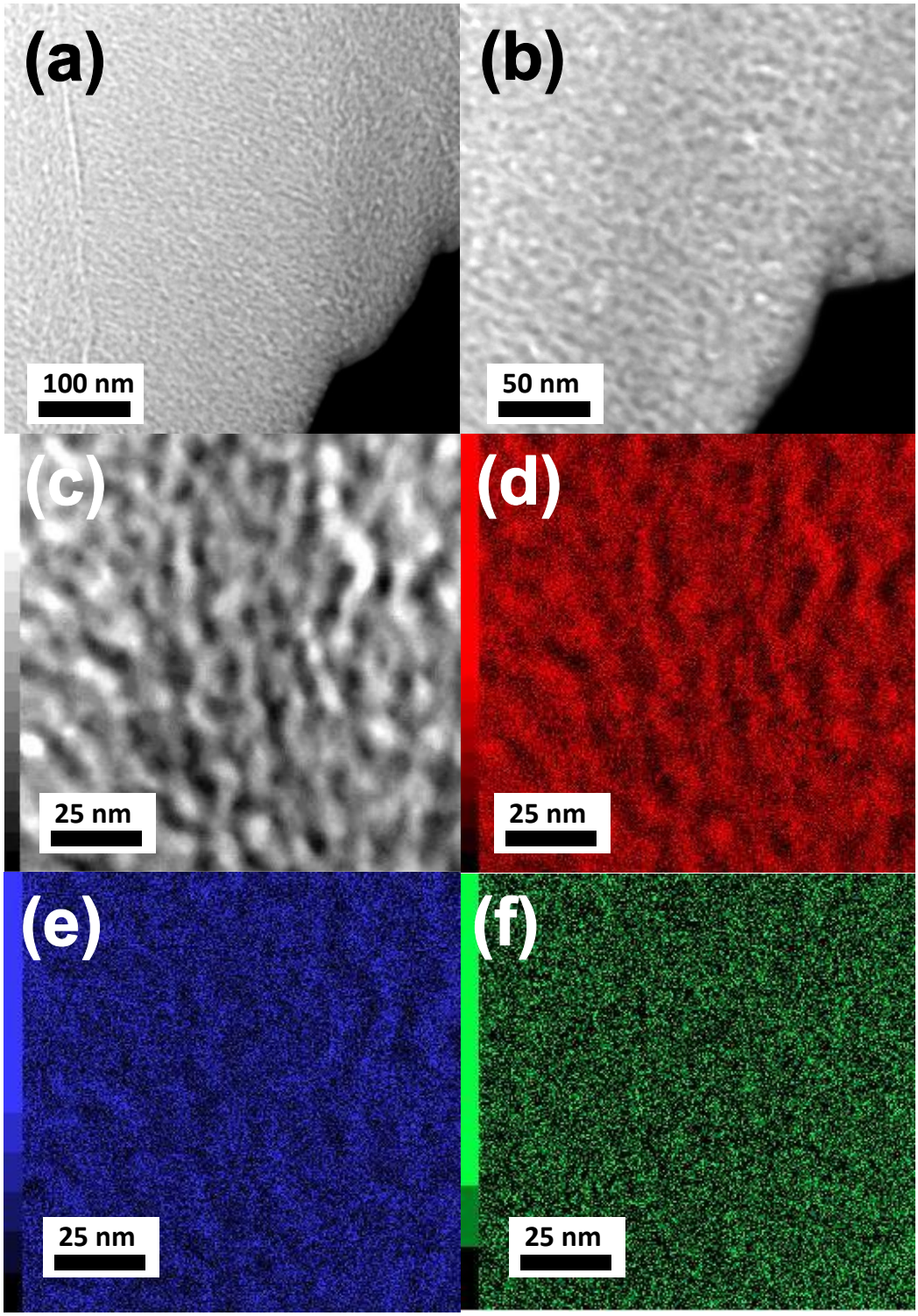


Figure 5.7 (a) (b) TEM image (c) STEM image, (d), (e), (f) elemental mapping of cross-sectioned Ru-$Y_2O_3$ nanocomposite. Ru = red, Y = blue, O = green)

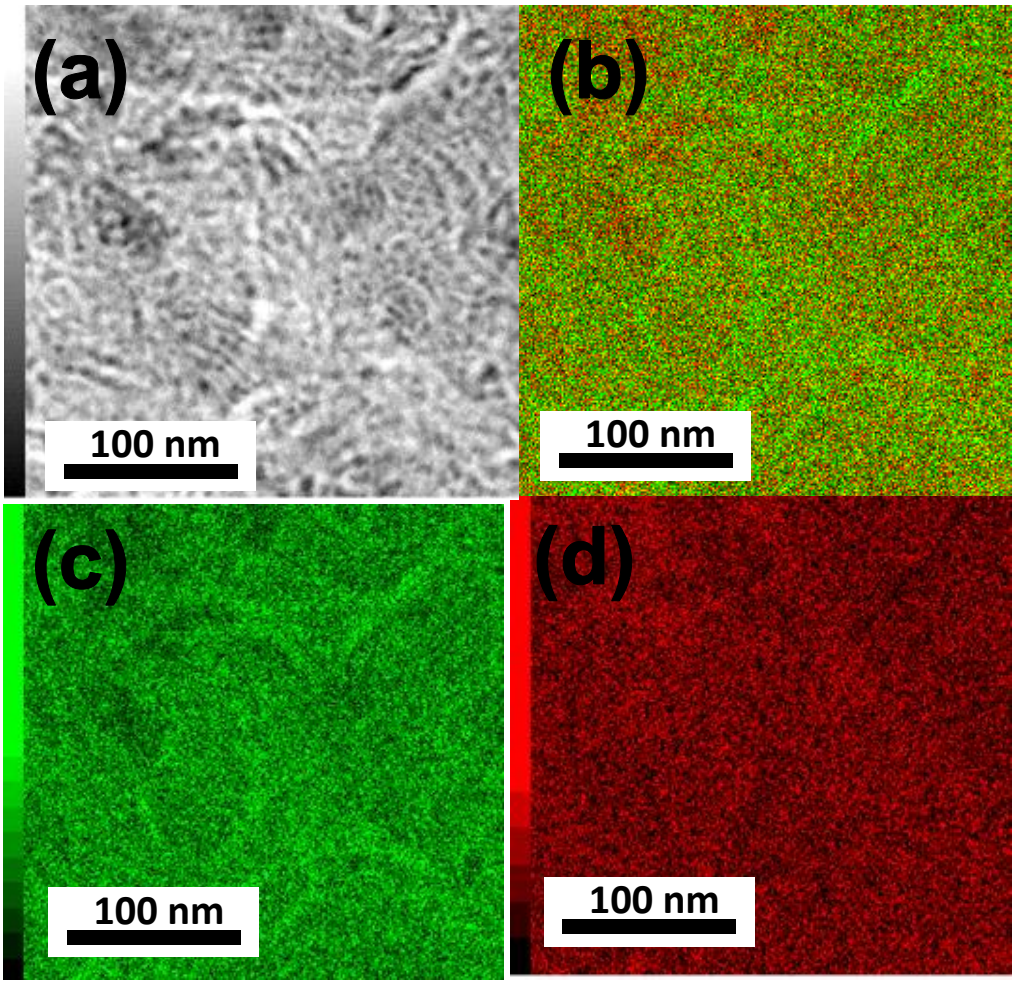


Figure 5.8 (a) STEM image, (b), (c), (d) elemental mapping of cross-sectioned Rh-$Y_2O_3$ nanocomposite. Rh = green, Y = red)

5.2 Metal-oxide epitaxial relation from nanophase separation

One of the distinct characteristics of nanophase separation is the development of metal and oxide in favor of the most stable metal-oxide interface direction. This was clearly exemplified in Ru-Ce system. The Ru phase was developed such that the Ru{$10\bar{1}0$}- and $CeO_2${110} planes were oriented in an epitaxial relation (Figure 5.9). The interatomic distance of oxygen on the $CeO_2$ (110) planes along the [100] axis, 2.7 Å, matches with the interatomic distance of Ru on the Ru ($10\bar{1}0$) planes along the [$11\bar{2}0$] axis, 2.7 Å (Figure 5.10c).[60] This lattice matching may minimize the interfacial energy between the metal- and oxide phases to favor the epitaxial Ru{$10\bar{1}0$}//$CeO_2${110} interface in the direction of Ru[$11\bar{2}0$]//$CeO_2$[100]. On the contrary, higher lattice mismatch in the direction of Ru[0001]//$CeO_2$[101] caused higher metal-oxide interfacial energy which was not favorable for further development of Ru-$CeO_2$ interface.

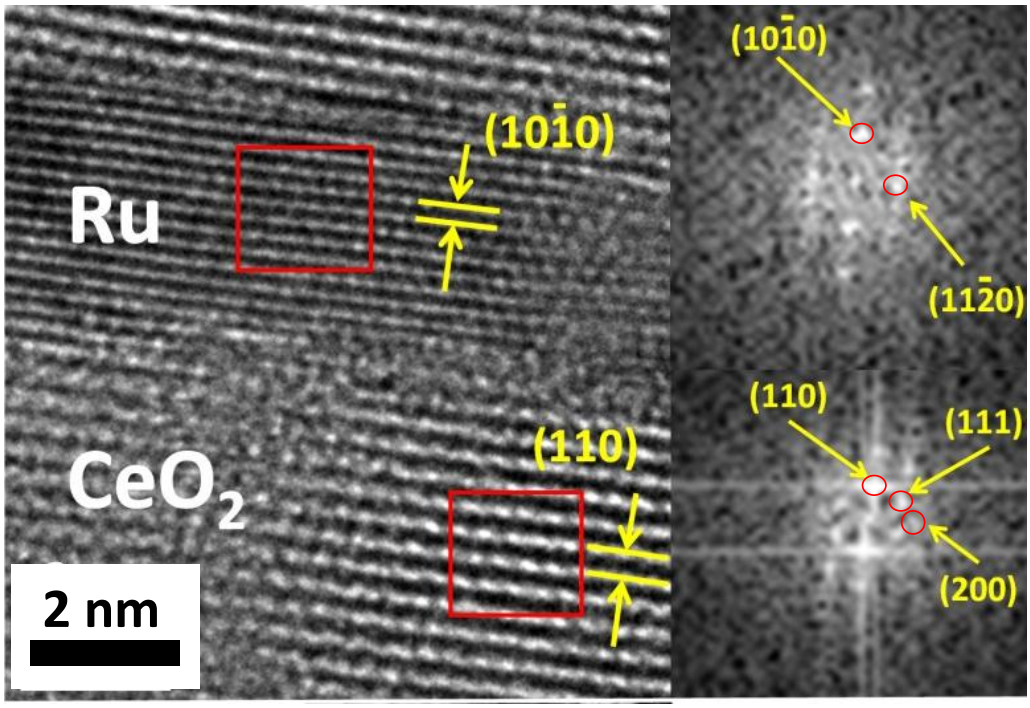


Figure 5.9: High-resolution scanning transmission electron microscopy (STEM) image at the Ru-$CeO_2$ interface.

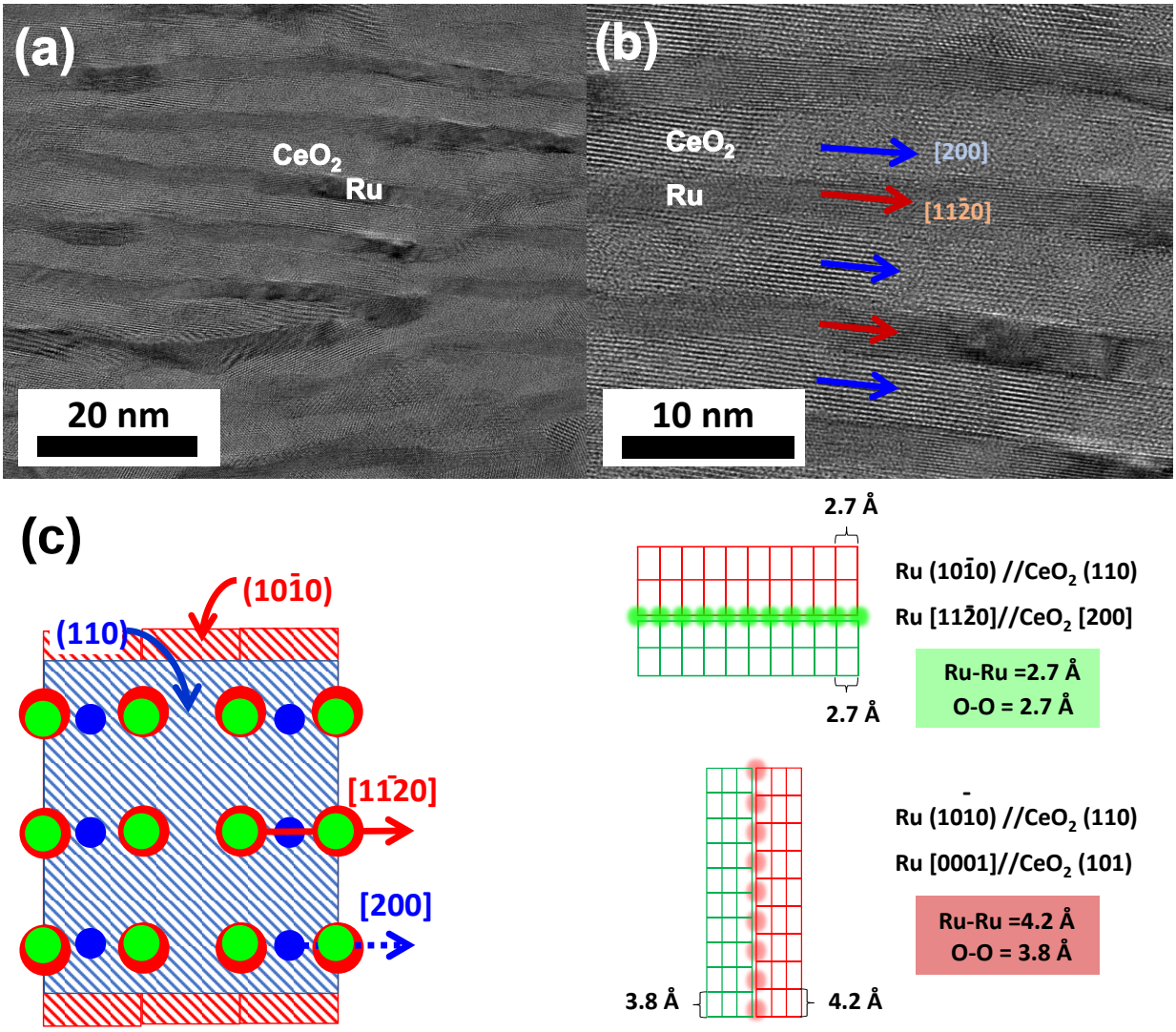


Figure 5.10: (a) TEM image of Ru-$CeO_2$ nanocomposite (b) Metal-oxide development direction (c) A schematic model for the epitaxial relation between the Ru{10-10}- and $CeO_2${110} planes. The red, blue and green circles correspond to the Ru-, Ce- and O atoms, respectively.

5.3 Characterization of nanoporous catalyst

5.3.1 Oxide promoted nanoporous Rh

Nanoporous structure was obtained through selective leaching of oxide phase. In catalysis, 2 elements are used to establish support/promoter relation and metal is commonly used as promoter. Leaching out most of the oxide and leaving a scarce amount oxide on the nanoporous metal result in a structure of inverse support/promoter.

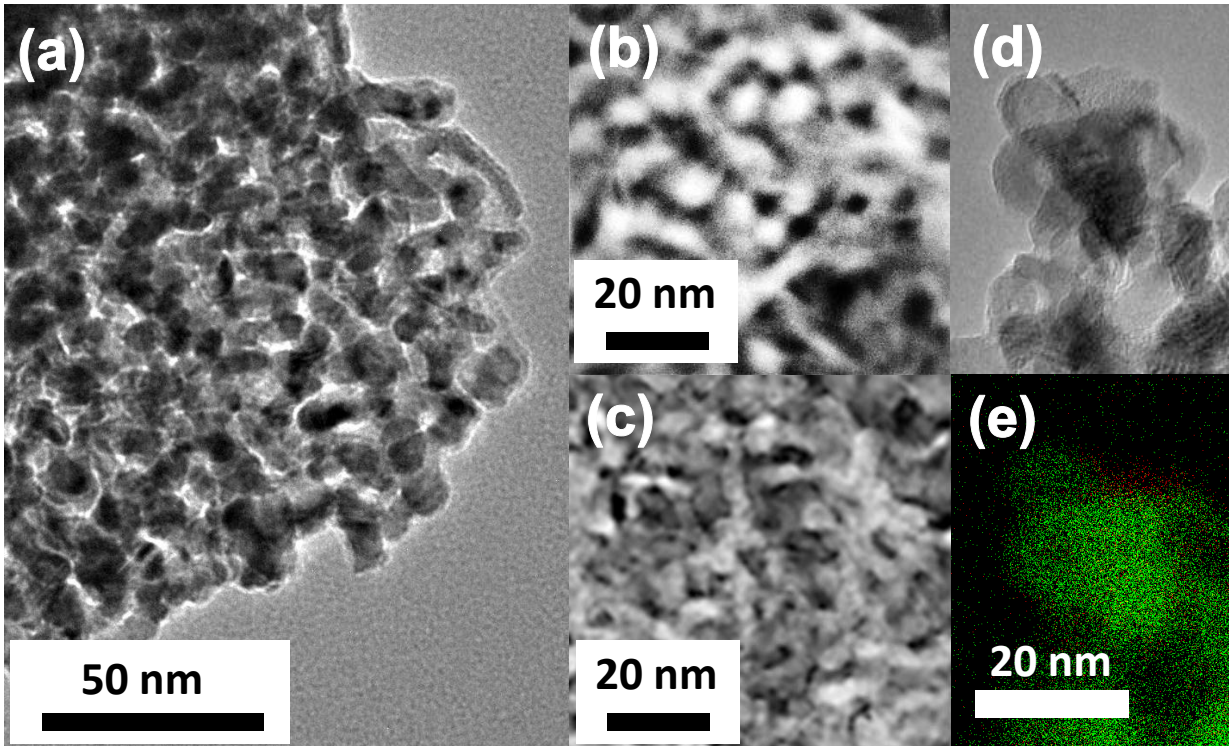


Figure 5.11: TEM/STEM images for the nanophase-separated Rh-Y composite and np-Rh. (a-b) nanophase-separated Rh-Y composite; (c-e) np-Rh. (a) STEM image for the Rh-Y composite. (b) High-magnification STEM image for the Rh-Y composite. (c) TEM image for the np-Rh. (d) a bright-field TEM image and (e) the corresponding elemental mapping. The green- and red areas again correspond to the Rh- and $Y_2O_3$ phases, respectively. The scale bars of (b)-(e) correspond to 20 nm.

Figure 5.11 shows the TEM image of Rh-Y nanocomposite after treated in $HNO_3$ (selective leaching of $Y_2O_3$) for 6 hours. The resulting nanoporous Rh consisted of an entangled, fibrous Rh that contained a number of pores in between the neighboring nano-fibres. Note that the

thickness of the fibrous Rh phase in the m-Rh (Figure 5.11c) was close to that of the Rh- and $Y_2O_3$ phases in the Rh-Y composite (Figure 5.11b). The nanoporous structure of np-Rh was, as expected, inherited from the entangled network structure of the nanophase-separated Rh-Y composite. There was a slight residue of $Y_2O_3$ partially over the surface of np-Rh (Figures 5.11d). This is also evidently supported by the *p*XRD spectra of leached samples which revealed that only after 18 hours $Y_2O_3$ was completely removed (Figure 5.12). The nitrogen ($N_2$) adsorption-desorption isotherms for porous Rh metals synthesized from various leaching time reveals that the hysteresis representing the materials porosity trend started to emerge after 6 hours of treatment (Figure 5.13a). Prolonged treatment resulted in formation of nanopores (< 5nm) as seen from BJH pore distribution in Figure 5.13b. Table 5.1 quantitatively presented the BET specific surface area of np-Rh for the corresponding leaching time.

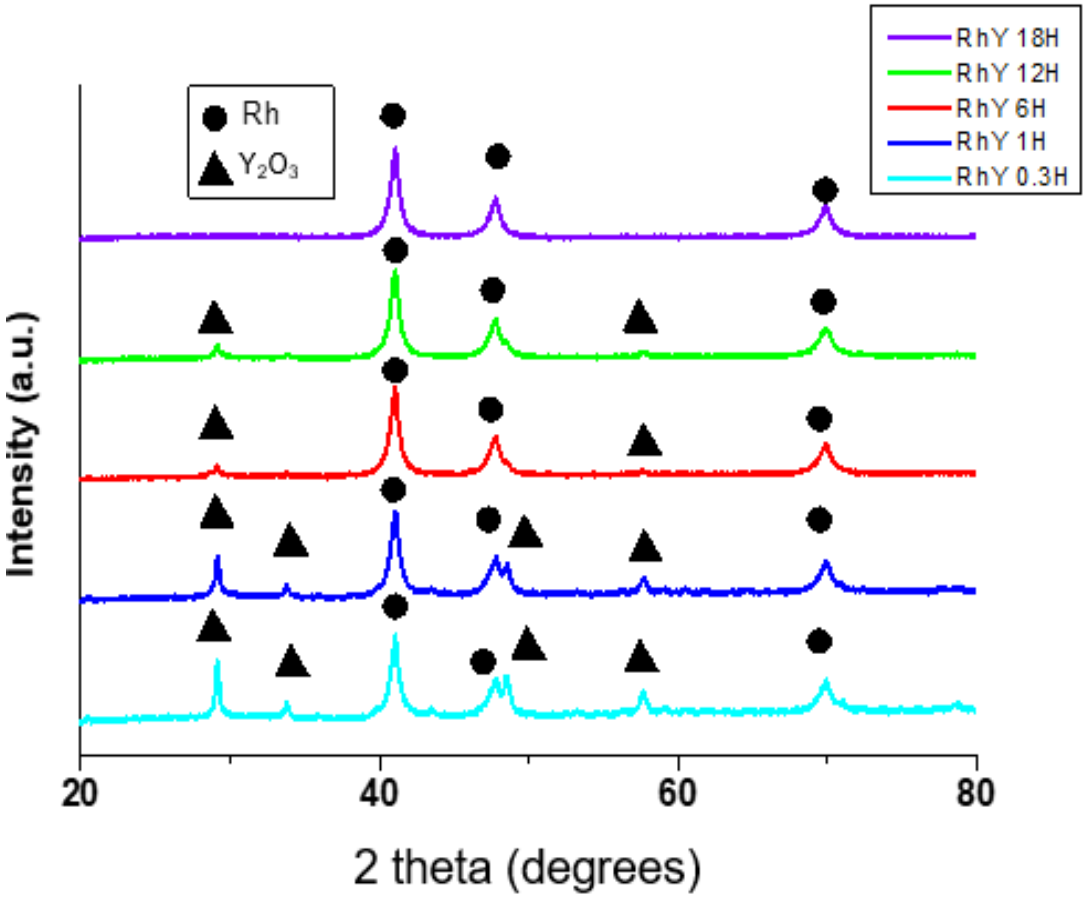


Figure 5.12: pXRD patterns of Rh-Y composite with different leaching time

Figure 5.13a shows the nitrogen ($N_2$) adsorption-desorption isotherms for different porous Rh metals, which were obtained by leaching the nanophase-separated Rh-Y composite for different periods of time (see also Figure 5.14 for the corresponding TEM images). The Rh-Y composite, leached for 0.3 and 1 h, showed a similar increasing trend on the adsorption curve with increasing relative pressure, followed by a slight hysteresis on the desorption curve. The Rh-Y composite, leached for 6 h, which corresponded to np-Rh, showed a prominent hysteresis, due to highly developed mesopores. The Rh-Y composite, leached over 12 hours, exhibited different hysteresis trends. The higher intensities of the adsorption-desorption isotherms indicate that the hierarchical porosity was further enhanced.

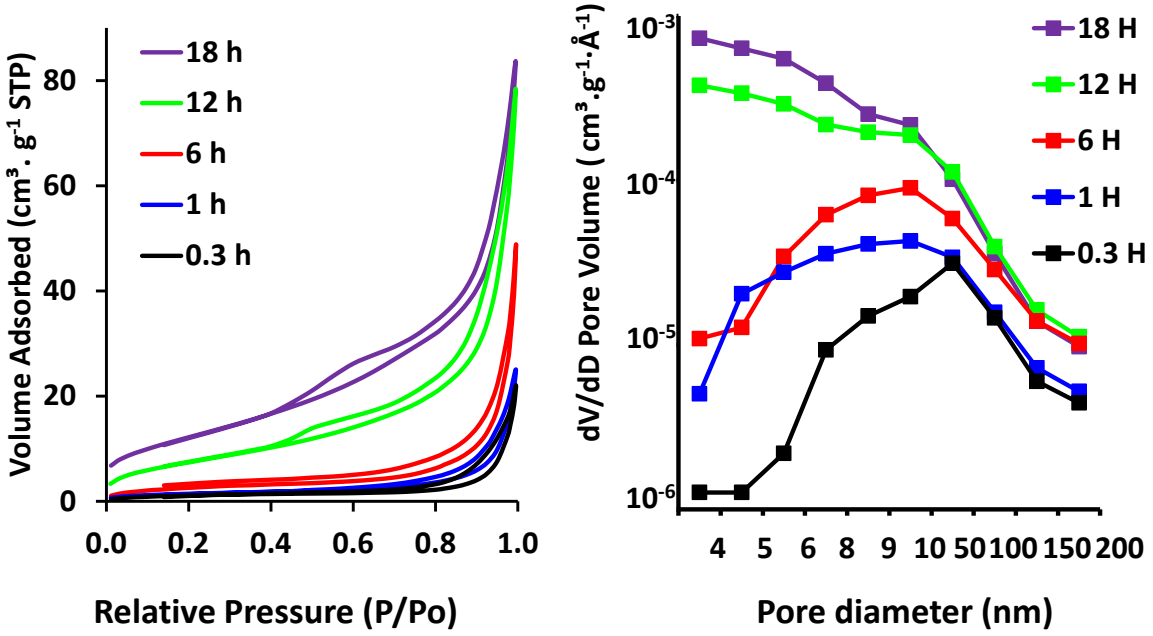


Figure 5.13: $N_2$ adsorption-desorption isotherms and pore size distribution. (a) N2 adsorption-desorption isotherms; (b) pore size distribution. The different porous Rh metals obtained from the nanophase-separated Rh-Y composite that was leached for different periods of time. The m-Rh material corresponds to the red profiles (leaching time: 6 h)

The difference in the hysteresis trend of the adsorption-desorption isotherms was also reflected on different pore distributions (Figure 3b). The dV/dD pore volumes for the Rh-Y composite, leached for less than 1 h, were lower than $10^{-4}$ $cm^3g^{-1}Å^{-1}$, due to the poorly developed porous structure. But a broad pore distribution at around 10 nm was observed. This peak became

prominent for the 6 h-leached Rh-Y composite, i.e., np-Rh. Note that the pore distribution of np-Rh was consistent with that from TEM observations, where the predominant pore size was also around 10 nm (Figure 5.11). The dV/dD pore volumes for the Rh-Y composite leached over 12 h exhibited rapidly increasing trends with decrease in the pore size, and showed a slight shoulder at around 10 nm. This shoulder became less prominent for the 18 h-leached Rh-Y composite. This phenomenon demonstrates that the deep leaching over 12 h significantly developed small nanopores (< 5 nm), being accompanied with broadening the 10 nm-sized porous structure.

Table 5.1: BET surface area of RhY nanocomposite treated at various time

| Sample | $S_{BET}$ ($m^2/g$) |
|---|---|
| RhY 0 hour acid treated | 2.68 |
| RhY 0.3 hour acid treated | 4.18 |
| RhY 1 hour acid treated | 5.15 |
| RhY 6 hours acid treated | 9.47 |
| RhY 12 hours acid treated | 28.16 |
| RhY 18 hours acid treated | 45.32 |

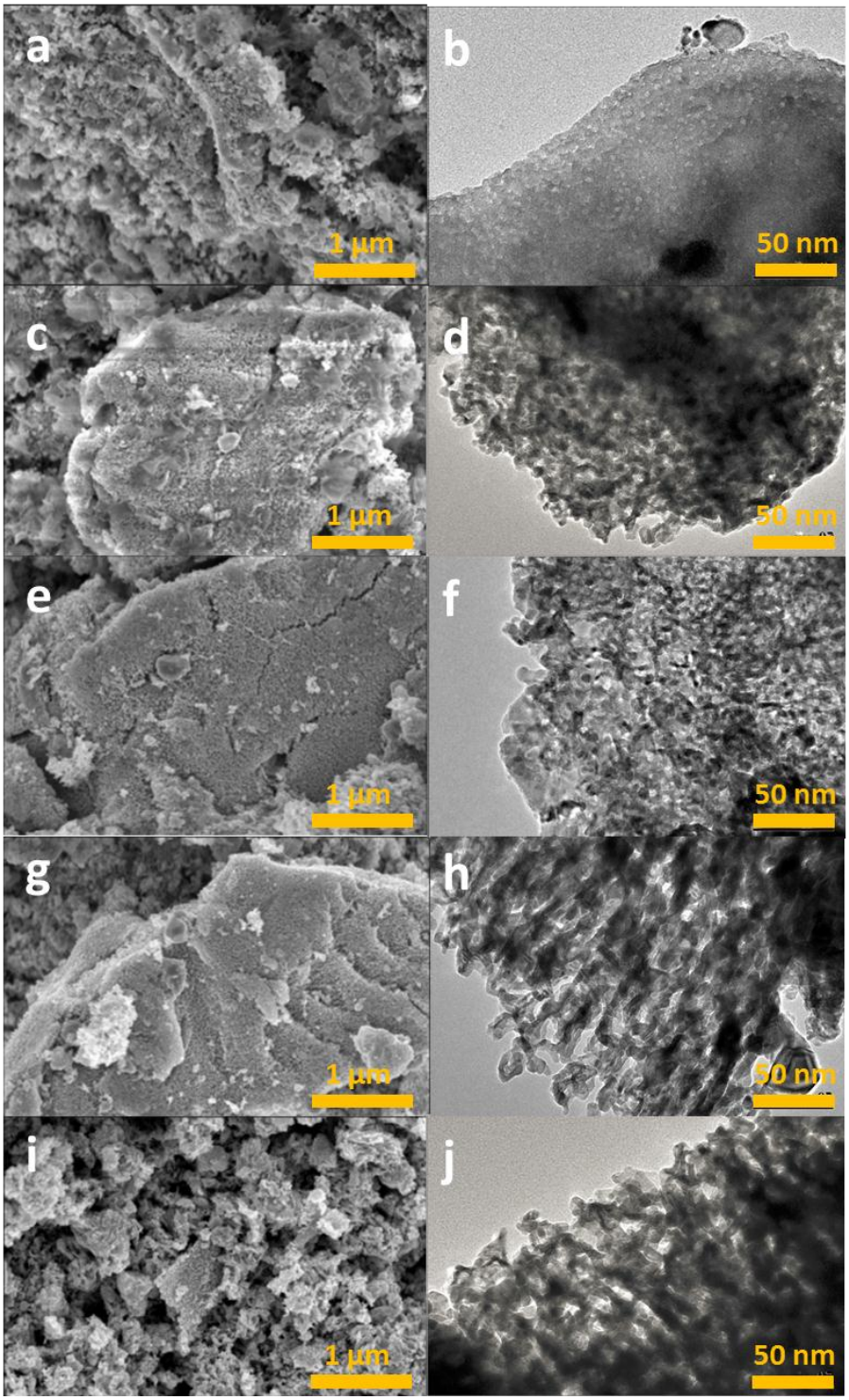


Figure 5.14: SEM and TEM images for the Rh-$Y_2O_3$ nanocomposite treated with different leaching time. SEM images: (a) 0.3 h, (c) 1h, (e) 6h, (g) 12h and (i) 18h. TEM images: (b) 0.3h, (d) 1h, (f) 6h, (h)12h and (j) 18h.

### 5.3.2 Active faceted nanoporous Ru

Catalytic activity of a catalyst is highly dependent to the exposed facet. Thus, facet tailoring has become an essential aspect in designing a new generation of catalyst. Herein, the reorientation of crystal during nanophase separation, especially at the metal-oxide interface is utilized as a mean to tailor the facet of the nanoporous catalyst. Characterization of the active faceted nanoporous catalyst is presented in this section.

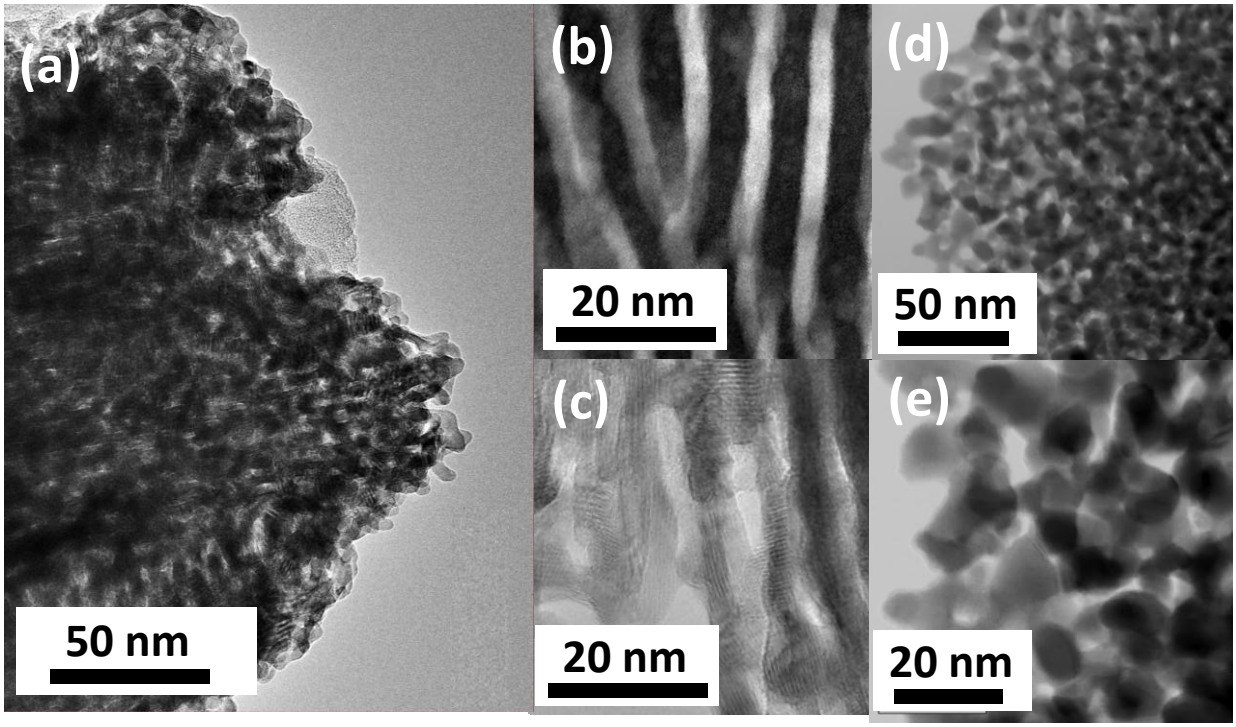


Figure 5.15: (a) TEM image of np-Ru after 6 hours leaching, (b) Sectional HAADF image of a nanophase-separated Ru-$CeO_2$ nanocomposite (dark: Ru; bright: $CeO_2$) and (c) a bright-field TEM image of active faceted np-Ru obtained via a selective leaching of Ru-$CeO_2$ nanocomposite (dark: Ru; bright: vacuum). (c) Bright-field TEM images of active faceted np-Ru. (d), (e) Np-Ru after 28h leaching.

Selective leaching of $CeO_2$ from the Ru-$CeO_2$ nanocomposite in $H_2SO_4$ solution for 6 hours resulted in the emergence of nanoporous Ru (np-Ru) (Figure 5.15a, c). Ru phase appeared to be retained structurally as in Ru-$CeO_2$ nanocomposite (Figure 5.15b). The $CeO_2$ phase was completely removed as evidenced by *p*XRD and hard X-ray photoemission spectroscopy (HAXPES) (Figure 5.16 and 5.17). On the contrary, directly dealloyed $Ru_2Ce$ manifested sign of

incomplete leaching despite being immersed in $H_2SO_4$ for 27 hours (more than 3 times longer) as $Ru_2Ce$ peaks were clearly still visible along with Ru peaks (Figure 5.16 – blue).

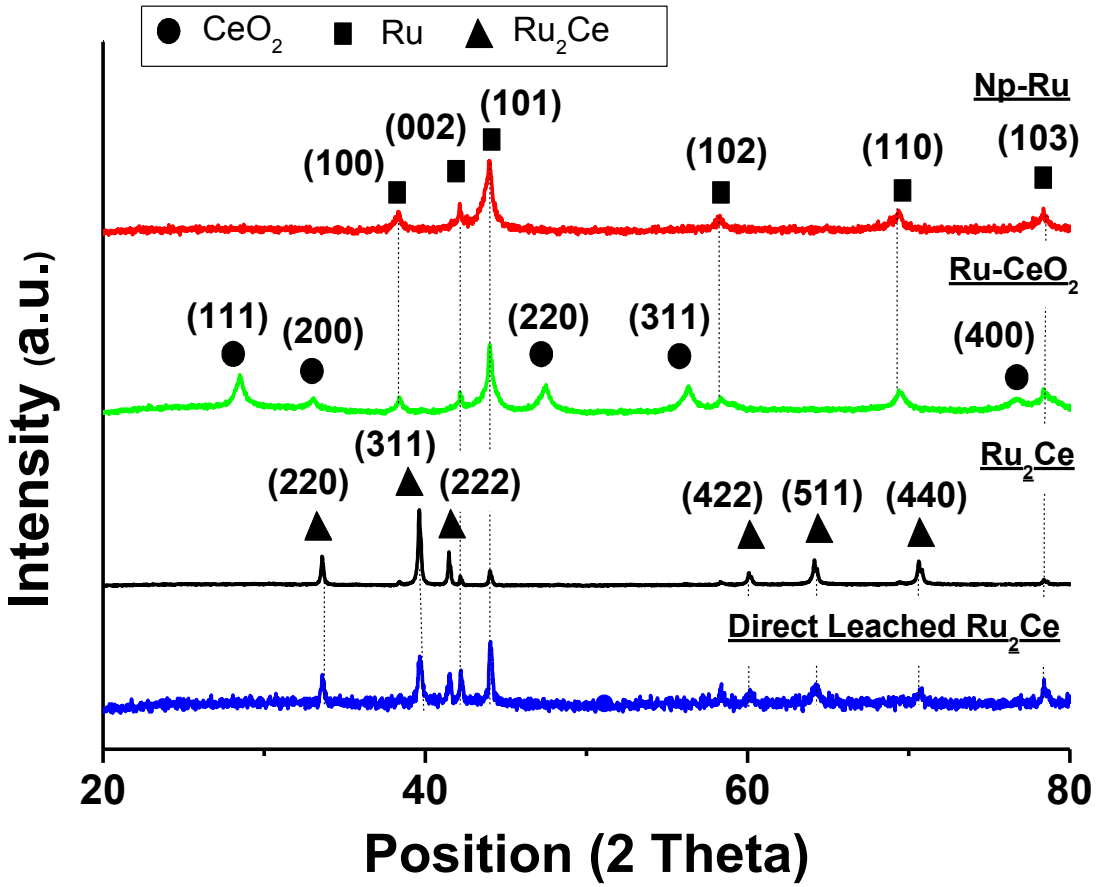


Figure 5.16: pXRD patterns of $Ru_2Ce$ precursor, Ru-$CeO_2$ nanocomposite, np-Ru, and directly leached $Ru_2Ce$

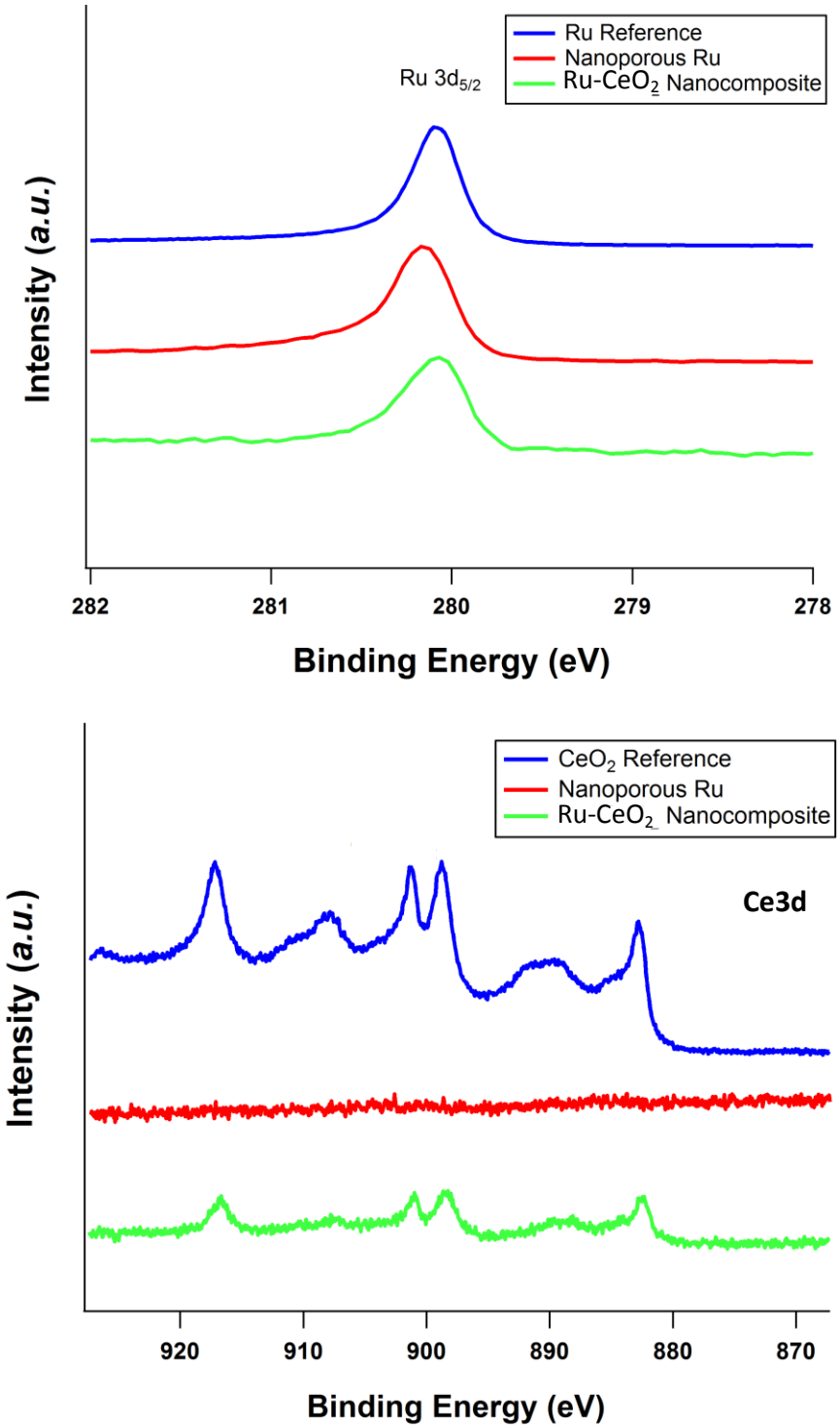


Figure 5.17: Hard X-Ray photoelectron spectra of $Ru_2Ce$ precursor, Ru-$CeO_2$ nanocomposite, and np-Ru referring to Ru3d and Ce3d orbital.

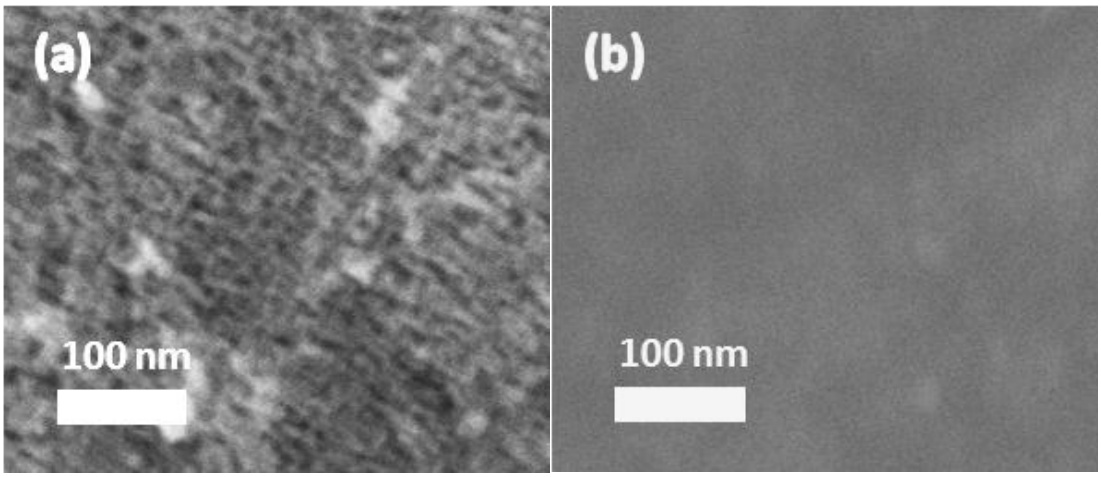


Figure 5.18: Fe-SEM image of (a) Ru-$CeO_2$ leached for 6 hours and (b) $Ru_2Ce$ directly leached for 27 hours

Specific surface area of np-Ru was quantified by BET (Brunauer-Emett-Teller) surface area measurements to be 48 $m^2g^{-1}$. Nitrogen ($N_2$) adsorption-desorption isotherm demonstrated a hysteresis trend, showing that np-Ru consisted of slit-shaped and/or lamellar pores, as per expected from the TEM observations (Figure 5.19).

Table 5.2: BET surface area of Ru nanocomposite and np-Ru

| Sample | BET Surface area |
|---|---|
| $Ru_2Ce$ | 0.3826 $m^2/g$ |
| Ru-$CeO_2$ | 1.3417 $m^2/g$ |
| Ru-$CeO_2$ 6 hours acid treated | 48.4234 $m^2/g$ |
| Ru-$CeO_2$ 27 hours acid treated | 78.3769 $m^2/g$ |

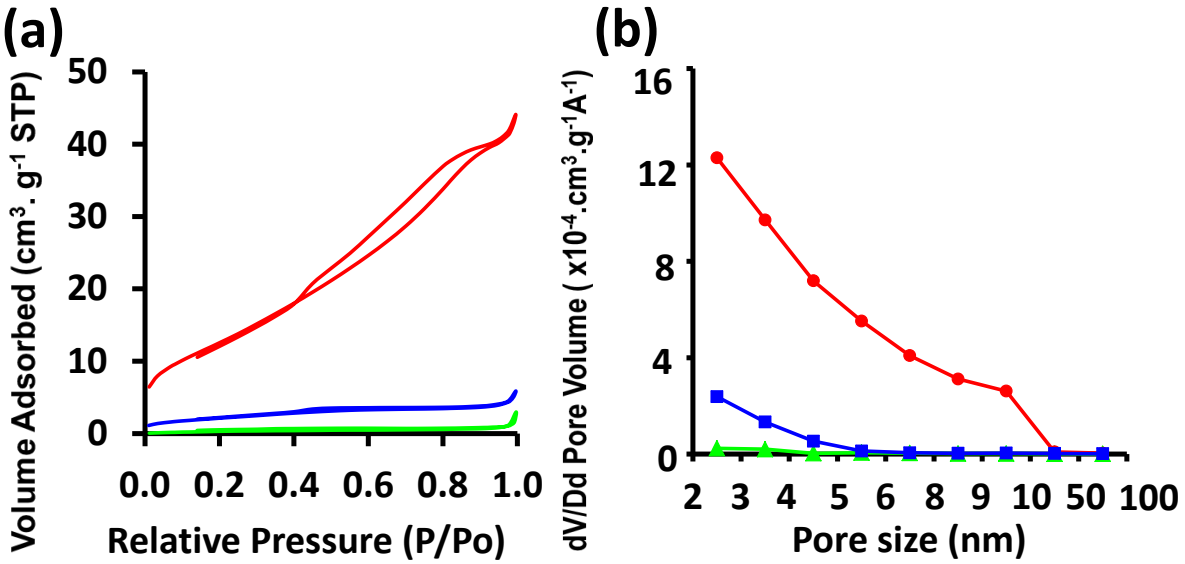


Figure 5.19: (a) $N_2$ adsorption-desorption isotherm and (b) BJH pore distribution of $Ru_2Ce$ precursor, Ru#$CeO_2$ nanocomposite, np-Ru, and directly leached $Ru_2Ce$ precursor

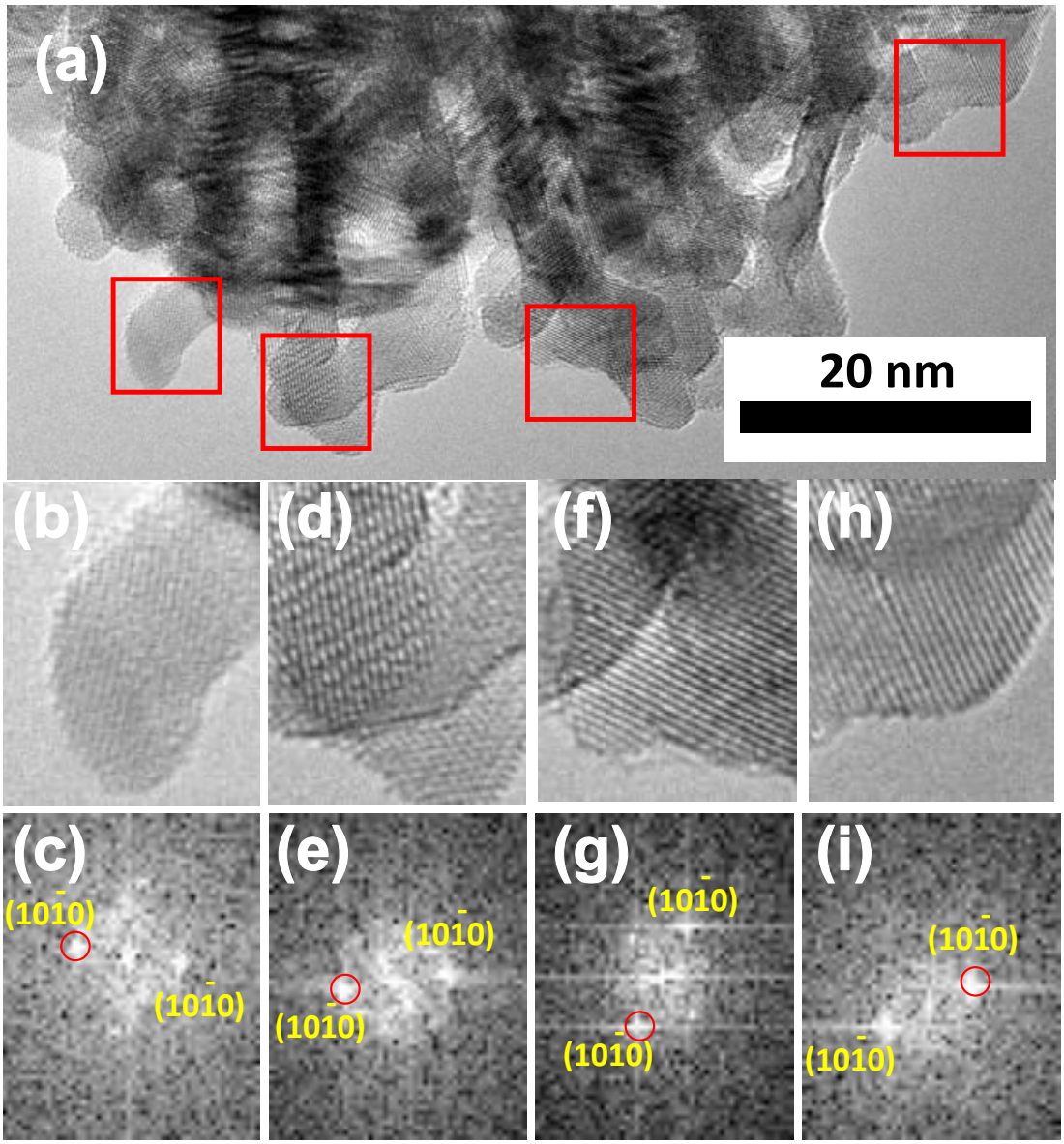


Figure 5.20: TEM image and FFT analysis of np-Ru

The Ru {10$\bar{1}$0} facets, which were extended via the formation of the Ru{1010}/Ce{110} interface in nanophase separation of the precursor alloy, became fully exposed to the environment after elimination of the $CeO_2$ matrix (Figure 5.20). It is also worth to note that in pXRD spectra, (10-10) and (11-20) peaks ((100) ⊥ (11-20)) were clearly visible in np-Ru, while very weak peaks or even almost none were noticed from directly dealloyed $Ru_2Ce$ (red shaded square). Note that Ru major peaks of (101) and even minor peaks of (002), (102), and (103) were all present in directly dealloyed $Ru_2Ce$.

## 5.4 Catalytic Performance Evaluation

### 5.4.1 Dry methane reforming (DRM)

Carbon-dioxide reforming of methane (DRM: $CO_2 + CH_4 = 2CO + 2H_2$) was conducted at a low reaction temperature of 410ºC to investigate the catalytic performance for these porous Rh materials (Table 5.3 and Figure 5.21). The obtained trend suggests that the $CH_4$ and $CO_2$ conversion increased with longer treatment time up to 6 hours. The increase is considered to be due to the removal of excess $Y_2O_3$ and formation of nanoporous structure that increased the specific surface area. The fact that specific surface area was significantly larger for 12 hours and 18 hours leached phase separated RhY and yet the conversion did not show any improvement. To shed light on this trend, electrocatalytic CO oxidation was carried out.

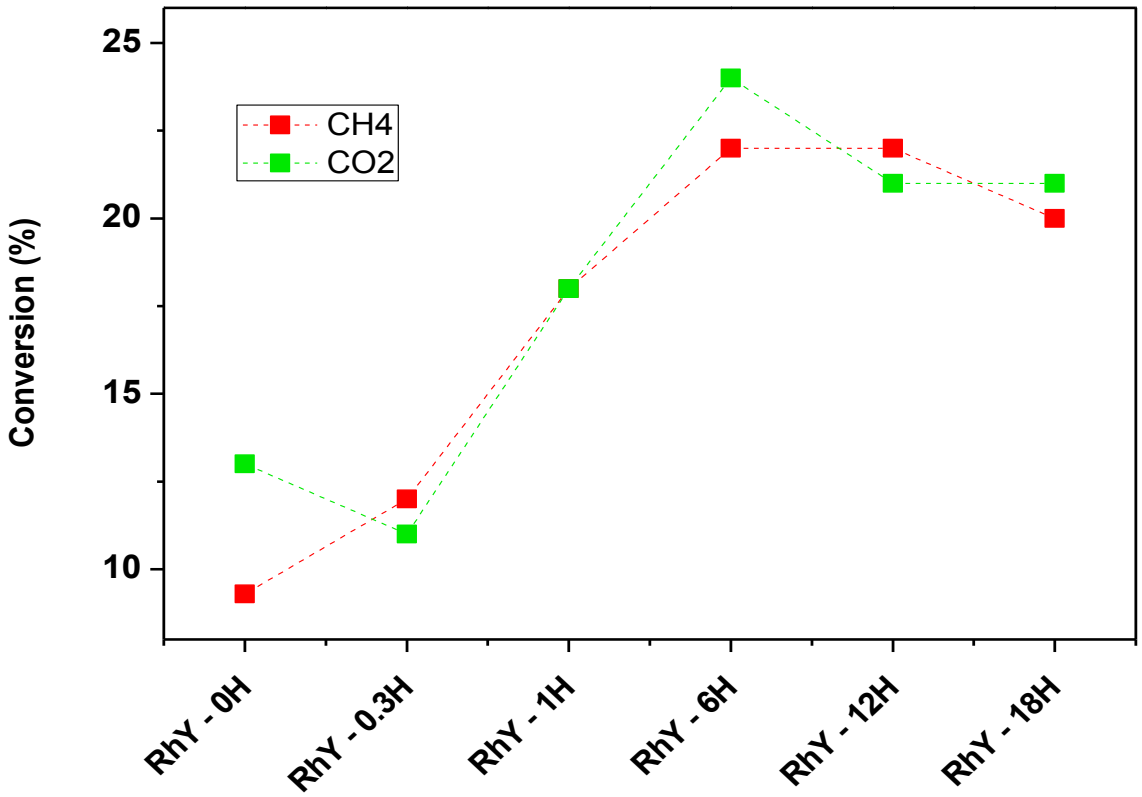


Figure 5.21: $CH_4$ and $CO_2$ conversion of nanoporous Rh during DRM reaction at 410ºC

Table 5.3: $CH_4$ and $CO_2$ conversion, and H2/CO ratio of nanoporous Rh - DRM reaction at 410ºC using $CH_4/CO_2/Ar$ (1/1/98 in vol %) gas as input

| Sample | $CH_4$ Conv. [%] | $CO_2$ Conv. [%] | $H_2$/CO ratio |
|---|---|---|---|
| RhY-0H | 9.3 | 13 | 0.8 |
| RhY-0.3H | 12 | 11 | 0.8 |
| RhY-1H | 18 | 18 | 1.0 |
| RhY-6H | 22 | 24 | 1.1 |
| RhY-12H | 22 | 21 | 1.1 |
| RhY-18H | 20 | 21 | 1.2 |

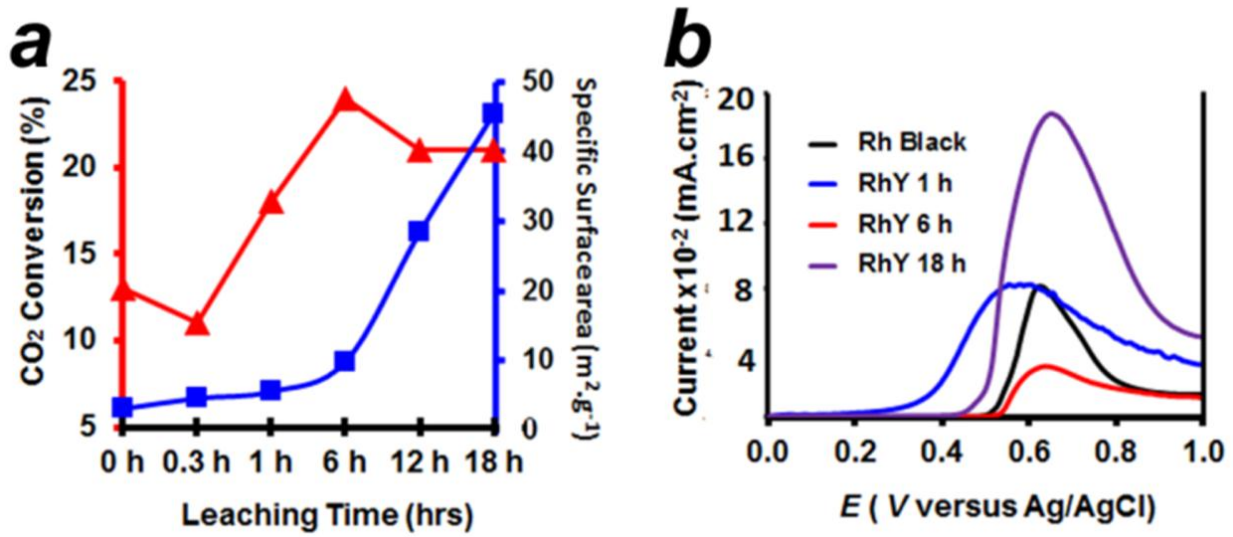


Figure 5.22: DRM performance and CO electro-oxidation. (a) DRM performance. Reaction conditions: Catalyst weight = 0.1g; temperature = 683 K; CH4/CO2/Ar = 1/1/98; flow rate = 100 mL min-1. The CO2 conversion rate and BET surface area for the different porous Rh metals presented as functions of leaching time. (b) CO electro-oxidation. Current vs. potential profiles for the CO electro-oxidation over the porous Rh materials leached for different periods of time.

To further elucidate the surface nature of the np-Rh, electrocatalytic CO oxidation was conducted in aqueous media. The results are shown in Figure 5.22b. The np-Rh material exhibited an onset potential of +0.52 V toward the CO electro-oxidation, which was as high as the onset potential for polycrystalline Rh nanoparticles. The porous Rh material, obtained by 1 h-leaching of the nanophase-separated Rh-Y, showed an onset potential of +0.30 V, lower than the np-Rh or Rh nanoparticles. This indicates that the 1 h-leaching Rh-Y composite possesses a strong ability for CO oxidation ($CO + H_2O = CO_2 + 2H^+ + 2e^-$). Oppositely, the np-Rh revealed a weak CO oxidation, suggesting that it can inhibit the combination of CO and oxygen-containing species. To our knowledge, one of the rate-determining steps for DRM is the dissociation of $CO_2$ admolecules into CO and oxygen adatoms ($CO_2 = CO + O_{ads}$), which can form a large number of CO and oxygen species. Therefore, the inhibition of np-Rh is in favor of the stable CO and oxygen species.

Rare-earth oxides including $Y_2O_3$ are commonly used as promoters for oxidative catalysis such as the CO oxidation, due to the inherently high ability as an oxygen ionic conductor.[61–63] The promoted CO oxidation over the 1 h-leached Rh-Y composite may be attributed to the residual $Y_2O_3$ over the pore surface (Figures 5.12). In addition, the 18 h-leached Rh-Y composite also exhibited a promotion for the CO oxidation. Our characterizations have also revealed that it possessed highly porous structure, but no residual $Y_2O_3$ (Figures 5.12). This allows us to consider that the hierarchical pore structure is another reason to enhance the reaction of CO and oxygen-containing species, and inhibited the CO formation from $CO_2$ in the DRM. However, the np-Rh possesses a unique nanoporous structure and moderate BET surface area. As the result, it developed a high DRM performance (Figure 5.22a).

### 5.4.2 Hydrogen evolution reaction (HER)

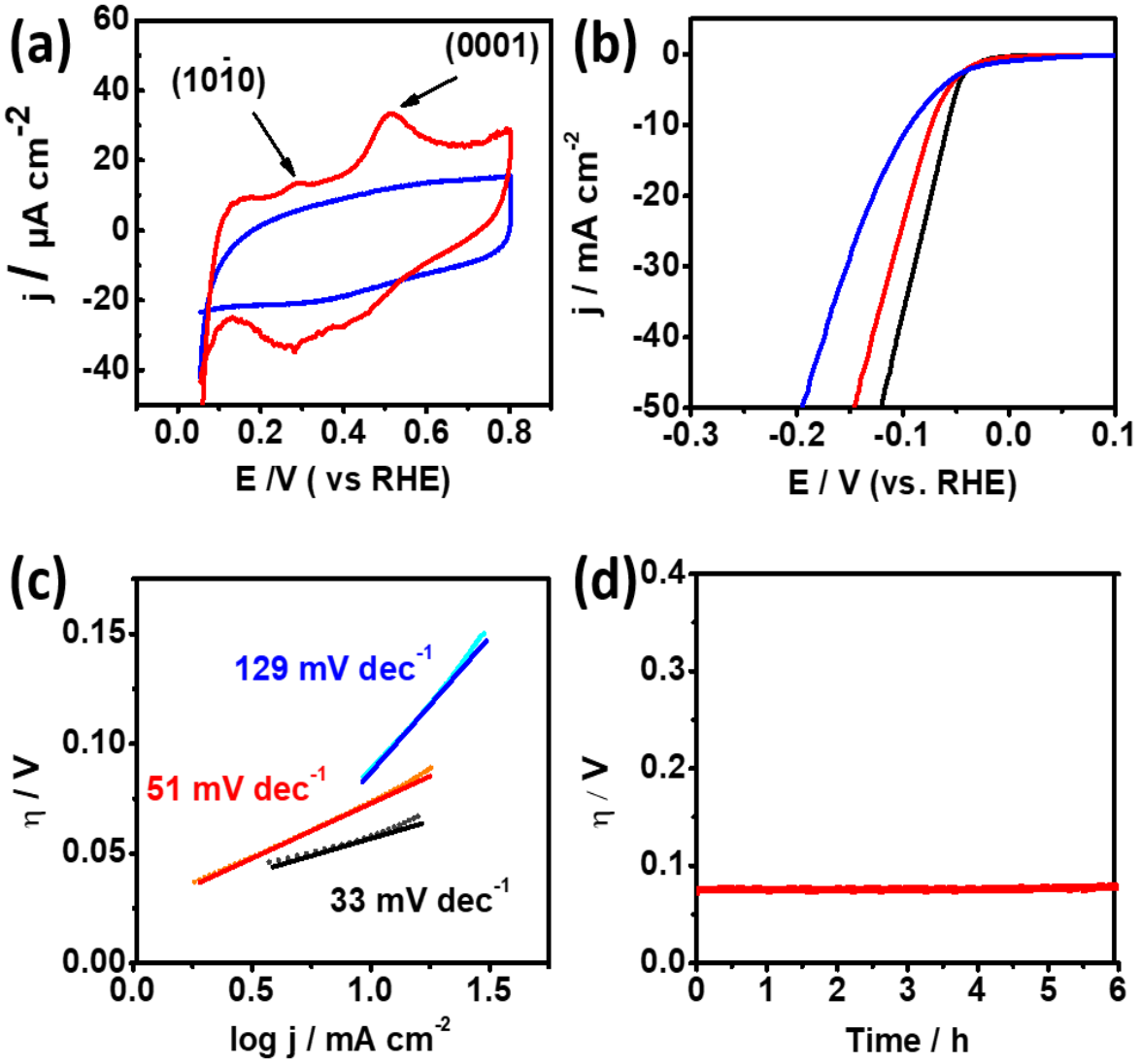


Figure 5.23: (a) Cyclic voltammetry (CV) profiles for np-Ru (red) and Ru/C (blue), (b) Linear-sweep voltammetry (LSV) profiles and the corresponding (c) Tafel plots for np-Ru (red), Ru/C (blue) and Pt black (black). The corresponding Tafel slopes are shown as inset. (d) Chronogalvanometry profile for np-Ru (red) acquired at a HER current density of 10 $mVs^{-1}$. All the experiments were conducted in 0.5 M $H_2SO_4$ solution.

Cyclic voltammetry (CV) was conducted in 0.5 M $H_2SO_4$ solution using a rotating glassy-carbon disk electrode to identify the preferential facets of np-Ru. Figure 5.23a presents the CV profiles for np-Ru and carbon-supported Ru (Ru/C; loading weight: 5%). Ru/C showed a typical CV profile for polycrystalline Ru with no preferential facets. By contrast, np-Ru showed a CV profile having distinct peaks at +0.30 V and +0.52 V vs. RHE, corresponding to the electrochemical oxidation of chemisorbed hydrogen atoms over the $\{10\bar{1}0\}$- and {0001} facets, respectively.[64] As expected from the TEM characterizations (Figure 5.20), np-Ru was predominantly surrounded by the $\{10\bar{1}0\}$- and {0001} facets.

Linear sweep voltammetry (LSV) was performed in 0.5 M $H_2SO_4$ in a potential range from +100 mV to -400 mV vs. RHE to evaluate the HER performance of the faceted np-Ru catalyst (by considering overpotential at current density, *j* of 10 $mAcm^{-2}$).[59,65,66] As comparison, Ru/C and Pt black were also tested in the same condition. The polarization curves resulting from LSV demonstrated that np-Ru had overpotential of +74 mV. This value was significantly low compared to the overpotential of +94 mV for Ru/C, and rather close to that for the state-of-art Pt/C, +58 mV (Figure 5.23b). We performed LSV using a graphite rod as the counter electrode to avoid possible contamination by redeposition of Pt (Figure 5.24a).[67] Another control LSV was conducted in perchloric acid ($HClO_4$) electrolyte to avoid possible another possible contamination by sulfuric anion ($SO_4^{2-}$) adsorption (Figure 5.24b). The np-Ru catalyst was superior to Ru/C in both of the conditions in terms of the higher onset potential. We further compared the HER performance of np-Ru to that of pure metal Ru, which substantiated the priority of np-Ru to metal Ru materials that are not tailored in nanopores or facets (Figure 5.24c). The electrochemical surface areas (ECSA) for np-Ru and Ru/C were finally determined as 39.60 and 73.87 m2g-1, respectively, by measuring the double-layer capacitances in the electrolyte solution (Figure 5.25.[54–57,68] The current density normalized to the ECSA also substantiated that np-Ru was superior to Ru/C in HER activity (Figure 5.24d).

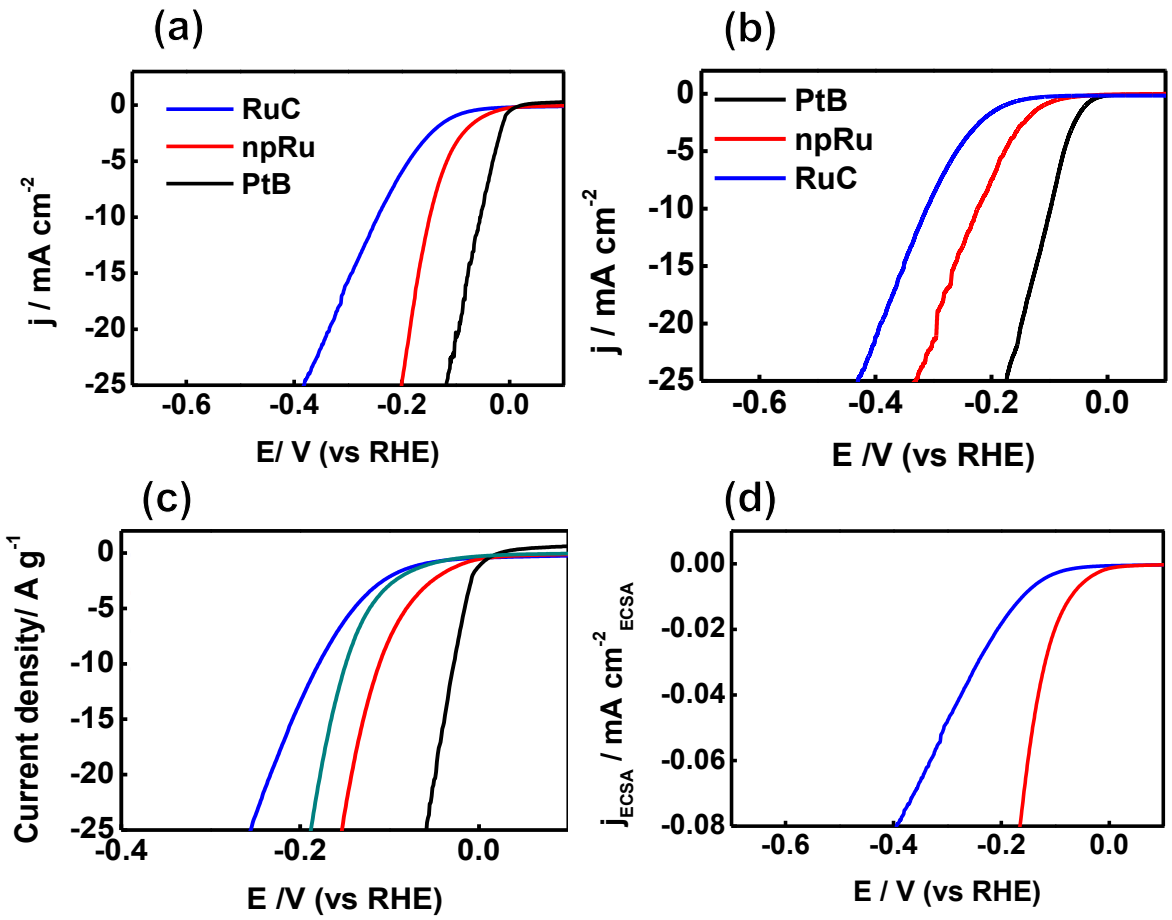


Figure 5.24: (a) Linear-sweep voltammetry (LSV) profiles for np-Ru (red), Ru/C (blue) and Pt black (black) using graphite rod as counter electrode. (b) Linear-sweep voltammetry (LSV) profiles for np-Ru (red), Ru/C (blue) and Pt black (black) using graphite rod as counter electrode ($HClO_4$ (0.1 M) as electrolyte). (c) Linear-sweep voltammetry (LSV) profiles normalized with mass loading for np-Ru (red), Ru/C (blue), Ru (green) and Pt black (black) using graphite rod as counter electrode ($H_2SO_4$ (0.5 M) as electrolyte). (d) Linear-sweep voltammetry (LSV) profiles for np-Ru (red) and Ru/C (blue) that are normalized to the ECSA.

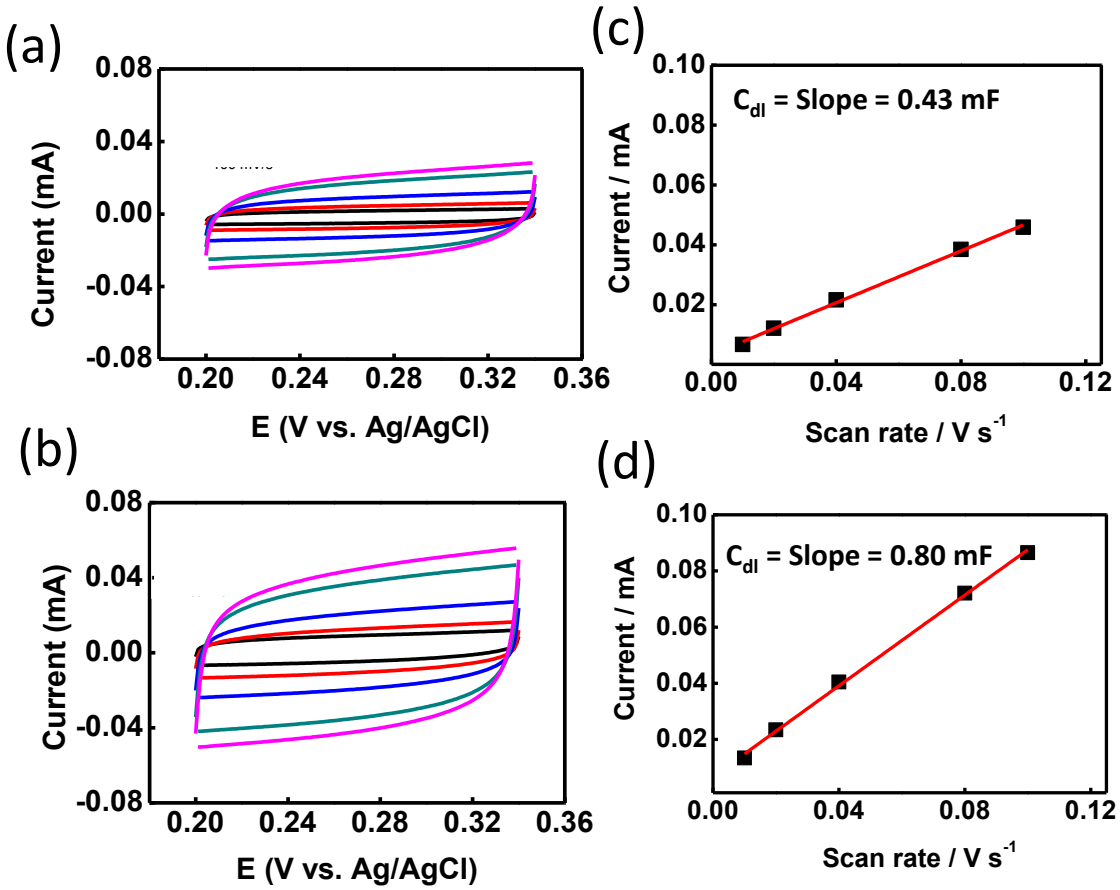


Figure 5.25: Static CV at multiple scan rates for (a) np-Ru and (b) Ru/C, and double-layer charging current vs scan rate for (c) np-Ru and (d) Ru/C. Scan rates are represented in black (10 V/s), red (20 V/s), blue (40 V/s), green (80 V/s), and purple (100 V/s).

Furthermore, the Tafel slope (*A*) for np-Ru, +51 mV $dec^{-1}$, was much lower than that for Ru/C, +129 mV $dec^{-1}$, and again closer to that for Pt black, +33 mV $dec^{-1}$. The np-Ru catalyst promoted HER not only at lower overpotential but also kinetically fast compared to Ru/C (Figure 5.23c). In addition, the estimated exchange current density at zero overpotential ($J_0$) from the Tafel extrapolation method for np-Ru, PtB, and Ru/C are 22.67 $mAcm^{-2}$, 17.25 $mAcm^{-2}$, and 6.638 $mAcm^{-2}$, respectively (Figure 5.26). The np-Ru catalyst exhibited a higher exchange current density than Ru/C, indicating that the np-Ru surface has a so low energy barrier that charge is readily transported between the electrolyte and the catalyst surface.

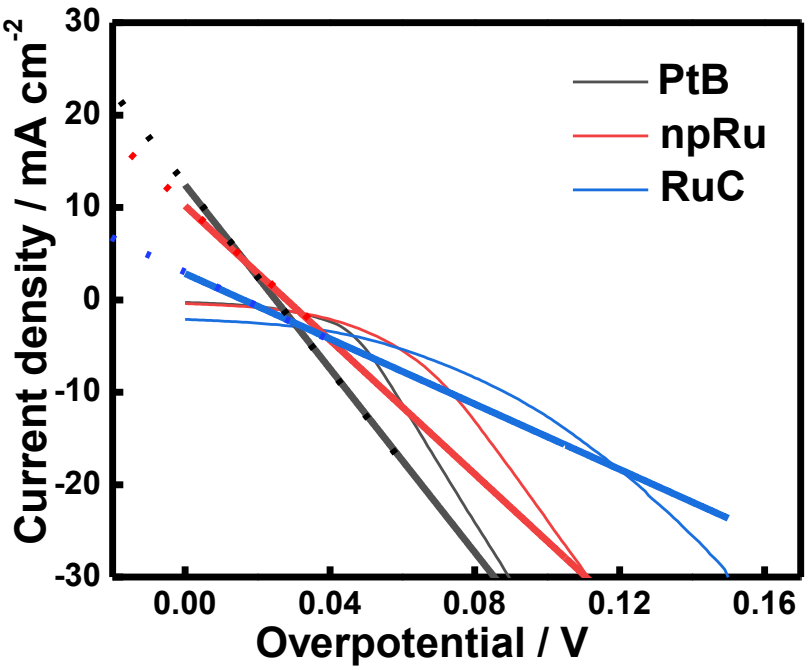


Figure 5.26: Determination of exchange current density ($j_0$) by Tafel extrapolation method.

It is acknowledged that there are three rate-determining steps associated with HER in acidic media, resulting in different Tafel slopes: reduction of hydronium ions, $H_3O^+$ to H adatoms, $H_{ads}$ (Volmer reaction: $H_3O^+ + e^- + M \rightarrow H_{ads} + H_2O$; *A*=120 mV $dec^{-1}$), electrochemical desorption (Heyrovsky reaction: $H_{ads} + H_3O^+ + e^- \rightarrow H_2 + H_2O + M$; *A*=40 mV $dec^{-1}$) and pairing of the $H_{ads}$ to form molecular $H_2$ (Tafel reaction: $2H_{ads} \rightarrow H_2 + 2M$; *A*=30 mV $dec^{-1}$) where *M* corresponds to the surface empty site.[69,70]

Based on the calculated Tafel slopes, the rate-determining step for Ru/C is assigned to the Volmer reaction in which $H_3O^+$ reduction to $H_{ads}$ was relatively slow. By contrast, the np-Ru catalyst promotes HER predominantly via the Volmer-Heyrovsky reaction, where $H_{ads}$ was readily available to be desorbed via electrochemical pathways. As theoretically demonstrated by Li *et al.*, the Ru $\{10\bar{1}0\}$- and $\{0001\}$ facets moderately adsorb $H_{ads}$ compared to the other facets including $\{11\bar{2}0\}$.[71] The moderately adsorbed $H_{ads}$ on to the $\{10\bar{1}0\}$ facets can serve as an active intermediate for the other reactions, *i.e.*, hydronium ions to molecular $H_2$ (Heyrovsky) as for np-Ru, whereas too strongly adsorbed $H_{ads}$ depletes the surface empty site, *M*, slowing down further generation of active $H_{ads}$ (Volmer) as observed in Ru/C.[72]

The electrochemical impedance spectra exhibited a small arc diameter for np-Ru compared to that for Ru/C, showing a lower resistance for np-Ru at the electrode/electrolyte interface (Figure 5.27). The improved HER catalytic activity of np-Ru is partly attributed to the lowered charge-transfer resistance at the catalyst/electrode interface. The low electrode/electrolyte resistance is associated to better diffusion of hydrogen, electrolyte, and intermediate species.[68]

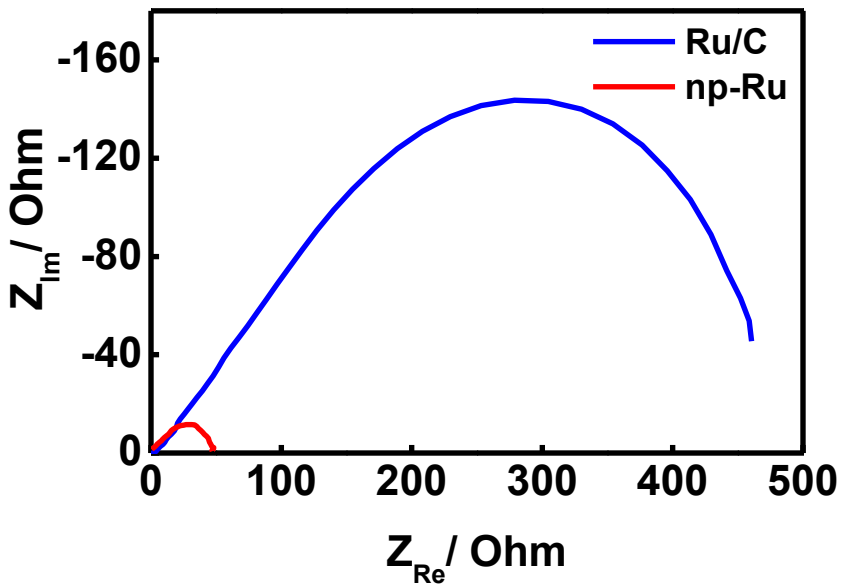


Figure 5.27: Electrochemical impedance spectra (EIS; Nyquist plot) at a potential of -0.4 V over the frequency range of 0.01 Hz–100 kHz in 0.5 m $H_2SO_4$ solution (graphite as counter electrode) for np-Ru (red), Ru/C (blue) and Pt black (black).

The catalyst stability of np-Ru was evaluated by chronogalvanometry (Figure 5.23d) and chronoamperometric (Figure 5.28) tests in 0.5 M $H_2SO_4$ solution at +10 mA. The active faceted np-Ru exhibited a stable overpotential over 6 hours, supporting the reaction stability of the developed Ru{10$\bar{1}$0} facets. TEM characterizations have also confirmed that the np-Ru catalyst after chronoamperometric test retained not only the nanoporous structure but also the catalytically active {10$\bar{1}$0} facets (Figure 5.29 and 5.30).

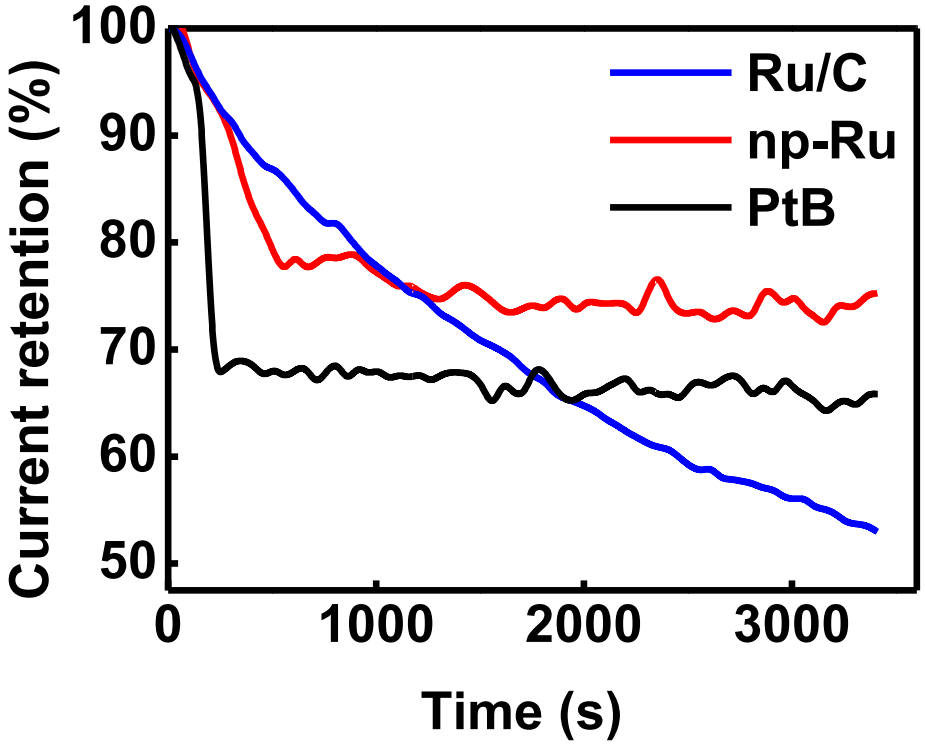


Figure 5.28: Chronoamperometric responses collected at applied potential (-0.4 V) for 1 hour in 0.5 m $H_2SO_4$ solution (graphite as counter electrode) for np-Ru (red), Ru/C (blue) and Pt black (black). The current retention for PtB and np-Ru steeply dropped on the early stage because some of the catalysts came off from the electrode surface, eventually reaching plateaus.

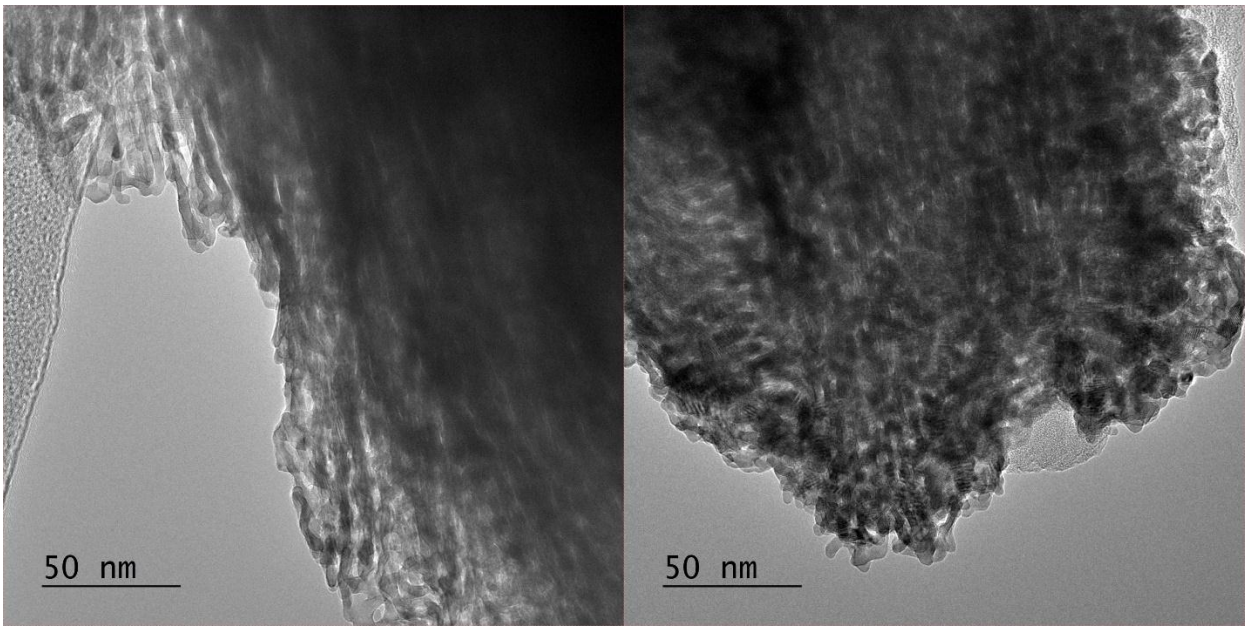


Figure 5.29: TEM images of as-prepared np-Ru.

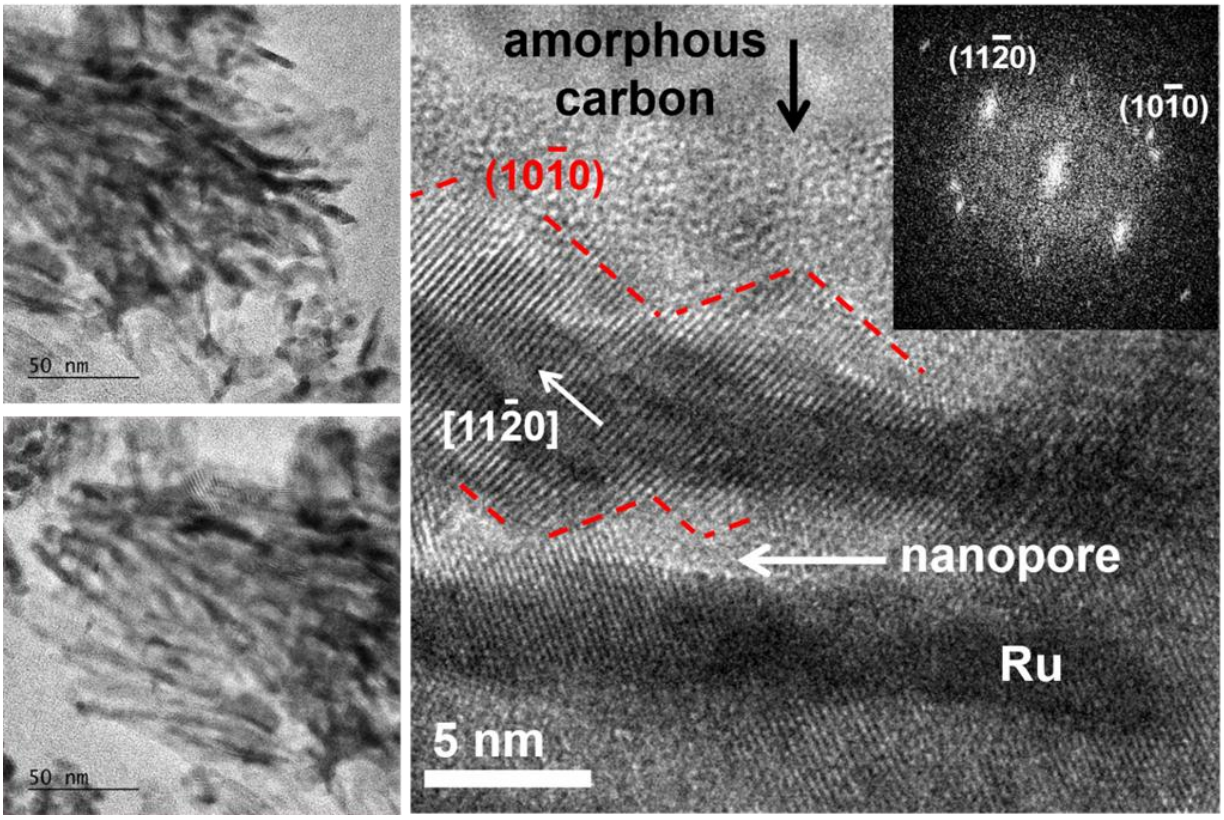


Figure 5.30: TEM images of np-Ru that experienced chronoamperometric tests (see Figure 5.28). An FFT pattern of the right-hand side high-resolution image is presented as the inset.

TOF of np-Ru was also measured by conducting copper under deposition ($Cu_{upd}$). Holding potential was increased little by little to get the charge only from Cu monolayer. TOF at 100 mV calculated was higher compared with literature of np-Ru which has no control over facet.[59] It showed that nanophase separation method had successfully induced the active facet and improved the catalytic activity.

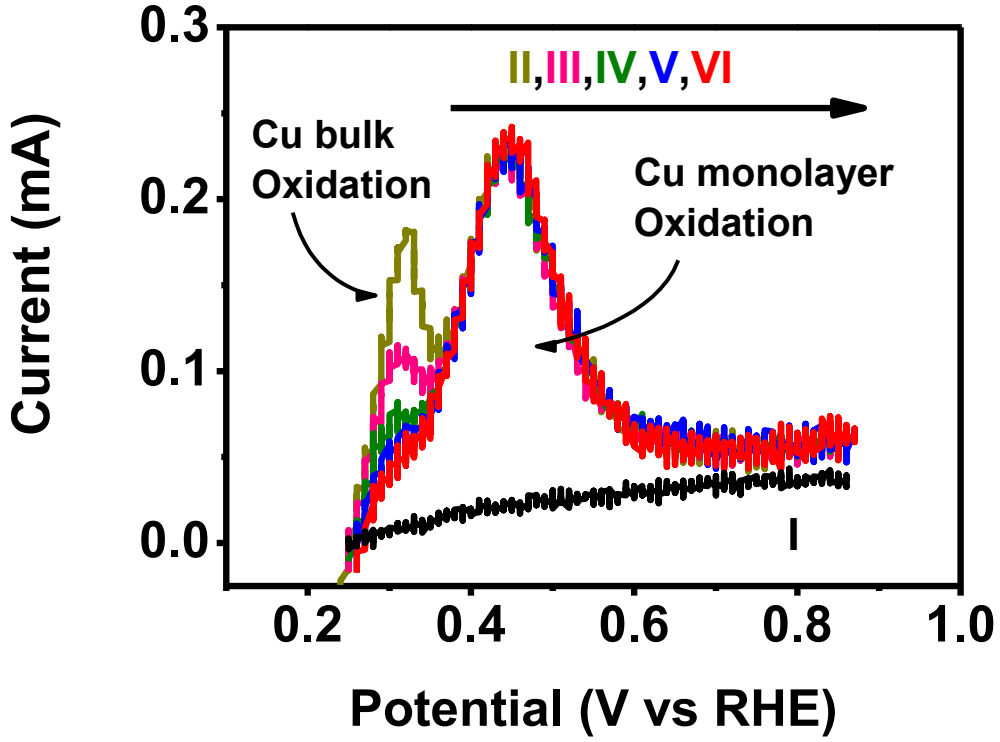


Figure 5.31: Copper under deposition of np-Ru. I corresponds to LSV in $H_2SO_4$, while II,III,IV,V,VI correspond to LSV in H2SO4 + 5mM $CuSO_4$ with underdeposition for 90s at potential of 0.245 V, 0.250 V, 0.255 V, 0.260 V, 0.265 V respectively.

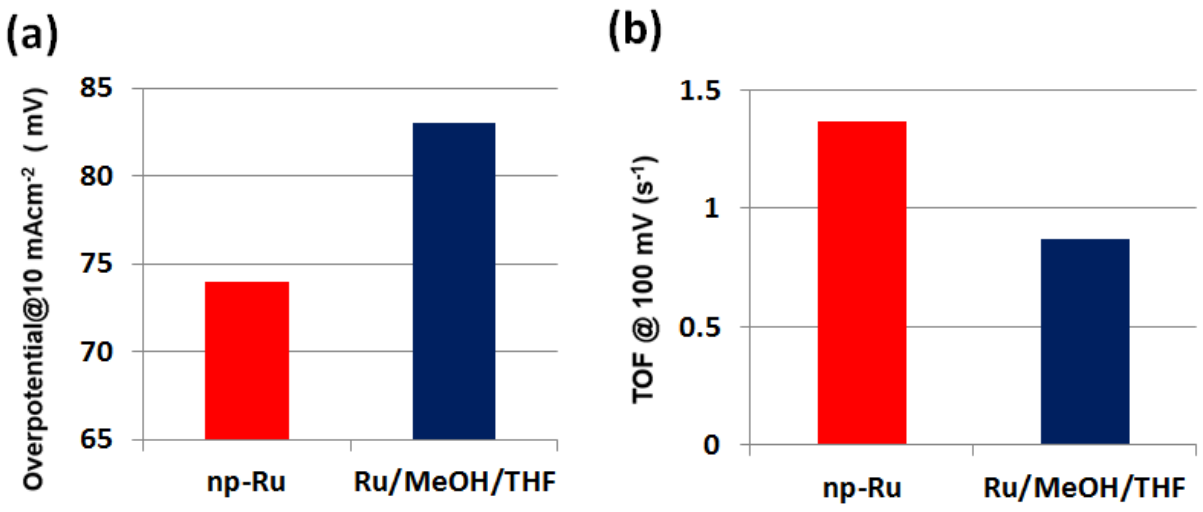


Figure 5.32: HER comparison between nanoporous metallic Ru of this work np-Ru (red) and previously reported Ru/MeOH/THF.[59] (a) Overpotential at 10 $mAcm^{-2}$ (b) TOF at 100 mV

# CHAPTER 6

# CONCLUSION AND FUTURE WORK

This research has provided comprehensive information on the nanophase separation and its utilization as a tailoring technique for nanomaterials. Practical application of the tailored nanomaterials as nanocatalysts was also covered. In conclusion, nanophase separation is a controllable synthesis pathway in which the pattern is dependent on diffusion coefficient of constituting elements. Oxidation of intermetallic compound yielded finely ordered metal-oxide nanocomposite, whereas subsequent removal of oxide phase through selective leaching resulted in nanoporous metal. In addition, the crystal reorientation during phase separation favoring the most stable metal-oxide interface caused certain facet exposure which enable facet tailoring when the element combination carefully chosen.

Nonetheless, the introduced nanophase separation route is still new and there is still a lot of room for improvement on this tailoring technique in order to reach industrialization. Deeper understanding of the phenomenon such as the atomic diffusion and establishment of a more direct model are necessary to further manipulate the tailoring technique. With the help of simulation and the developing materials informatics, deeper understanding of structure manipulation is possible in future including using cheaper naturally abundant elements. Application in electronics, structural, and others is also promising from this nanophase separation technique. The followings are challenges that could be thought of to expand the concept.

| Fundamentals/ Scientific Research | Application/ Engineering Research |
|---|---|
| • Single crystal precursor<br>• More direct model (instead of GS model)<br>• Use of 2D materials | • Use of naturally abundant elements (instead of precious metals)<br>• Functionalize as other device (ex: sensor, membrane, etc.) |

## REFERENCE


1 B. Jiang, C. Li, Ö. Dag, H. Abe, T. Takei, T. Imai, M. S. A. Hossain, M. T. Islam, K. Wood, J. Henzie and Y. Yamauchi, *Nat. Commun.*, 2017, **8**, 1–8.

2 B. R. Wiesenauer and D. L. Gin, *Polym. J.*, 2012, 44, 461–468.

3 X. Zhang, W. Lu, J. Dai, L. Bourgeois, J. Yao, H. Wang, J. R. Friend, D. Zhao and D. R. MacFarlane, *Sci. Rep.*, 2014, **4**, 1–5.

4 † Hongmei Luo, ‡ Li Sun, § and Yunfeng Lu and † Yushan Yan*, , DOI:10.1021/LA036367+.

5 J. H. Nam, Y. Y. Jang, Y. U. Kwon and J. Do Nam, *Electrochem. commun.*, 2004, **6**, 737–741.

6 V. Malgras, Q. Ji, Y. Kamachi, T. Mori, F.-K. Shieh, K. C.-W. Wu, K. Ariga and Y. Yamauchi, *Bull. Chem. Soc. Jpn.*, 2015, **88**, 1171–1200.

7 L. Zhang, H. Chang, A. Hirata, H. Wu, Q. K. Xue and M. Chen, *ACS Nano*, 2013, **7**, 4595–4600.

8 B. Lindström and L. J. Pettersson, *CATTECH*, 2003, **7**, 130–138.

9 J. W. Erisman, M. A. Sutton, J. Galloway, Z. Klimont and W. Winiwarter, *Nat. Geosci.*, 2008, **1**, 636–639.

10 S. Kameshima, K. Tamura, Y. Ishibashi and T. Nozaki, *Catal. Today*, 2015, **256**, 67–75.

11 Y. Lim, C. J. Lee, Y. S. Jeong, I. H. Song, C. J. Lee and C. Han, *Ind. Eng. Chem. Res.*, 2012, **51**, 4982–4989.

12 T. Margossian, K. Larmier, S. M. Kim, F. Krumeich, A. Fedorov, P. Chen, C. R. Müller and C. Copéret, *J. Am. Chem. Soc.*, 2017, **139**, 6919–6927.

13 K. Świrk, M. E. Gálvez, M. Motak, T. Grzybek, M. Rønning and P. Da Costa, *J. CO2 Util.*, 2018, **27**, 247–258.

14 M. M. Barroso-Quiroga and A. E. Castro-Luna, *Int. J. Hydrogen Energy*, 2010, **35**, 6052–6056.

15 D. C. LaMont and W. J. Thomson, *Appl. Catal. A Gen.*, 2004, **274**, 173–178.

16 ISO/TS 80004-1:2015(en), Nanotechnologies — Vocabulary — Part 1: Core terms, https://www.iso.org/obp/ui/#iso:std:iso:ts:80004:-1:ed-2:v1:en, (accessed 22 May 2020).

17 D. Akinwande, N. Petrone and J. Hone, *Nat. Commun.*, 2014, 5, 1–12.

18 H. Liu and T. J. Webster, *Biomaterials*, 2007, 28, 354–369.

19 C. Santhosh, V. Velmurugan, G. Jacob, S. K. Jeong, A. N. Grace and A. Bhatnagar, *Chem.*

*Eng. J.*, 2016, 306, 1116–1137.

20 J. S. Hyun, R. Ryoo, L. Zheng and O. Terasaki, *J. Am. Chem. Soc.*, 2001, **123**, 1246–1247.

21 D. Wang, W. Zhou, B. F. McCaughy, J. E. Hampsey, X. Ji, Y.-B. Jiang, H. Xu, J. Tang, R. H. Schmehl, C. O'Connor, C. J. Brinker and Y. Lu, *Adv. Mater.*, 2003, **15**, 130–133.

22 L. Wang and Y. Yamauchi, *J. Am. Chem. Soc.*, 2009, **131**, 9152–9153.

23 *IUPAC Compendium of Chemical Terminology*, IUPAC, 2009.

24 J. V. Edwards and S. C. Goheen, in *Functional Textiles for Improved Performance, Protection and Health*, Elsevier Ltd., 2011, pp. 293–319.

25 J. Gibbs, .

26 B. Ditchek and L. H. Schwartz, *Annu. Rev. Mater. Sci.*, 1979, **9**, 219–253.

27 E. P. Favvas and A. Ch Mitropoulos, *What is spinodal decomposition?*, 2008, vol. 1.

28 S. K. Nune, K. S. Rama, V. R. Dirisala and M. Y. Chavali, in *Nanostructures for Novel Therapy: Synthesis, Characterization and Applications*, Elsevier Inc., 2017, pp. 281–311.

29 F. Findik, *Mater. Des.*, 2012, 42, 131–146.

30 M. U. Kim, J. P. Ahn, H. K. Seok, E. Fleury, H. J. Chang, D. H. Kim, P. R. Cha and Y. C. Kim, *Met. Mater. Int.*, 2009, **15**, 193–196.

31 T. Höche, M. Mäder, S. Bhattacharyya, G. S. Henderson, T. Gemming, R. Wurth, C. Rüssel and I. Avramov, *CrystEngComm*, 2011, **13**, 2550–2556.

32 S. Veesler, L. Lafferrère, E. Garcia and C. Hoff, *Org. Process Res. Dev.*, 2003, **7**, 983–989.

33 C. Wagner, *J. Phys. Chem.*

34 G. Zhou, L. Luo, L. Li, J. Ciston, E. A. Stach, W. A. Saidi and J. C. Yang, *Chem. Commun.*, 2013, **49**, 10862–10864.

35 L. Luo, Y. Kang, J. C. Yang and G. Zhou, *J. Appl. Phys.*, 2015, **117**, 065305.

36 G. Zhou, *Appl. Phys. Lett.*, 2009, **94**, 201905.

37 S. Shoji, X. Peng, T. Imai, P. S. Murphin Kumar, K. Higuchi, Y. Yamamoto, T. Tokunaga, S. Arai, S. Ueda, A. Hashimoto, N. Tsubaki, M. Miyauchi, T. Fujita and H. Abe, *Chem. Sci.*, 2019, **10**, 3701–3705.

38 A. Gierer and H. Meinhardt, *Kybernetik*, 1972, **12**, 30–39.

39 D. Iron, J. Wei and M. Winter, *J. Math. Biol.*, 2004, **49**, 358–390.

40 J. Schnakenberg, *J. Theor. Biol.*, 1979, **81**, 389–400.

41 P. Gray and S. K. Scott, *Chem. Eng. Sci.*, 1983, **38**, 29–43.

42 M. Mimura and M. Nagayama, *Chaos An Interdiscip. J. Nonlinear Sci.*, 1997, **7**, 817–826.

43 F. Ernst, *Mater. Sci. Eng. R*, 1995, 14, 97–156.

44 O. Y. Gorbenko, S. V. Samoilenkov, I. E. Graboy and A. R. Kaul, *Chem. Mater.*, 2002, 14, 4026–4043.

45 H. Kim, C. O. Chui, K. C. Saraswat and P. C. McIntyre, *Appl. Phys. Lett.*, 2003, **83**, 2647–2649.

46 A. Stierle, P. Bödeker and H. Zabel, *Surf. Sci.*, 1995, **327**, 9–16.

47 K. A. Bogle, V. Anbusathaiah, M. Arredondo, J. Y. Lin, Y. H. Chu, C. Oneill, J. M. Gregg, M. R. Castell and V. Nagarajan, *ACS Nano*, 2010, **4**, 5139–5146.

48 A. Haryanto, S. Fernando, N. Murali and S. Adhikari, , DOI:10.1021/ef0500538.

49 IRENA, *Hydrogen: a renewable energy perspective*, Abu Dhabi, 2019.

50 D. Pakhare and J. Spivey, *Chem. Soc. Rev.*, 2014, **43**, 7813–1837.

51 W. Liu, E. Hu, H. Jiang, Y. Xiang, Z. Weng, M. Li, Q. Fan, X. Yu, E. I. Altman and H. Wang, *Nat. Commun.*, , DOI:10.1038/ncomms10771.

52 S. J. Gutić, A. S. Dobrota, M. Leetmaa, N. V. Skorodumova, S. V. Mentus and I. A. Pašti, *Phys. Chem. Chem. Phys.*, 2017, **19**, 13281–13293.

53 J. Bai, Q. Sun, M. Zhou, L. Wang, Y. Shen, Y. Ma, Z. Wang and C. Zhao, *J. Electrochem. Soc.*, 2018, **165**, H866–H871.

54 C. C. L. McCrory, S. Jung, I. M. Ferrer, S. M. Chatman, J. C. Peters and T. F. Jaramillo, *J. Am. Chem. Soc.*, 2015, **137**, 4347–4357.

55 Z. Zhou, L. Wei, Y. Wang, H. E. Karahan, Z. Chen, Y. Lei, X. Chen, S. Zhai, X. Liao and Y. Chen, *J. Mater. Chem. A*, 2017, **5**, 20390–20397.

56 B. Seo, D. S. Baek, Y. J. Sa and S. H. Joo, *CrystEngComm*, 2016, **18**, 6083–6089.

57 A. A. Alireza, N. Hamnabard, S. M. H. Meshkati, M. Pakan and Y. H. Ahn, *Dalt. Trans.*, 2019, **48**, 5429–5443.

58 J. Mahmood, F. Li, S. M. Jung, M. S. Okyay, I. Ahmad, S. J. Kim, N. Park, H. Y. Jeong and J. B. Baek, *Nat. Nanotechnol.*, 2017, **12**, 441–446.

59 S. Drouet, J. Creus, V. Collière, C. Amiens, J. García-Antón, X. Sala and K. Philippot, *Chem. Commun.*, 2017, **53**, 11713–11716.

60 S. Gates-Rector and T. Blanton, *Powder Diffr.*, 2019, **34**, 352–360.

61 Y. Wang, X. Hong, B. Li, W. Wang and D. Wang, *J. Nat. Gas Chem.*, 2008, **17**, 344–350.

62 H.-M. Yang and M.-K. Chan, *Catal. Commun.*, 2011, **12**, 1389–1395.

63 W.-H. Cheng, I. Chen, J. Liou and S.-S. Lin, *Top. Catal.*, 2003, **22**, 225–233.

64 N. S. Marinkovic, M. B. Vukmirovic and R. R. Adzic, in *Modern Aspects of Electrochemistry*, Springer New York, 2008, pp. 1–52.

65 M. G. Walter, E. L. Warren, J. R. McKone, S. W. Boettcher, Q. Mi, E. A. Santori and N. S. Lewis, *Chem. Rev.*, 2010, **110**, 6446–6473.

66 Y. Gorlin and T. F. Jaramillo, *J. Am. Chem. Soc.*, 2010, **132**, 13612–13614.

67 M. B. Zakaria, *RSC Adv.*, 2016, **6**, 10341–10351.

68 M. B. Zakaria, M. Hu, M. Pramanik, C. Li, J. Tang, A. Aldalbahi, S. M. Alshehri, V. Malgras and Y. Yamauchi, *Chem. - An Asian J.*, 2015, **10**, 1541–1545.

69 L. X. Chen, Z. W. Chen, Y. Wang, C. C. Yang and Q. Jiang, *ACS Catal.*, 2018, **8**, 8107–8114.

70 A. Kahyarian, B. Brown and S. Nesic, in *Journal of the Electrochemical Society*, Electrochemical Society Inc., 2017, vol. 164, pp. H365–H374.

71 Y. Li, L. A. Zhang, Y. Qin, F. Chu, Y. Kong, Y. Tao, Y. Li, Y. Bu, D. Ding and M. Liu, *ACS Catal.*, 2018, **8**, 5714–5720.

72 T. Shinagawa, A. T. Garcia-Esparza and K. Takanabe, *Sci. Rep.*, 2015, **5**, 1–21.

# APPENDIX

<Simulation Code>

```
n = 64;

a = 0.017;

b = 0.057;

du = 0.1;

dv = (1/5)*du;

dt = 0.01;

totaliter = 5000;

u = a + 0.3 RandomReal[{-0.5, 0.5}, {n, n}];

v = b/a + 0.3 RandomReal[{-0.5, 0.5}, {n, n}];


cf = Compile[{{uIn, _Real, 2}, {vIn, _Real,

     2}, {aIn, _Real}, {bIn, _Real}, {duIn, _Real}, {dvIn, _Real}, {dtIn, \

_Real}, {iterationsIn, _Integer}},


   Block[{u = uIn, v = vIn, lap, dt = dtIn,

     kern = N[{{0, 1, 0}, {1, -4, 1}, {0, 1, 0}}], du = duIn, dv = dvIn},


    Do[

lap =   RotateLeft[u, {1, 0}] + RotateLeft[u, {0, 1}] + RotateRight[u, {1, 0}] +

        RotateRight[u, {0, 1}] - 4*u;


     u = u + dt (du lap + a (1 - u) - v (u v));
```

```
    lap =

        RotateLeft[v, {1, 0}] + RotateLeft[v, {0, 1}] + RotateRight[v, {1, 0}] +
      RotateRight[v, {0, 1}] - 4*v;

    v = v + dt (dv lap - v (b - u v));

    , {iterationsIn}]; {u, v}]];

Timing[c1 = cf[u, v, a, b, du, dv, dt, totaliter];]
ListDensityPlot[c1[[2]], ColorFunction -> Hue , ColorFunctionScaling -> True]
```

<Thermodynamic Limit of Dry Reforming of Methane>

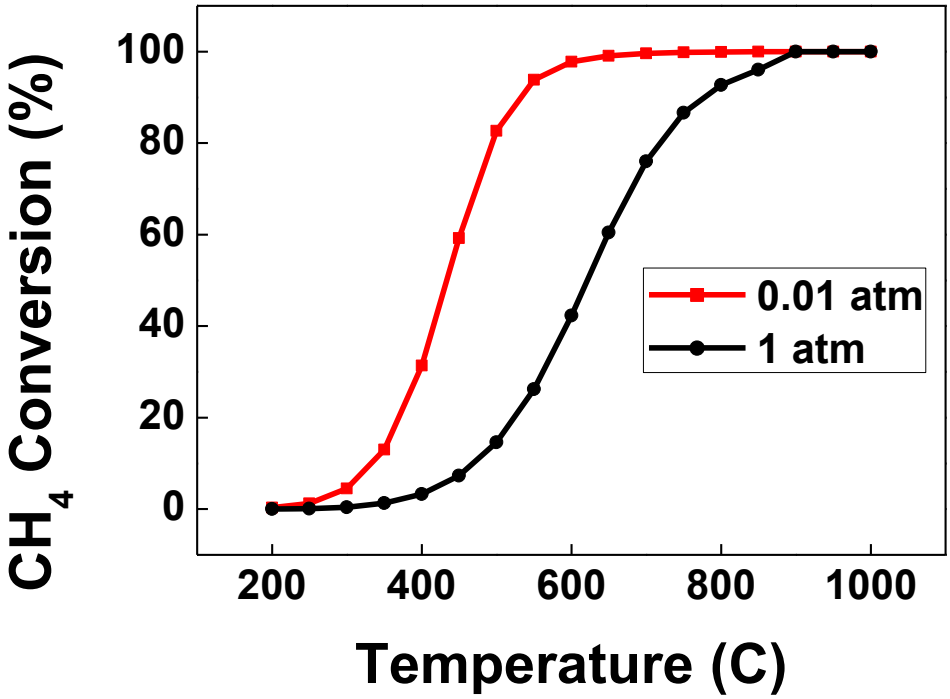

<Phase Diagram>

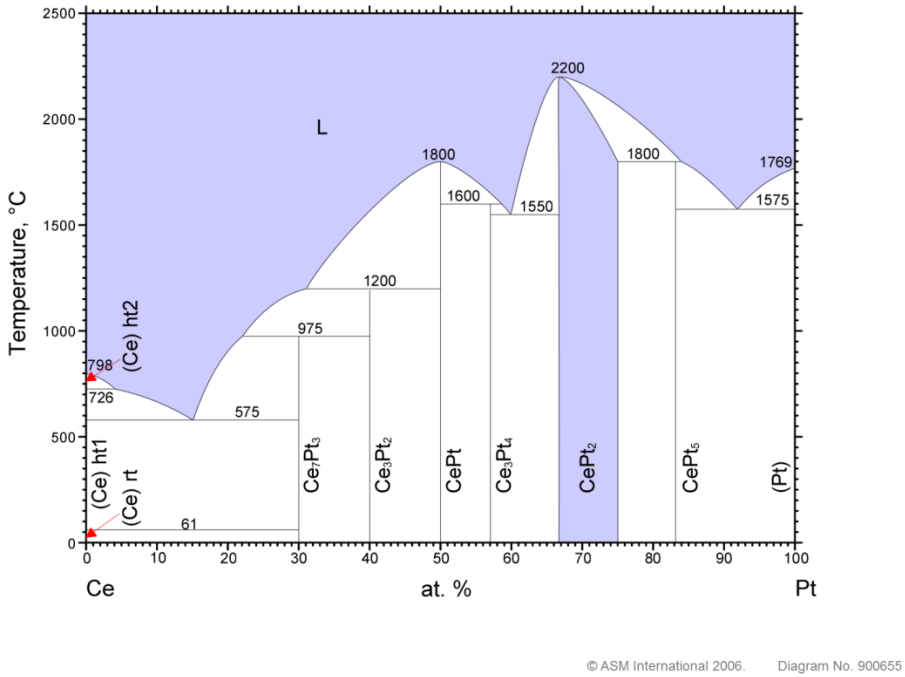


Okamoto H., Ce-Pt (Cerium-Platinum), Binary Alloy Phase Diagrams, II Ed., Ed. T.B. Massalski, Vol. 2, 1990, p 1098-1099

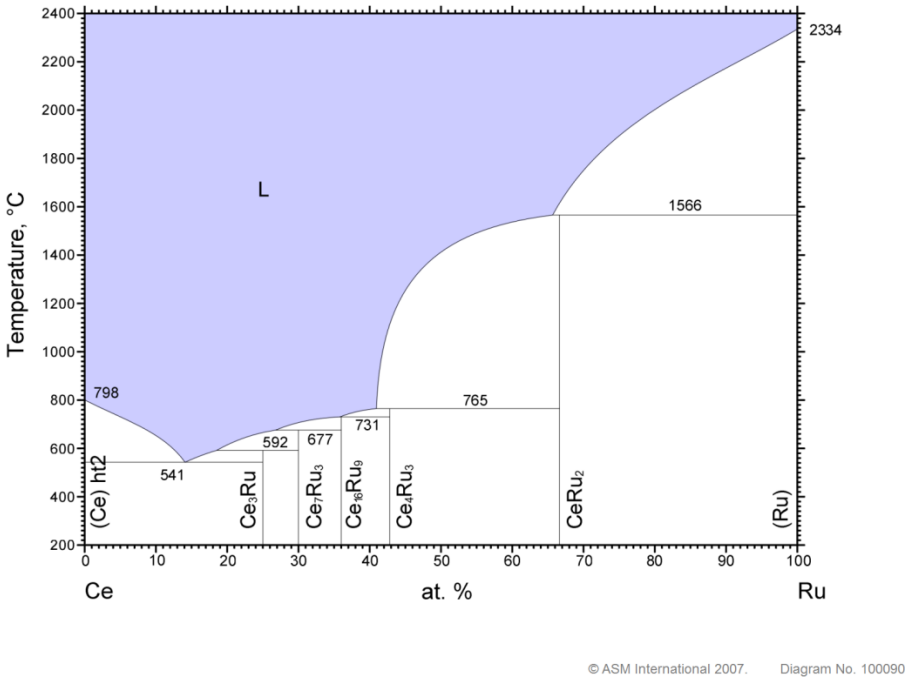


Selhaoui N., Charles J., Bouirden L., and Gachon J.C., Optimization of the binary Ce-Ru system, J. Alloys Compd., Vol. 269, 1998, p 166-172

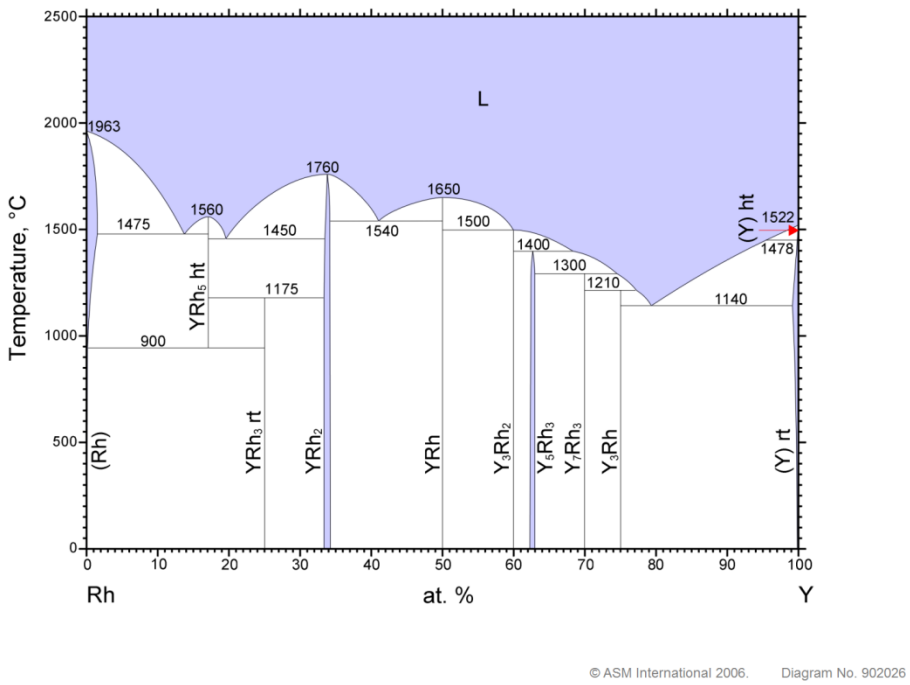


Okamoto H., Rh-Y (Rhodium-Yttrium), Binary Alloy Phase Diagrams, II Ed., Ed. T.B. Massalski, Vol. 3, 1990, p 3242-3246

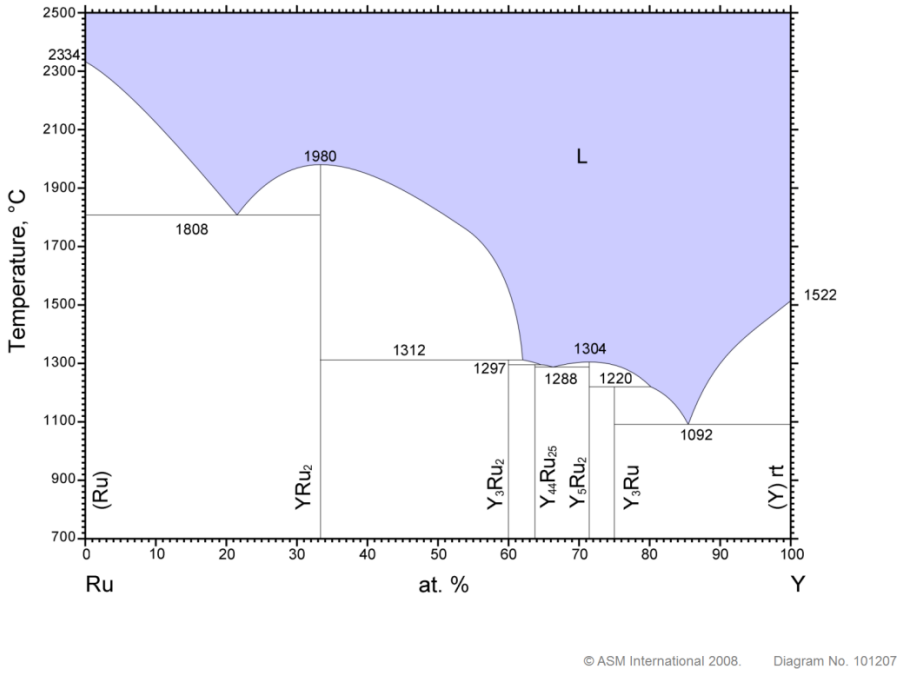


Selhaoui N., Charles J., Kleppa O.J., Bouirden L., and Gachon J.C., The ruthenium-yttrium system: An experimental calorimetric study with a phase diagram optimization, J. Solid State Chem., Vol. 138, 1998, p 302-306

## LIST OF PUBLICATIONS

Najib, A. S. B. M., Peng, X., Hashimoto, A., Shoji, S., Iida, T., Bai, Y., & Abe, H. (2019). Mesoporous Rh Emerging from Nanophase-separated Rh-Y Alloy. *Chemistry–An Asian Journal*, *14*(16), 2802-2805.

Nishiguchi, H., Najib, A. S. B. M., Peng, X., Cho, Y., Hashimoto, A., Ueda, S., ... & Abe, H. Intertwined Nickel and Magnesium Oxide Rival Precious Metals for Catalytic Reforming of Greenhouse Gases. *Advanced Sustainable Systems*, 2000041.

Imada, S., Peng, X., Cai, Z., Najib, A. S. B. M., Miyauchi, M., Abe, H., & Fujita, T. (2020). NiYAl-Derived Nanoporous Catalysts for Dry Reforming of Methane. *Materials*, *13*(9), 2044.

Najib, A. S. B. M., Iqbal, M., Zakaria, M.B., Shoji, S., Cho, Y., Peng, X., Ueda, S., Hashimoto, A.,Fujita, T., Miyauchi, M., Yamauchi, Y., Abe, H., (2020), Active Faceted Nanoporous Ruthenium for Electrocatalytic Hydrogen Evolution, *Journal of Materials Chemistry A* - **Accepted**

## ACKNOWLEDGEMENT

Firstly, I would like to express my gratitude to my principal supervisor, Professor Abe Hideki for the opportunity of this doctoral course and continuous support technically, financially, and mentally throughout the research activities. He indeed had created conducive working environment that allows freedom of ideas to be expressed, flexible research activities, and broad research networking. His expertise in materials science has guided me a lot in understanding and expanding the research ideas, as well as getting used to the scientific publication system. I would also like to thank Dr Nor Akmal Fadil from Universiti Teknologi Malaysia (UTM) for bridging me with him.

Special thanks to my colleagues in Abe laboratories, Dr Peng Xiao Bo, Ms Okura Naoko, Ms Motohashi Sanae, Ms Nishiguchi and our organization backbones Ms Nohara Yukiko, Ms Umehara Sachie, and Ms Umeda Junko. It has been a priceless treasure of my research career working with this team. Not forgetting, Crest project collaborator Prof Miyauchi Masahiro, Prof Fujita Tekeshi, and Dr Shuusaku Shoji. I would also like to extent my gratitude to collaborator from NIMS researchers, Dr Hashimoto Ayako for her support in TEM observations and consultations, Prof Xu Ya for physisorption test, and Dr Ueda Shigenori for HAXPES analysis. I would also like to extend my gratitude to Saitama University staffs for continuously supporting my research especially to Prof. Norihiko Kamata and Assoc.Prof. Kenji Kamishima.

My utmost gratitude to my supportive family members, my beloved parents, Hj. Mohd Najib Zakaria and Hjh. Safiah Abdullah, and siblings, Ahmad Najmin Mohd Najib, Aainaa Salwa Mohd Najib, Mohd Nadzri Mohd Najib, Nuur Shuhada Mohd Najib, and Asyraf Syahir Mohd Najib.

I gratefully acknowledge the financial supports from JST Crest project, Mitsubishi Corporation Scholarship, Saitama University Research Assistance scheme, and Universiti Teknologi Malaysia SLAM scholarship.

Abdillah Sani Bin Mohd Najib

June 2020